DISSERTATION

THE ROLE OF EARTH SYSTEM INTERACTIONS IN LARGE-SCALE ATMOSPHERIC CIRCULATION AND CLIMATE

Submitted by

Simchan Yook

Department of Atmospheric Science

In partial fulfillment of the requirements

For the Degree of Doctor of Philosophy

Colorado State University

Fort Collins, Colorado

Summer 2023

Doctoral Committee:

Advisor: David W.J. Thompson

A. R. Ravishankara
James Hurrell
Imme Ebert-Uphoff

ABSTRACT

THE ROLE OF EARTH SYSTEM INTERACTIONS
IN LARGE-SCALE ATMOSPHERIC CIRCULATION AND CLIMATE

The complex interactions among different components of the Earth system play a key role in governing the climate variability through various physical processes. For example, an interaction between the fluctuations in one component of the Earth system and associated variations in another component of the Earth system can either amplify or dampen the climate variability depending on the nature of their two-way feedback mechanisms. Thus, understanding the role of various physical interactions among components of the Earth system is critical to understand the changes in climate as well as to reduce the uncertainty in future climate projections. This dissertation focuses on discovering the key processes and interactions among different components of the Earth system on the climate variability using observations and model hierarchies.

In Part 1, the interactions between the atmospheric circulation and western North Pacific SST anomalies are explored in two sets of simulations: 1) a simulation run on a coupled atmosphere-ocean general circulation model (GCM), and 2) a simulation forced with prescribed, time-evolving SST anomalies over the western North Pacific. The results support the interpretation of the observed lead/lag relationships between western North Pacific Sea Surface Temperature (SST) anomalies and the atmospheric circulation, and provide numerical evidence that SST variability over the western North Pacific has a demonstrable effect on the large-scale atmospheric circulation throughout the North Pacific sector.

In Part 2, the role of moist lapse rate in altering the temperature variability under climate change is explored. To reduce the complexity of the problem, the changes in the temperature variance under global warming are first analyzed in the simplest version of model hierarchy: a single column Rapid Radiative Transfer Model with a simplified convective adjustment. Similar analyses were

repeated with varying model hierarchies with additional complexities: a global general circulation model in global Radiative Convective Equilibrium (RCE) setting with fixed SST, and fully coupled Earth system models. The results highlight the role of moist lapse rate as a potential constraint for climate variability in the tropical atmosphere simulated by different model hierarchies.

In Part 3, the effects of coupled chemistry-climate interactions on the amplitude and structure of stratospheric temperature variability are quantified in two numerical simulations: A "free running" simulation that includes fully coupled chemistry-climate interactions; and a "specified chemistry" version of the model forced with prescribed chemical composition. The results indicate that the inclusion of coupled chemistry-climate interactions increases the internal variability of temperature by a factor of $\sim$two in the lower tropical stratosphere through dynamically driven ozone-temperature feedbacks. The results highlight the fundamental role of two-way feedbacks between the atmospheric circulation and chemistry in driving climate variability in the lower stratosphere.

In Part 4, the effects of coupled chemistry-climate interactions on the large-scale atmospheric circulation are further explored based on two observational case studies of the Antarctic ozone holes of 2020 and 2021. The 2020 and 2021 were marked by two of the largest Antarctic ozone holes on record. It has been demonstrated that the ozone holes of 2020 and 2021 were associated with large changes in the atmospheric circulation consistent with the climate impacts of Antarctic ozone depletion. The ozone holes were also unusual for their associations with aerosol burdens due to two extraordinary events: the Australian wildfires of early 2020 and the eruption of La Soufriere in 2021. The results provide suggestive evidence that injections of both wildfire smoke and volcanic emissions into the stratosphere can lead to hemispheric-scale changes in surface climate.

This dissertation provides a detailed look at the complex aspects of the coupled interactions among different components of the Earth system and their roles on climate variability and large-scale dynamics. To clarify the role of the different physical processes contributing to the climate responses, this study performed a comprehensive analysis based on observations as well as a series of numerical experiments run on different configurations of climate model hierarchies. The find-

ings herein improve our understanding of different Earth system interactions and their influences on global climate and large-scale atmospheric dynamics.

ACKNOWLEDGEMENTS

I would like to express my deepest gratitude to all of the wonderful people around me who have always supported me in different ways throughout the five years of my PhD adventure.

I would like to thank my advisor, Dr. David Thompson, for helping me grow both personally and professionally through his endless support, insights, guidance, and encouragement. Without his mentorship, I would not have been able to learn and enjoy the fun of science as well as the beauty of the mountains.

I would also like to acknowledge my Ph.D. committee members: Dr. James Hurrell, Dr. Ravishankara, and Dr. Imme Ebert-Uphoff. I thank them not only for their careful review and many helpful suggestions on my research, but also for their mentorship and encouragement. I could not imagine a more friendly and supportive team of committee members.

Many thanks to my two other exemplary mentors, Dr. Susan Solomon and Dr. Lantao Sun, for their generous gifts of time, wisdom, and mentorship. I could not have reached this point without their help.

Thanks to the members of the Thompson research group, past and present: Casey, Chloe, Dhyey, James, Jingyuan, Leif, Lina, Luke, Sam, Ying, and Ying-Ju, for being such great colleagues. I feel lucky to have known them. Special thank you to Casey and Ying-Ju for enduring my distracting work-ethic in the office, such as my furious and noisy typing habit, and asking random questions when you are busy. Thank you for still being my friends, despite all that.

Finally, I am grateful to my parents in South Korea for their love and support which have always been my source of resilience. I also want to thank my Korean friends, Chelsea, Jangho, Jinkyul, Juni, Joonsuk, Seonsik, Yoo-Jeong, Yoonjin, Devira and Jennifer, for our long-lasting friendship spanning more than a decade. I have tremendously benefited from our friendship.

TABLE OF CONTENTS

LIST OF TABLES

LIST OF FIGURES

Chapter 1

Introduction

1.1 Overview

"Climate science investigates the structure and dynamics of earth's climate system. It seeks to understand how global, regional and local climates are maintained as well as the processes by which they change over time. In doing so, it employs observations and theory from a variety of domains, including meteorology, oceanography, physics, chemistry and more." cited from Stanford Encyclopedia of Philosophy [Kooy (2015)].

This dissertation addresses four different research questions in climate science, focuses on discovering the key processes and interactions among different components of the Earth's system on climate variability using observational, modeling and theoretical studies.

1.2 Climate Variability

Substantial progress has been made over the last few decades in our understanding of the future of climate change. Global warming of the climate system is "unequivocal" and is linked directly to increasing anthropogenic greenhouse gas (GHG) emissions (IPCC, 2012, 2021). Yet, there still exist uncertainties in our estimation of the projected climate change. This is primarily due to the dynamic nature of Earth's climate system, which is characterized by its variability across many different temporal and spatial scales. The variability of Earth's climate is a response to the different types of climate forcing and arises from interplays between different physical processes and system components. To reduce uncertainty in future climate projections, it is essential to understand the factors that cause changes in Earth's climate.

Changes in Earth's climate, or climate variability, are primarily categorized into two types depending on the source of the variability: 1) forced responses to external forcing, or when the climate system is perturbed from the outside [e.g., occurrence of Antarctic ozone hole due to

emission of man-made ozone depleting substances (ODSs)] and 2) internal climate variability [or also referred as "climate noise"; Madden (1976); Schneider and Kinter (1994); Deser et al. (2012)] that arises from physical processes intrinsic to the climate system in the absence of external forcing (e.g., changes in tropical ozone concentration associated with changes in tropical upwelling in the atmosphere).

The latter, internal variability, is known as one of the main sources of uncertainty in our future climate projections. The complex interactions among different components of Earth's system play a key role governing climate variability through various physical processes. For example, an interaction between the fluctuations in one component of Earth's system (e.g., large-scale atmospheric circulation in the stratosphere) and associated variations in another component of Earth's system (e.g., stratospheric ozone) can either amplify or dampen the climate variability (e.g., stratospheric air temperature variability) depending on the nature of their two-way feedback mechanisms. Thus, understanding the role of various physical interactions among components of Earth's system on internal climate variability is crucial to understanding the changes in climate as well as reducing uncertainty in future climate projections. This dissertation tries to address four different types of climate interactions contributing to internal climate variability.

1.3 Research Approach

In general, the research process in this dissertation is structured in three steps: 1) identifying novel aspects of climate interactions in observation, 2) interpreting the observed phenomena and developing hypotheses based on theoretical understanding, and 3) testing the hypotheses in a series of numerical modeling experiments with different model hierarchies.

The research questions in this dissertation are inspired from findings in observational studies based on analyses of reanalysis data or satellite observation, such as the European Centre for Medium-Range Weather Forecasts reanalysis version 5 over the period 1979-2020 [ERA5; Hersbach et al. (2020)], the Ozone Mapping and Profiler Suite Limb Profiler (OMPS-LP) instrument [Taha et al. (2021).

Then, follow up modeling studies are performed to improve our understanding of physical processes involved. By comparing the outputs from the two simulations in different model hierarchies or configurations, one including the specific process of interest and the other without the representation of the process, we can gain insight into the role of specific process on the climate variability. To assess the role of interactive stratospheric chemistry on climate variability, WACCM with fully coupled chemistry, as well as specified chemistry version are used. To investigate the role of air-sea interaction, CESM with a fully coupled ocean model and the Atmospheric Model Intercomparison Project (AMIP)-style simulation with prescribed data ocean are used.

Climate models with simpler hierarchies are also used in order to understand the climate interactions in a more controlled setting. For example, to understand the role of radiative transfer on temperature variability, a single-column radiative transfer model with a simple convective adjustment (Konrad) is used. Then the analyses were repeated using the simulations run on a general circulation model in the Radiative Convective Equilibrium (RCE) setting with fixed SSTs to test the hypothesis in a global context. Finally, the analyses were done using outputs from a fully coupled general circulation model to assess the hypothesis in the realistic climate.

For example, the chapter 3 is motivated from the findings of previous observational studies [Wills et al. (2016); Wills and Thompson (2018)], on the lead/lag relations between the atmospheric circulation and midlatitude Sea Surface Temperature (SST) field over the western North Pacific. Based on linear theory of atmospheric thermodynamics, Wills and Thompson (2018) interpreted that the lead/lag relations are the results of interactions between the SST anomalies and the extratropical atmospheric circulation. Thus, we designed numerical experiments to test the hypotheses by controlling the coupling between SST fields and atmospheric circulation. The results from numerical experiments prove the hypotheses also hold in the simulated climate and provide numerical evidence to bolster the interpretation from the observed studies.

1.4 Outline of dissertation

The goal of my dissertation is to clarify the role of interactions between different components of the Earth system (e.g., oceanic variability, atmospheric chemistry, and atmospheric radiation) and atmospheric circulation on climate variability. A series of numerical experiments run on different configurations and hierarchies of climate models is performed to disentangle the complex aspects of the coupled interactions in climate system.

The dissertation focuses on the role of Sea Surface Temperature (SST) variability over the Kuroshio-Oyashio Extension (KOE) region on the large-scale atmospheric circulation over the North Pacific (Part 1), on the changes in internal temperature variability in radiative-convective equilibrium (RCE) under climate change (Part 2), on the impact of stratospheric chemistry-climate interactions on the temperature variability in the lower tropical stratosphere (Part 3), and on the potential influence of wildfire smoke and volcanic ashes upon the recent ozone hole and large-scale atmospheric circulation in the Southern Hemisphere (Part 4).

Chapter 2

Air-Sea Interactions[1]

Observational studies argued that the lead/lag relations between the atmospheric circulation and midlatitude SST field uniquely identify two distinct patterns of atmospheric variability that force and respond to midlatitude SST anomalies. The observed lead/lag relationships between the atmospheric circulation anomalies and SST anomalies are assessed in two sets of simulations run on the NCAR Community Earth System Model Version 1 (CESM): a simulation run on a fully coupled version of CESM allowing the two-way coupling between the atmosphere and SST field, and 2) a simulation forced with prescribed, time-evolving SST anomalies over the western North Pacific which only allowing the ocean-to-atmosphere forcing. Together, the simulations support the interpretation of the observed lead/lag relationships between western North Pacific SST anomalies and the atmospheric circulation, and provide numerical evidence that SST variability over the western North Pacific has a demonstrable effect on the large-scale atmospheric circulation throughout the North Pacific sector.

2.1 Introduction

It is clear that the atmospheric circulation influences sea surface temperature (SST) variability in the midlatitudes. Sea surface temperature variability in the North Atlantic and North Pacific is strongly forced by the atmospheric circulation through the surface heat fluxes and Ekman transport [e.g., Davis (1976); Frankignoul and Hasselmann (1977); Frankignoul (1985); Deser and Timlin (1997); Alexander (2010) and references therein]. Circulation variability in the extratropical upper oceans is driven predominantly by variations in the surface wind stress (e.g., Vallis (2017)).

[1]The results outlined in Chapter 2 have been published in the *Journal of Climate*: Yook, S., D. W. J. Thompson, L. Sun, and C. R. Patrizio, 2022b: The atmospheric response to western north pacific sea-surface temperature anomalies. *Journal of Climate*, **35 (11)**, 3335–3352, doi: 10.1175/JCLI-D-21-0371.1.

It is less clear whether extratropical SST variability, in turn, influences the atmospheric circulation [e.g., Kushnir et al. (2002)]. Linear theory predicts that the surface fluxes associated with midlatitude SST anomalies are balanced primarily by horizontal temperature advection by the lower-tropospheric flow [Hoskins and Karoly (1981)]. However, the predicted changes in the atmospheric flow are modest relative to the large internal variability of the extratropical atmosphere, which can complicate the detection of the response [e.g., Kushnir et al. (2002)]. The atmospheric response is further complicated by its dependence on the mean jet position and feedbacks associated with extratropical wave–mean flow interactions (e.g., Peng et al. (1997); Hall et al. (2001); Peng and Robinson (2001); Kushnir et al. (2002); Woollings et al. (2010); Saulière et al. (2012)).

Nevertheless, a growing body of evidence suggest that extratropical SST anomalies can play an active role in climate variability. For examples: Czaja and Frankignoul (2002) provide evidence of linkages between North Atlantic SST anomalies and an atmospheric pattern resembling the North Atlantic Oscillation (NAO). Frankignoul and Sennéchael (2007) and Frankignoul et al. (2011) provide evidence of analogous linkages between North Pacific SST anomalies and large-scale atmospheric variability over the North Pacific sector. A series of studies demonstrate the importance of large SST gradients for the low-level atmospheric flow [e.g., Chelton et al. (2004); O'Neill et al. (2005); Chelton and Xie (2010); Wang et al. (2019)]. An increasing number of studies reveal seemingly robust linkages between SST anomalies over the Northern Hemisphere western boundary current regions and the free tropospheric flow [e.g., Minobe et al. (2008); Minobe et al. (2010); Nakamura et al. (2004); Nakamura et al. (2008); Xu et al. (2010); Kwon et al. (2010); Kwon et al. (2011); Taguchi et al. (2012); Kwon and Joyce (2013); Small et al. (2014); O'Reilly and Czaja (2015); O'Reilly et al. (2017); Smirnov et al. (2015); Révelard et al. (2016); Wills et al. (2016); Wills and Thompson (2018); Simpson et al. (2019); Athanasiadis et al. (2020); Kwon et al. (2020)].

In a pair of recent papers [Wills et al. (2016); Wills and Thompson (2018), hereafter WT18], we argued that the observed lead–lag relationships between the atmospheric circulation and midlatitude SST field uniquely identify the atmospheric circulation anomalies that act to drive and

respond to midlatitude SST anomalies. Over both the North Atlantic and North Pacific sectors, the atmospheric circulation anomalies that lead large SST anomalies by several weeks are consistent with horizontal temperature advection anomalies that force the SST field, whereas the atmospheric circulation anomalies that lag large SST anomalies are reminiscent of the linear atmospheric response to midlatitude SST anomalies [Hoskins and Karoly (1981)].

The purpose of this study is to 1) test the reproducibility of the observed lead/lag relationships between the midlatitude SST field and atmospheric circulation in output from a fully coupled Atmosphere-Ocean General Circulation Model (AOGCM) and 2) test the hypothesis that the lead/lag relationships uniquely reveal the extratropical atmospheric response to midlatitude SST anomalies in a prescribed SST, Atmospheric Model Intercomparison Project (AMIP)-style simulation. We focus here on atmosphere-ocean interactions over the North Pacific sector. The North Atlantic sector will be considered in a separate study.

2.2 Data and Analysis Details

2.2.1 Observations

We use two primary observational data sources. The Hurrell et al. (2008) SST data set is used to generate the boundary conditions used to force the "Kuroshio-Oyashio Global Atmosphere" (KOGA) experiments over the period 1901-2015 (as described below). All other observational data analyses are based on the European Centre for Medium-Range Weather Forecasts reanalysis version 5 over the period 1979-2020 [ERA5; Hersbach et al. (2020)]. Note that SSTs from ERA5 are prescribed from observations [see Hersbach et al. (2020) and references therein].

2.2.2 Models and experiments

The primary results are based on experiments run on two different configurations of the NCAR Community Earth System Model version 1 [CESM1; Hurrell et al. (2013)]: 1) A fully-coupled configuration in which SSTs are interactive (the coupled AOGCM experiment) and 2) A prescribed SST-configuration in which the model is driven by SST anomalies prescribed over the western

North Pacific. The atmospheric component of the model is the Community Atmospheric Model version 5 (CAM5) run with 30 vertical levels. CAM5 is run at horizontal resolution of 0.9°×1.25° in the fully-coupled configuration and 1.9°×2.5° in the prescribed SST configuration. The ocean component of the model is run on the CESM nominal 1-degree horizontal resolution grid.

The coupled simulations run on CESM1 include 40 members of a large-ensemble integrated with historical forcings over the period 1920–2005 and representative concentration pathway 8.5 (RCP8.5) forcing from 2006 to 2100 [Kay et al. (2015)]. We used output from the Coupled AOGCM experiments over the period 1980-2020. The large-ensemble output are available through the Large Ensemble Community Project and produced on resources provided by NSF/CISL/Yellowstone. The use of multiple ensemble members in the analyses helps isolate the signatures of atmosphere-ocean interactions from other forms of internal climate variability.

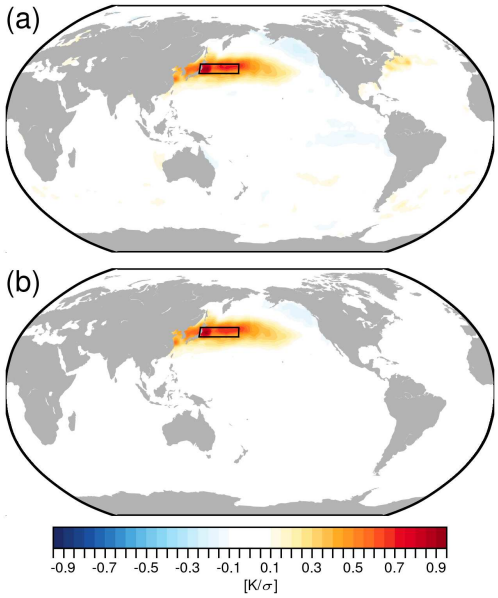

Figure 2.1: (top) SST anomalies regressed on standardized SST anomalies averaged over the western North Pacific region (as indicated by the black box). (bottom) The $K^*_{SST}(x,t)$ pattern used to force the KOGA simulation. The pattern is identical to that in the top panel, except that SST anomalies outside the North Pacific region are set to zero. See text for details.

The prescribed SST experiments are forced with 1) time-varying SST anomalies in the western North Pacific region over an area corresponding roughly to the Kuroshio-Oyashio extension (KOE)

region and 2) the annually-repeating seasonal-cycle of SSTs over all other regions of the world ocean. As such, the experiments isolate the influence of SST anomalies in a particular region - here the western North Pacific - from the influence of SST anomalies over other regions of the globe. The experiment design is analogous to the "middle latitude ocean-global atmosphere" (MOGA) experiments from Lau and Nath (1994). It is also similar to the pacemaker experiments in Kosaka and Xie (2013) but here SST anomalies outside the "pacemaking" region are prescribed to their seasonally-varying climatological values rather than coupled.

The pattern of SST anomalies used to force the KOGA runs is found as follows.

1. The linear trend and seasonal cycle is subtracted from SSTs at all grid boxes in the Hurrell et al. (2008) dataset over the period of 1901-2015.

2. Variations in SST anomalies over the western North Pacific are defined as the time series of detrended SST anomalies averaged over 36-42°N, 140-171°E (as indicated by the box in Figure 2.1a), which corresponds to the region of largest variance in the North Pacific SST field and roughly to the Kuroshio-Oyashio extension region. The time series is hereafter denoted as the K index time series, $K(t)$, where t denotes the month.

3. The pattern of wintertime SST anomalies associated with variations in $K(t)$ is found by regressing December-February (DJF) SST anomalies onto standardized values of $K(t)$. The resulting regression map is shown in the top panel of Figure 2.1 and is hereafter denoted $\beta_{KSST}(x)$, where x denotes the grid point. The pattern of SSTs regressed on the K index time series for the global domain is shown in Figure 2.2.

4. Sea-surface temperature anomalies at all months 1901-2015 are decomposed into two components: a) A component that is linearly congruent with the pattern of $\beta_{KSST}(x)$ (hereafter $\beta^*_{KSST}(x,t)$) and b) a component that is linearly independent of $\beta_{KSST}(x)$. Note that at that time step i, $\beta^*_{KSST}(x,t)$ has the same spatial structure as $\beta_{KSST}(x)$ but amplitude determined by the spatial projection of $\beta_{KSST}(x)$ onto the SST data at time step i.

5. The amplitude of $\beta_{KSST}(x)$ (and thus $\beta^*_{KSST}(x,t)$) is very weak outside the western North Pacific (Figure 2.1a). Nevertheless, to ensure SST anomalies outside the North Pacific do not

influence the model response, we set all values in $\beta^*_{KSST}(x,t)$ to zero outside the region 5°N-65°N and 115°E -115°W. An 11-degree running average is applied at the boundary of the region to avoid any discontinuities in the SST field. The resulting pattern is shown in the bottom of Figure 2.1.

6. The global SST boundary forcing used in the KOGA experiments is formed by adding a) the matrix of time-varying SST anomalies given by $\beta^*_{KSST}(x,t)$ and b) the annually-repeating, climatological-mean seasonal cycle of SSTs. As such, the experiment is forced by the time-varying evolution of the pattern shown in the bottom panel of Figure 2.1 superposed on the annually-repeating climatological-mean SST field.

The KOGA simulations are integrated over the period 1901-2015. The experiments were repeated five times to yield a total sample size of 575 years. The KOGA results are also compared with output from a global-ocean/global-atmosphere (GOGA) AMIP-style experiment forced with prescribed time-varying SSTs from across the globe. The GOGA experiments were run on NCAR CAM5 with a horizontal resolution of 0.9°×1.25°. SSTs and sea-ice were derived from ERSSTv4 and HadISST1. We analyze 10 ensemble members run over the period 1880-2014. The GOGA runs were conducted by the NCAR Climate Variability & Change Working Group and are available from the NCAR Climate Data Gateway.

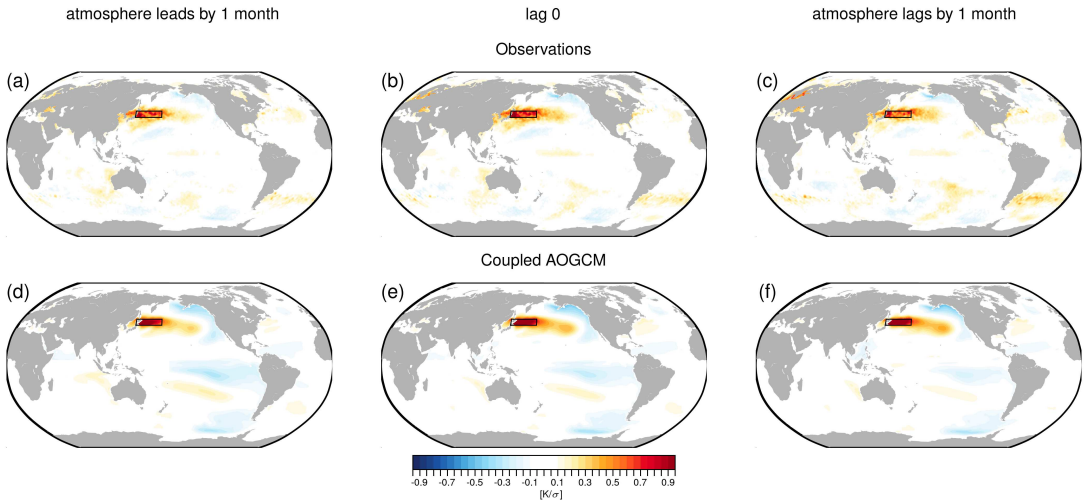

Figure 2.2: The global pattern of SSTs regressed on the K index time series. That is: Results show SST anomalies regressed on the K index based on the observations (top) and the coupled AOGCM (bottom).

2.2.3 Analysis Details

Anomalies are defined as deviations from the long-term mean annual cycle. All observations are linearly detrended to remove the influence of trends on the results. Sea level pressure (SLP) is expressed as geopotential height at 1000 hPa (Z_{1000}). Area averages are weighted by pressure and cosine of latitude as necessary. Lag regression analyses are centered on December-February (DJF), thus results at, e.g., lag - 1 indicate monthly values for November-January regressed on monthly values for December-February.

For the KOGA and GOGA simulations, the regression analyses are conducted first for individual ensemble members and then the resulting regression coefficients are averaged over all ensembles. The results based on the KOGA simulations are thus derived from 5 ensemble members × 115 years/ensemble × 3 months/year = 1725 time steps. For the coupled AOGCM simulations, the regression analyses are conducted for output concatenated from all 40 ensemble members and thus over 4920 time steps (40 ensemble members × 41 years/ensemble × 3 months/year).

Statistical significance for key results is shown in Figure 2.21 and Figure 2.22. Figure 2.21 and Figure 2.22 show results from the top rows in Figs. 2.3-6 (Figure 2.21) and from Fig. 2.8 (Figure 2.22) superposed with stippling where the significance of the results exceeds the 95% level. See Section 2.2 for details of the calculation of significance. The significance of a regression coefficient is assessed by 1) applying Student's t-statistic to the associated correlation coefficient r; and 2) assuming

$$n\frac{1-r_1r_2}{1+r_1r_2}$$

degrees of freedom, where n is the number of timesteps, and r_1 and r_2 are the lag-one autocorrelations of the time series being correlated [Bretherton et al. (1999)].

2.3 Results

Figure 2.3 shows the standard deviations of the SST field derived from observations (i.e., ERA5), the coupled simulation, and the KOGA simulation. Note that the standard deviations in panels b) and c) are found for individual ensemble members and then averaged over all

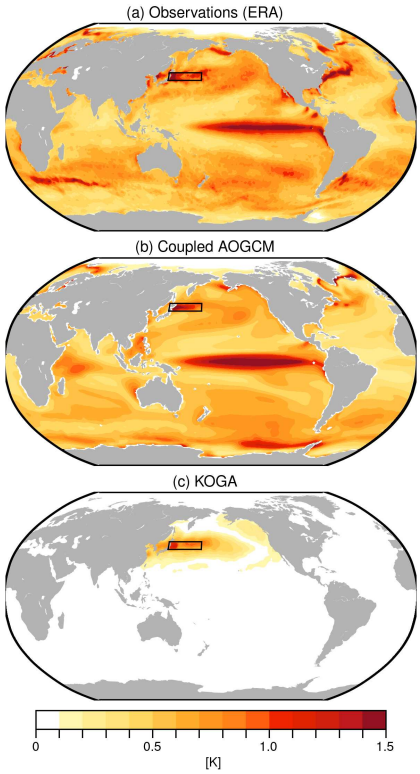

Figure 2.3: Standard deviations of the SST anomaly field in observations (ERA5 over 1979-2020), the coupled AOGCM (CESM1) and the KOGA experiment.

ensembles. The ERA5 SSTs are constrained by observations Hersbach et al. (2020), and indicate that the regions of largest SST variances are located in the eastern tropical Pacific and in the Kuroshio, Gulf Stream and Agulhas return current regions (Figure 2.3a). The coupled AOGCM (Figure 2.3b) reproduces broadly the pattern of observed SST variances, albeit there are differences in the amplitude and structure of the SST variances over regions of large variance, including the western North Pacific. These differences are discussed more below. The variances from the KOGA experiment (Figure 2.3c) arise from the time evolution of the $\beta^*_{KSST}(x,t)$ pattern and are by construction centered on the North Pacific region.

In the rest of this section, we explore the lead/lag relationships between SST variability over the North Pacific and the large-scale atmospheric circulation in the observations and both numerical configurations. The basis for the lag regressions is the K index time series, which as noted in Section 2.2 is defined as standardized values of detrended SST anomalies averaged over the western North Pacific (black boxes in Figure 2.3). The K index time series is normalized by

the spatially averaged SST variability over the KOE region for all-months. We begin with lag regressions derived from the observations.

The top row of Figure 2.5 shows the lag regressions of ERA5 SLP (contours) and SSTs (shading) onto the ERA5 K index time series. The lags range from minus one month (left column) to plus one month (right column) months. The results are a reproduction of the key finding from WT18 but for monthly-mean data. By construction, the largest SST anomalies are found in the western North Pacific in the vicinity of the Kuroshio/Oyashio Extension region. The SST anomalies are very similar at all lags, consistent with the persistence of the SST field. In contrast, the atmospheric circulation anomalies change notably from one lag to the next. The month prior to peak positive anomalies in KOE region is marked by positive SLP anomalies that span much of the North Pacific basin (Figure 2.5, top left); the month following peak positive anomalies in KOE region is marked by low SLP anomalies that overlie and extend downstream of the KOE region (Figure 2.5, top right). The primary SLP anomalies in both patterns are statistically significant (Figure 2.21).

For completeness, results for lags extending from lag -3 to +5 are shown in Figure 2.11. The region of positive SLP anomalies at negative lag is evident as early as lag -3 but peaks in amplitude at lag -1 months. The region of low SLP anomalies at positive lag is apparent at lag +2 but shrinks notably beyond that.

The atmospheric anomalies at negative lag are consistent with anomalously warm advection over the region of large SST gradients in the Kuroshio/Oyashio extension region [see also Deser and Timlin (1997); Ciasto and Thompson (2004); WT18). The SLP anomalies at negative lag are thus consistent with atmospheric forcing of the SST field. In contrast, the atmospheric anomalies at positive lag indicate anomalously cold advection over the western North Pacific. They are thus consistent with the linear atmospheric response to the SST field, in which the surface fluxes associated with SST anomalies are balanced by horizontal temperature advection [Hoskins and Karoly (1981)]. The maximum amplitude of the anomalies at positive lag is about $\sim$12m in Z_{1000} (1.5 hPa in SLP) per standard deviation of the K index time series in observations. These

amplitudes correspond to roughly 7% (27%) of the variance (standard deviation) of the observed January-February-March SLP variability near the low pressure center of action in the western North Pacific (Figure 2.4).

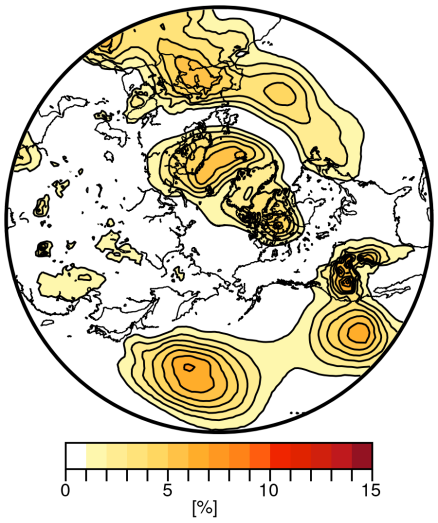

Figure 2.4: The ratio of variance (r-squared values) in observed JFM SLP explained by the DJF KOE index.

The interpretation of the SLP pattern at positive lag as the atmospheric "response" is supported by the projection of the attendant surface turbulent heat flux anomalies onto the SST anomalies. Figure 2.6 (top) shows the product of 1) the surface fluxes of sensible and latent heat regressed onto the K index and 2) the SST anomalies in Figure 2.5 (top). Note that multiplying the fluxes and SST anomalies emphasizes regions where the fluxes contribute to the SST anomalies of interest; results not weighted by the SST anomalies are shown in Figure 2.7. Regions where the product is positive indicate areas where the SST anomalies are reinforced by the surface fluxes; regions where the product is negative indicate areas where the SST anomalies are damped by the surface fluxes. As evidenced in the figure, the period prior to peak SST anomalies is associated with warming of the ocean mixed layer by the atmosphere, whereas the period following peak SST anomalies is associated with warming of the atmosphere by the ocean.

Interestingly, the lag zero regression map can be viewed as the linear superposition of the forcing (lag -1) and response (lag +1) patterns. To see this, the bottom two rows of Figure 2.5

show the decomposition of the SLP lag-regression maps into 1) the "forcing" pattern and 2) a component linearly independent of the forcing pattern. The decomposition is done as follows: 1) The "forcing" pattern is defined as the SLP regression map at lag -1 month (Figure 2.5, top left). 2) The amplitude of the forcing pattern is found at each lag as the (spatial) regression of the respective SLP regression map onto the forcing pattern. This yields the component of the SLP regression map that is linearly congruent with the forcing pattern at each lag. And 3) The residual "response" patterns are found by subtracting the linearly congruent component of the forcing pattern from the SLP regression maps.

The decomposition is shown in the second and third rows of Figure 2.5 and highlights two key results:

1) The forcing pattern accounts for the entirety of the total regression map at lag -1, by construction (Figure 2.5, left column). But its amplitude decreases with lag and is negligible at lag +1 (middle row). Thus the full regression map at lag -1 (top left) and lag +1 (top right) are effectively linearly independent of each other.

2) The residual regression maps are very similar at lag 0 and lag +1, despite the fact they are not constrained to be so. Thus the residual patterns are largely dominated by a single structure, and the lag regressions in the top row can be viewed as the time-varying linear superposition of two distinct structures.

Figure 2.8 explores the corresponding lead/lag relationships in the coupled AOGCM model output. As noted earlier, the coupled AOGCM captures well the observed SST variability over most of the globe albeit with some differences on the basin scale. There are two prominent differences between the coupled AOGCM output and the observations over the North Pacific SST field: 1) The largest SST variability in the western North Pacific in the AOGCM is located a few degrees poleward of the observational maximum [compare Figure 2.3a and Figure 2.3b; see also Small et al. (2019); Thompson and Kwon (2010)]. For this reason, the K index time series for the coupled AOGCM is based on SSTs averaged over a region shifted 3 deg. poleward of that used for the observations (as indicated by the box in Figure 2.3b). 2) The SST variances in the western

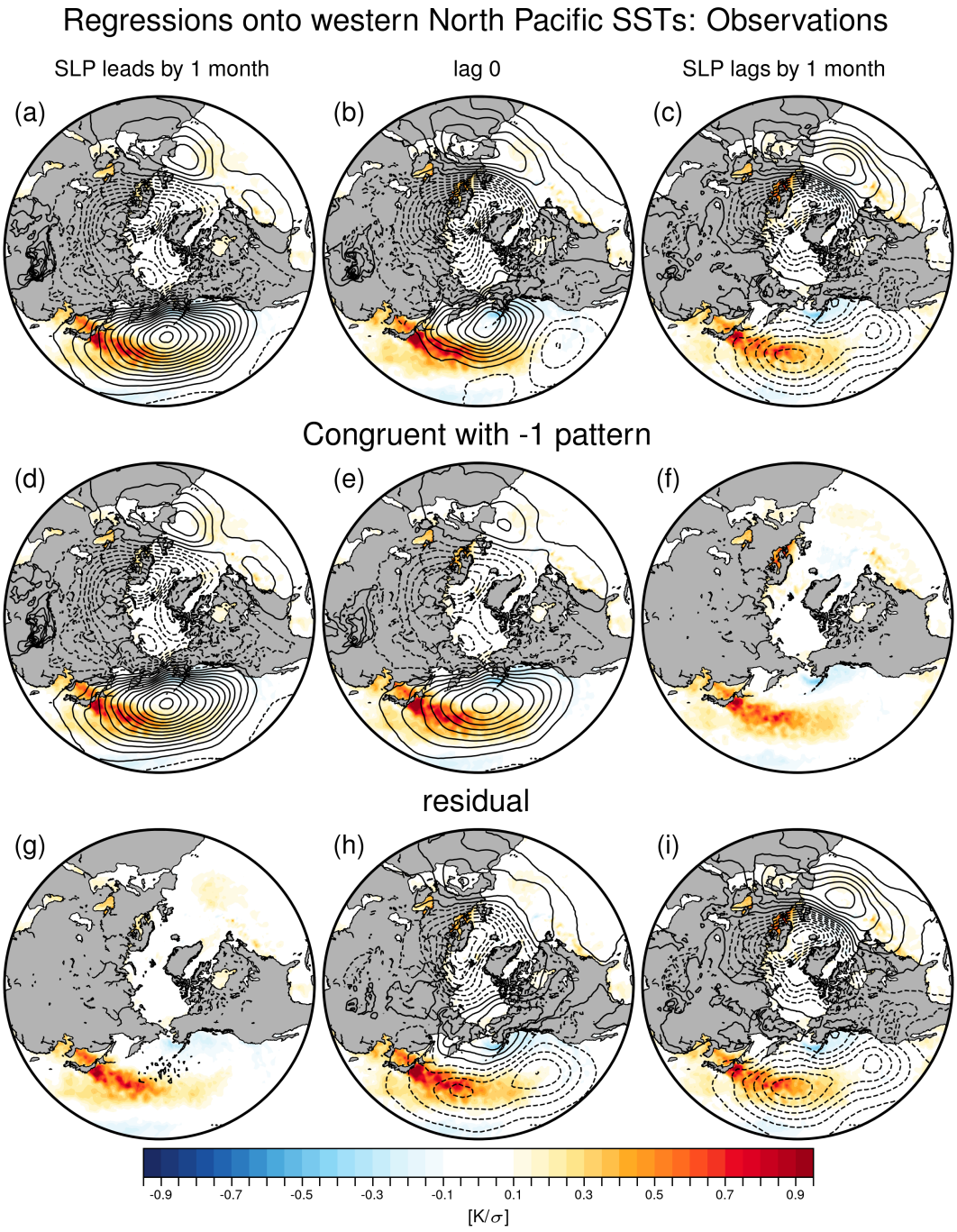

Figure 2.5: (a)-(c) Observed wintertime lag regressions of the SST and Z_{1000} fields onto standardized values of the K index time series. Negative lags denote Z_{1000} and SST anomalies lead the K index time series, and vice versa. (d)-(f) As in (a)-(c), but the Z_{1000} contours show the components of the Z_{1000} regression coefficients that are linearly congruent with the pattern in (a). (g)-(i) As in (d)-(f), but the Z_{1000} contours show the differences between the Z_{1000} anomalies in (a)-(c) and (d)-(f). The SST field is indicated by shading, and the Z_{1000} field is indicated by contours. Solid (dashed) contours indicate positive (negative) anomalies. The Z_{1000} contours are spaced at 2-m intervals starting at ± 1 m. The same contour intervals are used in other figures throughout the chapter except where otherwise noted.

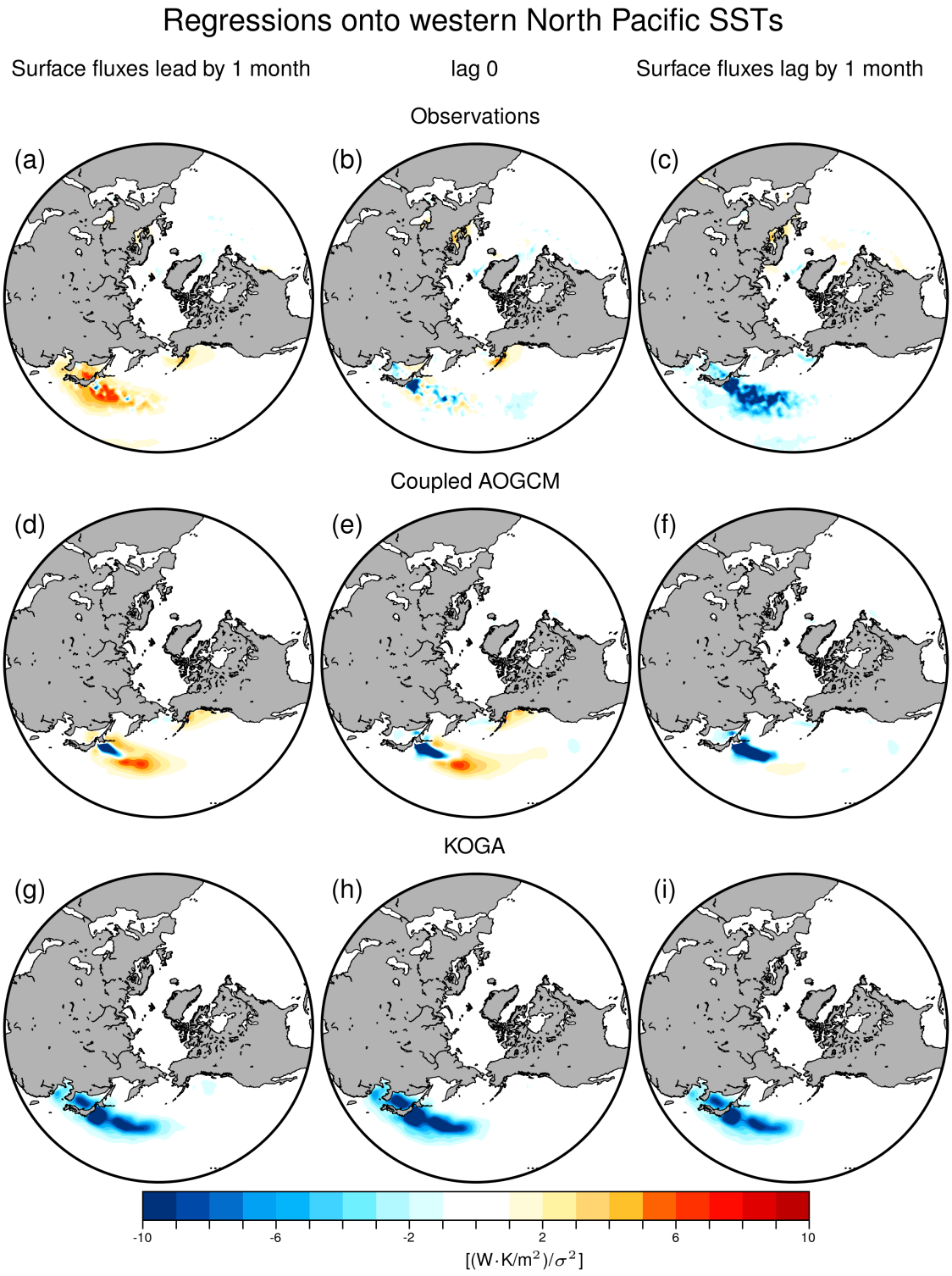

Figure 2.6: The product of 1) the surface fluxes of sensible and latent heat and 2) SSTs regressed onto the K index time series. Results are shown for (a)–(c) observations, (d)–(f) the coupled AOGCM output, and (g)–(i) the KOGA output. Regions where the product is positive (negative) indicate areas where the SST anomalies are reinforced (damped) by the surface fluxes.

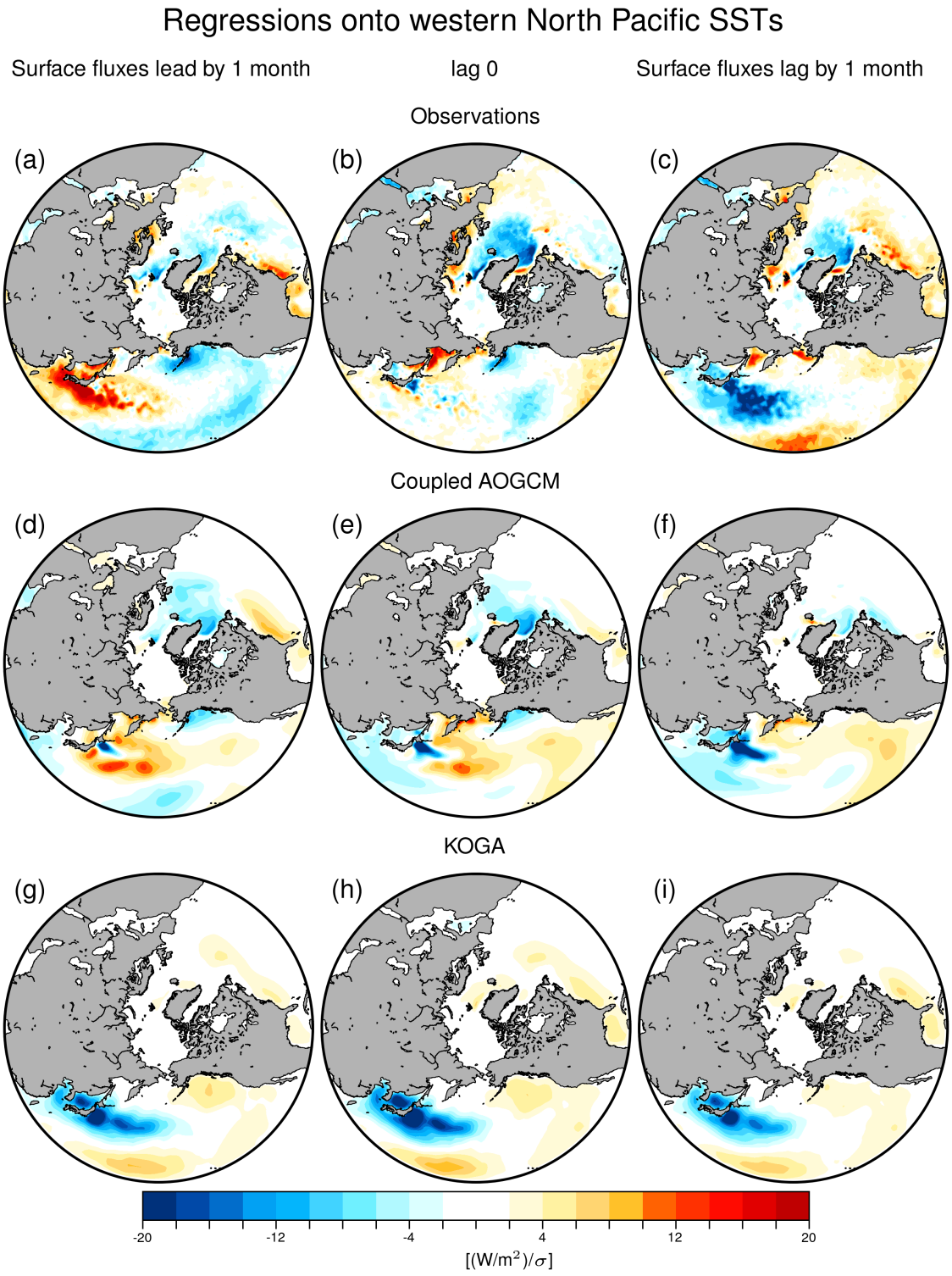

Figure 2.7: The surface fluxes of sensible and latent heat regressed onto the K index time series. Results are shown for observations (top), the coupled AOGCM output (middle), and the KOGA output (bottom). Regions where the fluxes are positive (negative) indicate areas where surface fluxes are into the ocean (atmosphere).

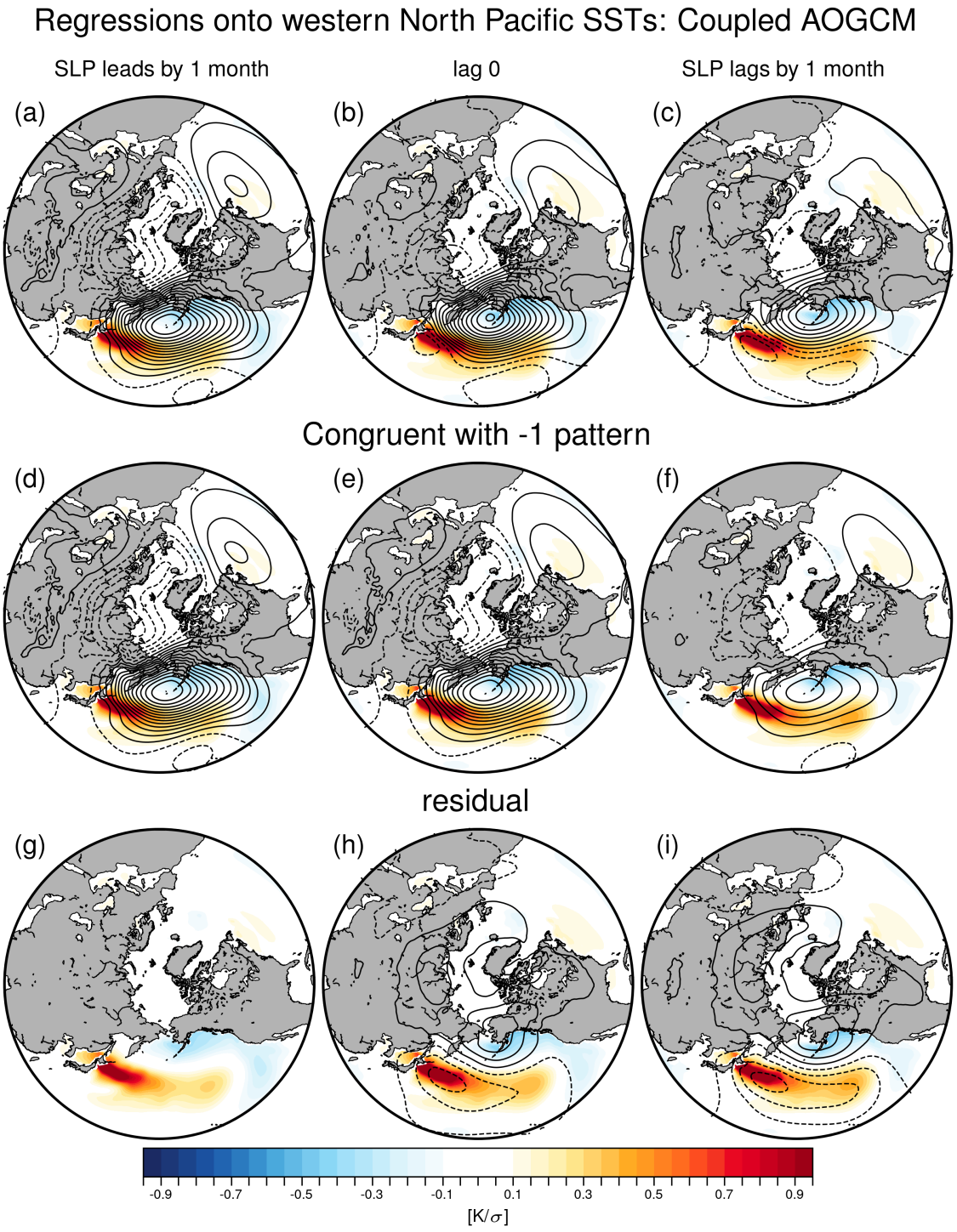

Figure 2.8: As in Figure 2.5, but for output from the coupled AOGCM (CESM1). The Z_{1000} contours are spaced at 2-m intervals starting at ± 1 m.

North Pacific are slightly larger in the AOGCM than they are in the observations. For example, the standard deviations of SSTs averaged over the K index time series region for the DJF period (i.e., the standard deviations of the K index time series) are 0.82 K in the AOGCM output and 0.73 K in the observations, and the averages of the grid-point standard deviations over the same region are 1.0 K in the coupled AOGCM and 0.85 K in the observations. The larger variances in the coupled AOGCM output are consistent with biases in the model SST response to both oceanic [Thompson and Kwon (2010)] and atmospheric processes [Small et al. (2019); Small et al. (2020)]. Neither of these differences qualitatively affect the results of the regressions (not shown).

The lag -1 regression map derived from the coupled AOGCM (Figure 2.8, top left) is qualitatively similar to that derived from observations (Figure 2.5, top left). Both are dominated by statistically significant SLP anomalies consistent with northward flow and thus warm temperature advection over the region of large SST gradients in the Kuroshio/Oyashio extension region (significance is shown in Figure 2.21).

The lag +1 regression map derived from the coupled AOGCM (Figure 2.8, top right) also bears similarity to its observational counterpart (Figure 2.5, top right) in that both exhibit negative SLP anomalies across the North Pacific. However, it also exhibits notable differences, in particular the coupled AOGCM map exhibits positive SLP anomalies over the Bering Sea that are not apparent in the observations. The decomposition of the coupled model results into a "forcing" (Figure 2.8 middle row) and residual (Figure 2.8 bottom row) pattern - as done for observations in Figure 2.5 - reveals that the differences between the observed and coupled AOGCM lag +1 regression maps derive not from differences in the response pattern, but from differences in the persistence of the forcing pattern. Comparing the middle rows of Figure 2.5 and Figure 2.8, it is clear that the forcing pattern persists much longer in the coupled AOGCM than it does in observations. When the projection of the forcing pattern is removed from the coupled AOGCM regression maps (Figure 2.8 bottom), the residual pattern is more clearly dominated by low SLP anomalies that span the central North Pacific and increase in amplitude with lag.

The enhanced persistence of the forcing pattern in the coupled AOGCM potentially derives from model biases in the persistence of SLP variability in the North Pacific sector. The enhanced persistence of the forcing pattern, in turn, leads to enhanced persistence of the corresponding SST anomalies. The longer time scale of SST anomalies in the western North Pacific in the coupled AOGCM is apparent in Figure 2.11; the longer time scale of SLP anomalies is evidenced in the differences in the lag-one autocorrelations of SLP averaged over the North Pacific sector bounded by 35-70°N and 150°E-130°W: the lag-one month autocorrelation in the coupled AOGCM output is r$\sim$0.3; the lag-one month autocorrelations in observations in r$\sim$0.2.

To leading order, the relative signs of the surface heat fluxes and SST anomalies in the coupled AOGCM are qualitatively similar to those derived from observations [compare Figure 2.6, top and middle rows; see also Figure 2.7): The fluxes generally reinforce the SST anomalies at negative lag (as evidenced by warm shading in Figure 2.6] but damp the SST anomalies at positive lag (as evidenced by cool shading). Note that regions where the relationship between the surface heat fluxes and SSTs are out-of-phase - as indicated by the blue shading - are centered primarily over the KOE frontal region, where the air-sea flux variability is driven predominantly by SST variations arising from intrinsic oceanic variability [Small et al. (2019)]. The AOGCM indicates a small region where the SSTs are damped by the surface fluxes over the KOE region that is not evident in the observations (see the small region of blue shading near the coast of Japan), which suggests the CESM overestimates the contribution of oceanic processes to SST variability in this region.

Together the results in Figure 2.5-Figure 2.8 indicate that:

a) Lag regressions between the SLP field and SSTs averaged over the western North Pacific consist of two distinct patterns: 1) a pattern consistent with forcing of SST anomalies over the KOE region by horizontal atmospheric temperature advection that peaks at negative lag; and 2) a pattern consistent with damping of SST anomalies over the KOE region by horizontal atmospheric temperature advection that peaks at positive lag and is consistent with the linear atmospheric response to midlatitude SST anomalies. The response pattern is most clear when the

component of the regressions that is linearly congruent with the forcing is subtracted from the lag regression maps [Figure 2.5 and Figure 2.8, bottom].

b) Results based on both observations and coupled model output are very similar. The primary differences derive from the persistence of the model "forcing" pattern, which exhibits larger persistence than its observational counterpart, and thus partially obfuscates the coupled model response pattern at positive lag [Figure 2.8 right column].

To what extent is the atmospheric response - as inferred from the results in the bottom right panels of Figure 2.5 and Figure 2.8 - recovered in the experiment forced with the time history of SST anomalies over the western North Pacific? Figure 2.9 is constructed in the same manner as the top rows of Figure 2.5 and Figure 2.8, but shows results based on the KOGA simulation. Recall that the KOGA simulation is forced by the climatological-mean, seasonal cycle of SSTs throughout the globe superposed on the time evolution of the pattern of SST anomalies shown in Figure 2.1. Note that the regression coefficients based on the KOGA output are calculated first for individual ensemble members and then averaged over all ensembles. Thus the amplitudes can be compared directly with the observations and coupled model output.

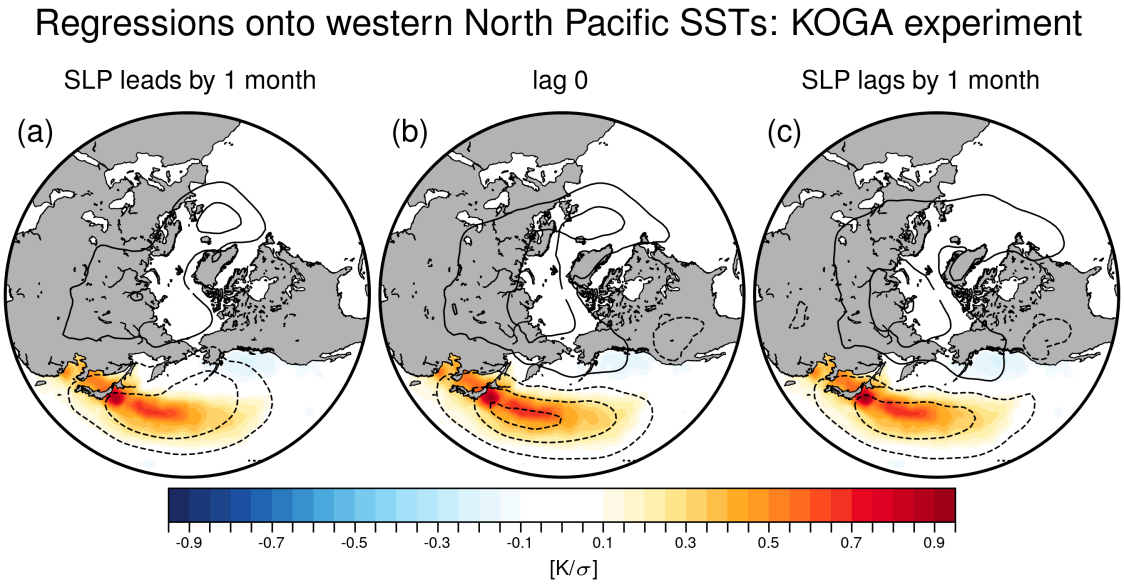

Figure 2.9: As in Figure 2.5a-c, but for output from the KOGA simulation. The Z_{1000} contours are spaced at 2-m intervals starting at ± 1 m.

The KOGA results do not exhibit a distinct atmospheric forcing pattern at negative lag - i.e., they do not exhibit a pattern consistent with warm advection over the western North Pacific. This is expected, since the model is forced with prescribed SST anomalies, and thus horizontal temperature advection by the atmosphere is incapable of influencing the SST field. Rather, the KOGA results indicate a pattern consistent with the atmospheric response at all lags. That is: At all lags, the KOGA output indicates 1) heat fluxes that act to damp the SST field and thus warm the lower atmosphere (Figure 2.6 bottom) and 2) SLP anomalies consistent with cold advection over the western North Pacific (Figure 2.9) that act to balance the surface fluxes.

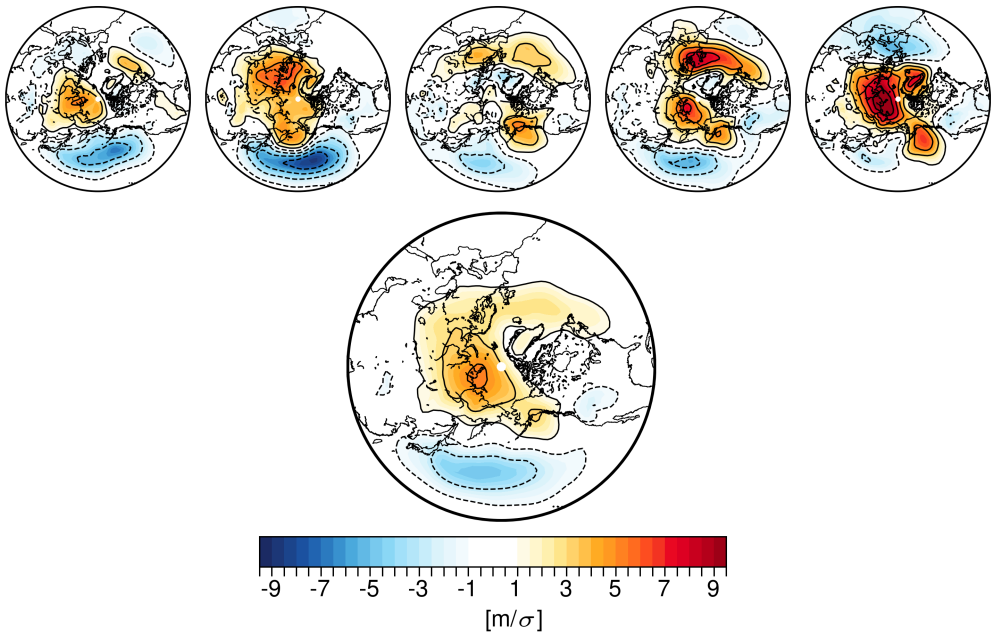

Figure 2.10: (top) Wintertime lag regressions of the Z_{1000} field onto the K index time series at lag +1 from each ensemble member in the KOGA run. (bottom) The ensemble-mean lag +1 regression coefficients from the KOGA run reproduced from the contours in Figure 2.9c. Shading and contours both indicate the Z_{1000} field.

The close similarity between the atmospheric response in the KOGA simulation (Figure 2.9) and the inferred atmospheric response from observations (Figure 2.5i) suggests that the latter reflects the observed atmospheric response to SST anomalies over the western North Pacific. In both the KOGA simulation and observations, the low level circulation anomalies are consistent with the linear, balanced response to extratropical SST anomalies; that is, the surface low is

shifted to the east of warm SST anomalies so that horizontal temperature advection over the Kuroshio/Oyashio extension region acts to oppose the anomalous fluxes of heat into the lower atmosphere and thus damp the underlying SST anomaly.

The response in the KOGA experiments is highly reproducible and significant. The regression coefficients in the primary center of action are significant based on the t-statistic (Figure 2.21). The low pressure center of action varies in amplitude from one ensemble member to the next, but its primary center over the western half of the North Pacific is reproducible in all five ensemble members (Figure 2.10). Importantly, the response is consistent with the observational and coupled model results shown in Figure 2.5 and Figure 2.8 (bottom right). The amplitude of the KOGA SLP anomalies is somewhat less than the amplitude of the residual SLP anomalies from observations and the coupled AOGCM output (compare Figure 2.9 right with Figure 2.5 and Figure 2.8 bottom right). But the general patterns of the observed, coupled AOGCM, and KOGA SLP anomalies are all clearly very similar to each other.

Figure 2.12 probes the vertical structure of the responses. The bottom row reproduces the responses in Z_{1000} from the observations, coupled AOGCM, KOGA and GOGA experiments. That is, the figure shows the lag +1 results reproduced from (first column) the observations from Figure 2.5i, (second column) the coupled AOGCM output from Figure 2.8i, (third column) the KOGA output from Figure 2.9c, and (fourth column) the GOGA output. The top row shows the same results but for results based on the Z_{500} field. The Z_{500} regression coefficients in Figure 2.12a and b were calculated in the same way as those in the bottom right panels of Figure 2.5 and Figure 2.8, i.e., they are the differences between the Z_{500} lag +1 regression maps and the components that are linearly congruent with the Z_{500} lag -1 regression maps.

The circulation anomalies derived from the KOGA output (right column) peak in the lower troposphere, again consistent with the linear baroclinic response to extratropical SST anomalies [Hoskins and Karoly (1981); Kushnir et al. (2002)]. However, in contrast, the circulation anomalies derived from observations and the coupled AOGCM output (left and middle columns) exhibit equivalent barotropic structures with more pronounced anomalies aloft.

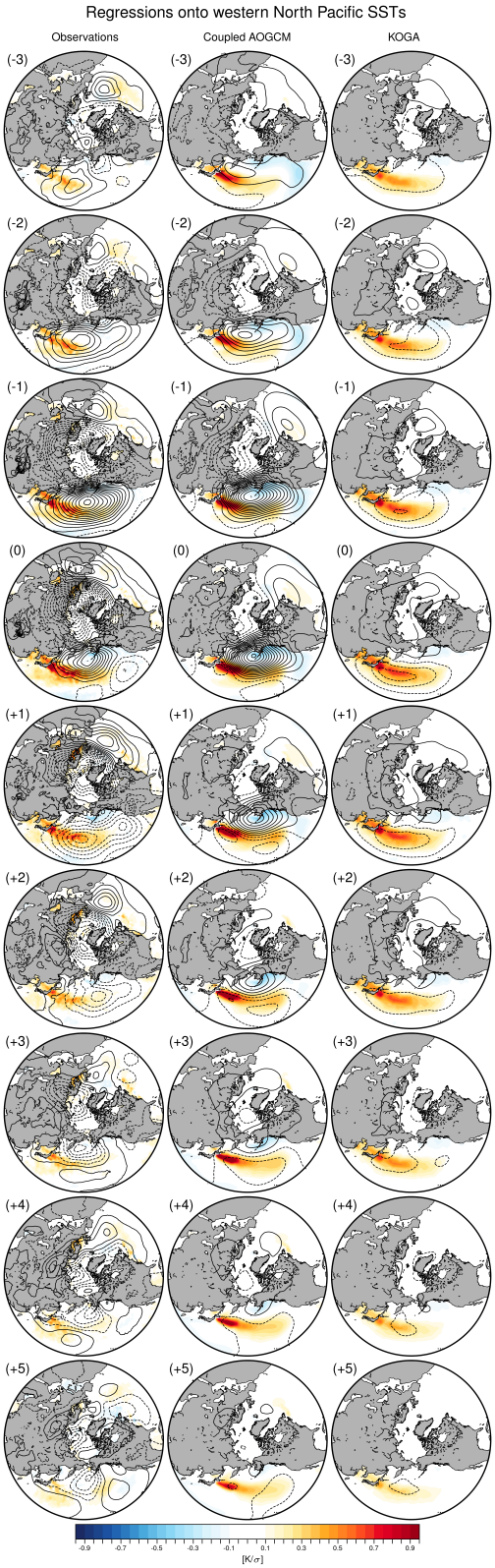

Figure 2.11: The evolution of the SST and Z_{1000} fields regressed onto the K-SST index in (left) the observations, (middle) the coupled AOGCMs, and (right) the KOGA runs. The Z_{1000} contours are spaced at 2-m intervals starting at ± 1 m.

Why do the observations and coupled AOGCM indicate an equivalent barotropic response while the KOGA output indicates a shallow response? One possibility is that the upper tropospheric anomalies in the observations and coupled AOGCM arise from SST anomalies that lie outside the western North Pacific, such as the tropical Pacific. We view this as unlikely for two reasons: 1) SST anomalies regressed on the K index time series do not exhibit notable amplitude outside the North Pacific (Figure 2.2); and 2) Analogous results formed from AMIP-style experiments forced with SST anomalies across the globe (the GOGA runs described in Section 2.2) also do not reveal notable anomalies aloft (Figure 2.12). The similarity between results derived from the GOGA and KOGA simulations suggest that SST anomalies in the KOE region dominate the results from the GOGA output.

A second possibility is that the upper level response is muted in the KOGA run due to insufficient horizontal resolution. Previous studies have shown that high horizontal resolution is required to correctly represent the coupling between mesoscale ocean eddies and the extratropical atmospheric circulation [Czaja et al. (2019); Ma et al. (2015); Ma et al. (2017); Smirnov et al. (2015); Small et al. (2014); Small et al. (2019); Siqueira and Kirtman (2016)] and that it also leads to a more robust upper tropospheric response [Smirnov et al. (2015)]. However, it is notable that the GOGA run has the same horizontal resolution as the coupled AOGCM but nevertheless exhibits a very different response aloft.

A third possibility is that the upper level response is influenced by the temporal resolution of the SST boundary conditions. For example, Zhou et al. (2015) argue that daily fluctuations in the SST field play an important role in generating a realistic simulation of the large-scale atmospheric response. The SST boundary conditions in the KOGA run include monthly mean SST values linearly interpolated to the daily timescale. They thus lack realistic variability on sub-monthly timescales.

A fourth possibility is that the upper level response evident in the observations and coupled AOGCM is dependent on two-way coupling between the atmosphere and SST field. This could be tested by conducting experiments analogous to the KOGA simulation but where we prescribe

time-varying anomalous fluxes of heat in the ocean mixed-layer in the KOE region rather than the SST field itself, thus permitting thermodynamic coupling at the sea-surface.

It would be interesting to explore the sensitivity of the atmospheric response in KOGA-like experiments run at different horizontal resolutions, realistic daily variations in the SST field, and forced with prescribed ocean heat fluxes rather than prescribed SSTs [i.e., as in Kwon et al. (2011)]. These experiments are deferred to a future study.

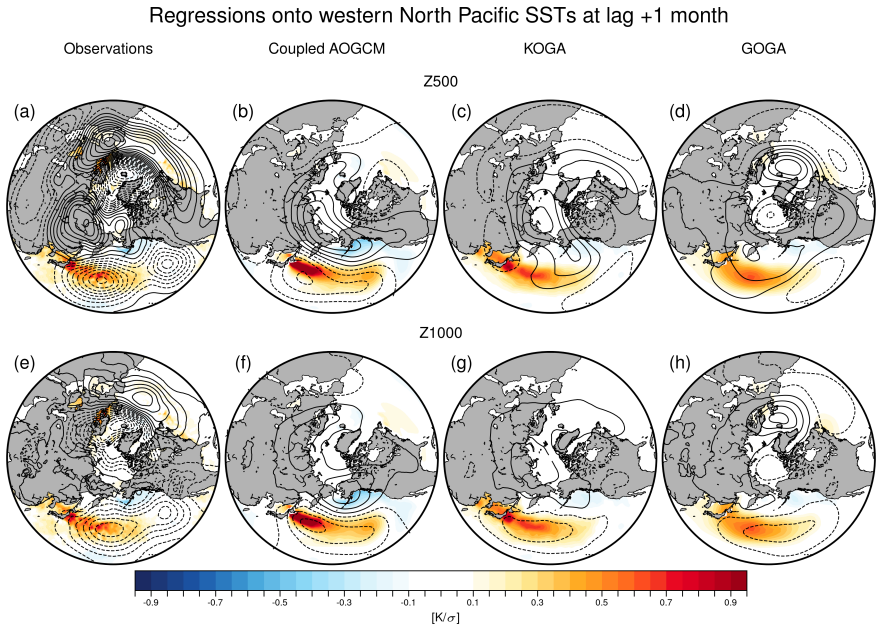

Figure 2.12: (e)–(h) Wintertime lag regressions of the Z_{1000} and SST fields onto the K index time series lag +1 based on observations, the coupled AOGCM (CESM1), the KOGA, and the GOGA experiment. The Z_{1000} results in (e) and (f) show the components of the regression coefficients that are linearly unrelated to the lag -1 regressions; that is, they show the "residual" regression coefficients reproduced from Figure 2.5i and Figure 2.8i, respectively. (a)–(d) As in (e)–(h), but for results based on the Z_{500} field. The Z_{1000} and Z_{500} contours are spaced at 2-m intervals starting at ± 1 m.

We have further explored the atmospheric circulation anomalies arise from SST anomalies that lie outside the western North Pacific. We have conducted the additional analyses of Global Ocean-Global Atmosphere (GOGA) and Tropical Ocean-Global Atmosphere (TOGA) runs using AMIP experiments as listed below:

1) NOAA FACTS AMIP CAM5 historical simulations [Murray et al. (2020); Hurrell et al. (2008)]. The atmospheric model of GOGA-FACTS is driven by observed SSTs and sea ice [Hurrell et al. (2008)]. We analyze the period 1979-2019 and use 40 ensemble members.

2) NCAR CAM5 Prescribed SST AMIP Ensembles: i) TOGA runs forced by time-varying SSTs over the tropics (28S:28N) and climatological SSTs elsewhere derived from ERSSTv3b, ERSSTv4, and ERSSTv5 (10 ensemble members for each SST dataset; TOGA-NCAR), and ii) GOGA runs forced with global time-varying observational SSTs from the ERSSTv4 (10 ensemble members; GOGA-NCAR). HadISST1 was used for the ice forcing dataset both in TOGA and GOGA runs. We analyze the period 1880-2005 in historical simulations and 2006-2014 under RCP85 scenario.

All simulations are run in a horizontal resolution of 0.9°×1.25°. As in other analyses, the linear trend and seasonal cycle is subtracted from SSTs and atmospheric fields in each respective SST dataset prior to the regression analyses. In TOGA-NCAR runs, the regression analyses are conducted for output concatenated from all 30 ensemble members. The latitudinal domain in Figure 2.13 and Figure 2.14 has been extended to the equator to cover the correlated SST anomalies over the tropics.

The GOGA-FACTS output shows low pressure anomalies over the North Pacific in the lower troposphere, consistent with the linear responses shown in KOGA run (Figure 2.13 and Figure 2.12).

Atmospheric circulation anomalies in response to the tropical SSTs during the period over 1880-2014 exhibit are weaker in amplitudes (Figure 2.14b and d). Atmospheric responses to the global SST during the same period are consistent with linear response shown in other AMIP-style simulations (Figure 2.13 and Figure 2.12), and the responses are not showing the barotropic structure (Figure 2.14a and b).

Thus, results from AMIP-style simulations (KOGA, GOGA, and TOGA runs) indicate that (Figure 2.9, Figure 2.13, and Figure 2.14) AMIP style simulations forced with historical SSTs over the extratropics exhibit the shallow but robust local responses over the North Pacific. The

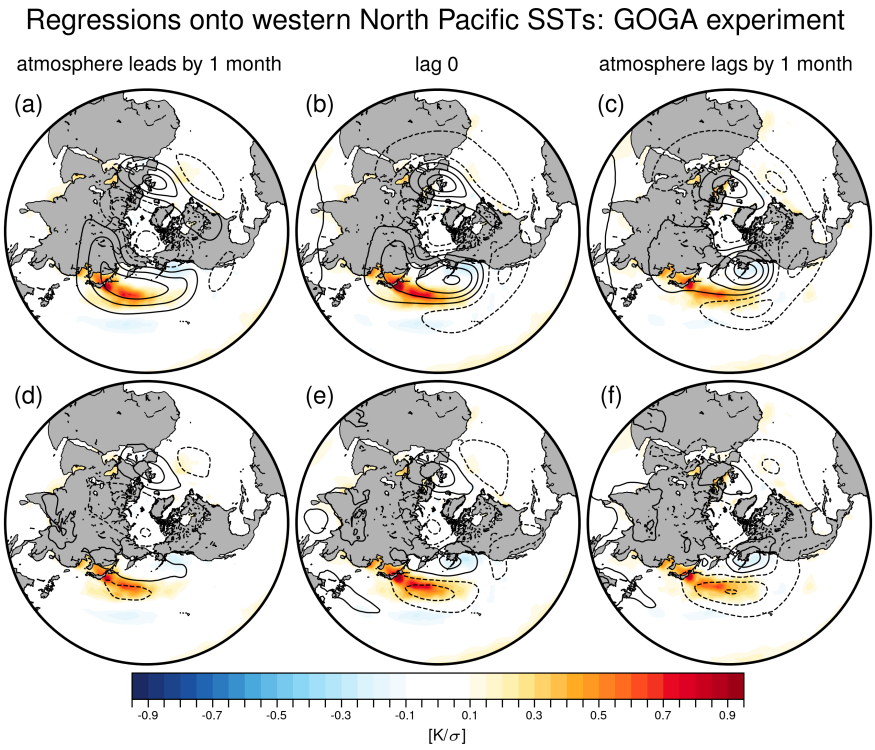

Figure 2.13: Z_{500} (top) and Z_{1000} (bottom) responses to the KOE SST anomalies at different lag based on the GOGA-FACTS runs during 1979-2019

difference in the upper level responses between observations and AMIP-style experiments may also indicate the inability of the standard resolution CAM5 in AMIP-style configuration to reproduce the upper-level response to the KOE SSTs as suggested by Smirnov et al. (2015).

Figure 2.14 shows the atmospheric circulation responses in the lower and upper levels based on the GOGA-NCAR and TOGA-NCAR output over the period of 1880-2014.

We tried to remove the ENSO signal using simple linear regression method. We defined the Niño-3.4 index as averaged SST anomalies over the region 5°S-5°N, 170-120°W. Then, we identified the time lag when the time series of SLP anomalies at each grid point and the Niño-3.4 index time series shows the maximum correlation. The linear-regression of SLP at each grid point associated with the Niño-3.4 index was subtracted to the original SLP anomalies to form the ENSO-residual SLP. We repeated the analyses using the ENSO-residual SLP data. However, removing the linear regression associated with the ENSO from the SLP data does not change the

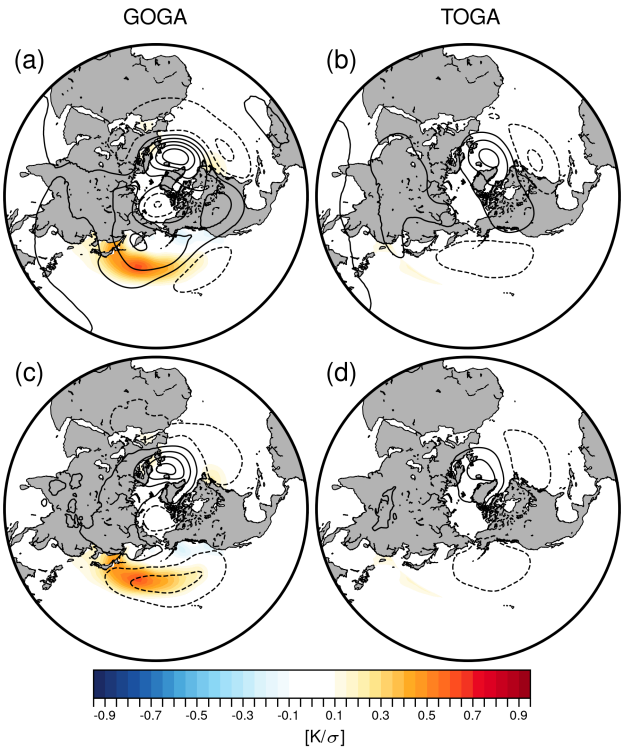

Figure 2.14: Z_{500} (top) and Z_{1000} (bottom) responses to the KOE SST anomalies at +1 lag based on the GOGA-NCAR (left) and TOGA-NCAR (right) runs during 1880-2014.

overall results. This is also consistent with Wills and Thompson (2018) who used similar approach using ERA-Interim daily time series.

We have repeated the analyses based on the fully-coupled configuration of CESM1 run on different horizontal resolutions:

1) a high-resolution configuration of the CESM version 1.3 with a nominal horizontal resolution of 0.25° for the atmosphere and 0.1° for the ocean and sea-ice models (HR; Chang et al. (2020)), and

2) a standard-resolution configuration of the CESM1 with a nominal 1-degree horizontal resolution of atmosphere and ocean models (LR; Hurrell et al. (2013)). The results are derived from a 500 (1500) years of preindustrial control simulations in HR (LR).

The results based on the Coupled AOGCM runs were not sensitive to the horizontal model resolution (Figure 2.15 and Figure 2.16). However, the results based on the Coupled AOGCM runs cannot be used to conclude the resolution dependency in the AMIP-style simulations, given

the differences between those configurations in their representation of SST variability and air-sea interactions. This issue can only be properly addressed with sensitivity experiments run on AMIP-style experiments with different horizontal resolutions. We deferred it to future work, due to limitations in computational resources in the current project.

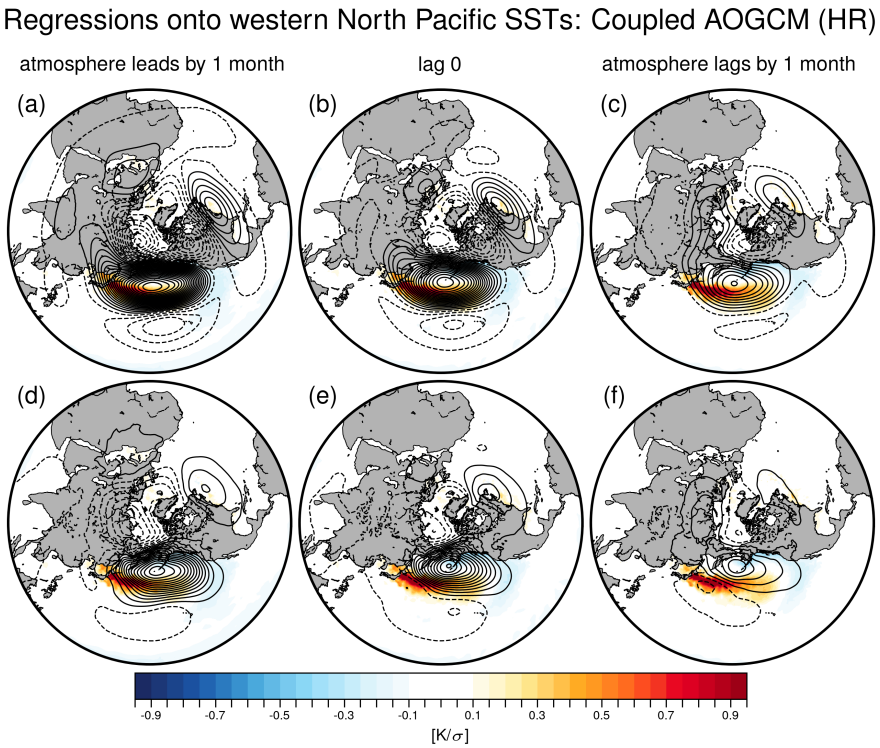

Figure 2.15: Z_{500} (top) and Z_{1000} (bottom) responses to the KOE SST anomalies at different lag based on the low resolution (HR) version of the Coupled AOGCM preindustrial control simulation.

We have also conducted the additional analyses to investigate the evolution of the atmospheric circulation (Z1000) anomalies at lags -3 to +5 months (Figure 2.11). The atmospheric forcing pattern begins to develop since lag -2 months both in the observation and in Coupled AOGCM. The basin-wide atmospheric response pattern becomes strongest at lag +1, then quickly breaks down quickly since lag +2 in the observation and similarly in the KOGA results. However, the atmospheric response persisted longer up to lag +3 months in the Coupled AOGCM results.

We attribute the persistent atmospheric response pattern in the Coupled AOGCM to potential model biases in the representation of the SST variability over the KOE region associated with the

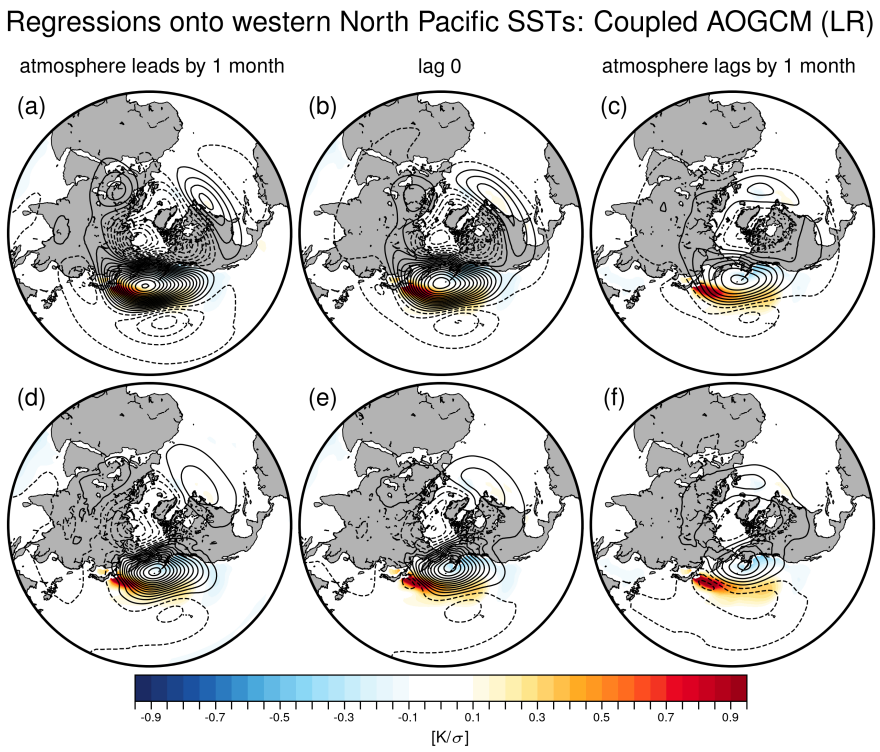

Figure 2.16: Z_{500} (top) and Z_{1000} (bottom) responses to the KOE SST anomalies at different lag based on the high resolution (LR) version of the Coupled AOGCM preindustrial control simulation.

K-SST index timeseries. Figure 2.17 shows the evolution of the SST anomalies associated with 1 standard deviation of the K-SST index in the observation and the coupled AOGCMs, calculated as the spatial average of the regression coefficients over the KOE region. The regression at lag 0 denotes the DJF SST anomalies regressed on to the DJF K-SST index time series. The SST anomalies over the KOE region associated with the K-SST index in the coupled model are larger ($\sim$50%) in amplitudes and more persistent than their observational counterpart.

The larger SST anomalies in Coupled AOGCM can be attributed to the excessive SST response to the meridonal movement of the oceanic jet in the KOE region [Thompson and Kwon (2010)], and it is consistent with the findings of Small et al. (2019) that the monthly anomalies of SST tendency near the WBC is overdominated by the atmospheric forcing in this standard resolution version of CESM.

To elucidate the model biases in the persistence of large-scale atmospheric circulation anomalies over the North Pacific, we defined the North Pacific SLP (NP) index as an average of

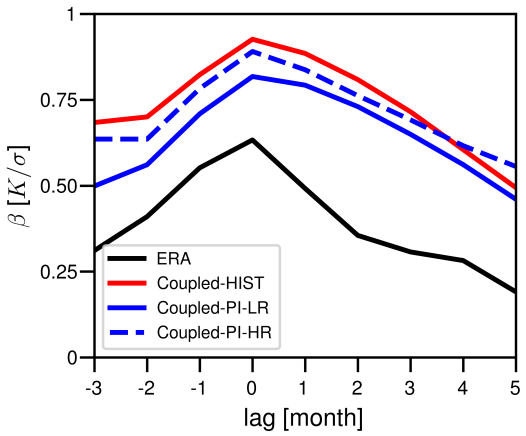

Figure 2.17: The evolution of the SST anomalies associated with 1 standard deviation of the K-SST index in the observation and the coupled AOGCMs, calculated as the spatial average of the regression coefficients over the KOE region. The regression at lag 0 denotes the DJF SST anomalies regressed on to the DJF K-SST index time series.

SLP anomalies over the domain 150°E-130°W and 35-70°N [as indicated by the red box in Figure 2.18; the results were not sensitive to the latitude (longitude) range $\pm$10 (20)°]. Since the difference among the various configurations of Coupled AOGCM was smaller than their biases from the observation (Figure 2.17), we focused on comparison of the results based on the observations and preindustrial control simulation (run on same horizontal resolution as historical simulation) to exclude influence of the external forcing.

Figure 2.19 shows the evolution of atmospheric circulation anomalies associated with the NDJ NP index timeseries. The regression coefficients are spatially averaged over the NP domain defined above. Here, the regression at lag 0 denotes the NDJ SLP anomalies regressed on to the NDJ NP index time series. The simulated SLP variability in Coupled AOGCM captures the general features of the observed SLP variability quite well, except the amplitude of the SLP anomalies at lag +1 is much stronger in the Coupled AOGCM (10 m) than in the observations (4 m). The e-folding time scale of NP index (for all months) was also slightly longer in the Coupled AOGCM PI run (0.76 month; r$\sim$0.27) than in the observation (0.56 month; r$\sim$0.17).

Global maps of the SST anomalies associated with the DJF KSST index time series are shown in Figure 2.2, to investigate the SST variability correlated with the KSST index outside the North

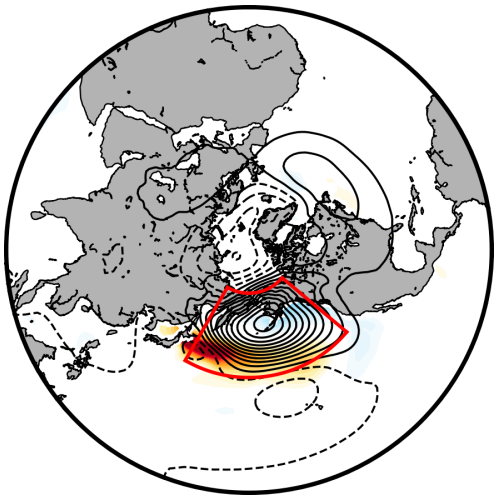

Figure 2.18: January (left), February (middle), and March (right) Z1000 responses to the KOE SST anomalies at lag -1 month, respectively. Results are shown for observations (top), the coupled AOGCM output (middle), and the KOGA output (bottom).

Pacific region. The coupled AOGCM reveals a PDO-like global pattern of SST anomalies with more correlated signals over the tropics (second row). Johnson et al. (2020) demonstrated the cooling in the equatorial Pacific associated with the PDO weakened the Aleutian low (i.e., positive SLP anomalies in the North Pacific) using partial ocean data assimilation experiments conducted with CESM. Thus, the correlated tropical SST anomalies may contribute to the persistence bias of the atmospheric forcing pattern in the Coupled AOGCM.

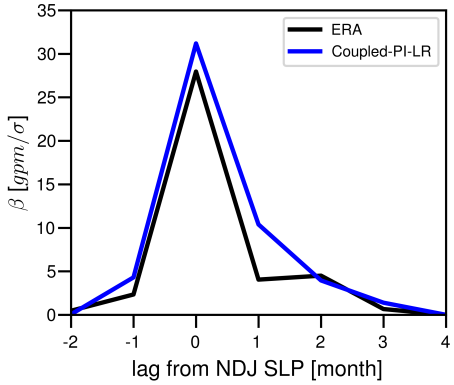

Figure 2.19: The evolution of atmospheric circulation anomalies associated with the NDJ NP index time-series. The regression coefficients are spatially averaged over the NP domain defined above. Here, the regression at lag 0 denotes the NDJ SLP anomalies regressed on to the NDJ NP index time series.

To summarize, the timescales of SST anomalies over the KOE region, atmospheric response and forcing pattern were longer in the Coupled AOGCM than in the observations (Figure 2.11):

1) The SST anomalies over the KOE region associated with the K-SST index in the coupled model are larger ($\sim$50%) in amplitudes and more persistent than their observational counterpart. The larger SST anomalies over the KOE region in Coupled AOGCM can be attributed to the excessive SST response to the meridonal movement of the oceanic jet in the KOE region [Thompson and Kwon (2010)], as well as the overestimated contribution of the atmospheric forcing on the SST variability there [Small et al. (2019); Small et al. (2020)].

2) The potential model biases in the representation of the SST variability over the KOE region may also contribute to the persistence of the atmospheric response up to lag +3 months in the Coupled AOGCM results.

3) The e-folding time scale of SLP variability in the North Pacific was slightly longer in the Coupled AOGCM PI simulation (0.76 month) than in the observation (0.56 month). The simulated SST anomalies associated with the K-SST index show a PDO-like pattern with negatively correlated temperature anomalies in the Equatorial Pacific, while the observational counterpart does not reveal substantial negative correlations over the Tropics (Figure 2.2). It has been demonstrated that the cooling in the equatorial Pacific associated with negative polarity of the PDO (i.e., warming of the KOE SSTs) can lead to the weakening of the Aleutian low (i.e., positive SLP anomalies in the North Pacific; Johnson et al. (2020)). Thus, stronger teleconnection from the correlated tropical SST anomalies may also contribute to the persistence bias of the atmospheric forcing pattern in the Coupled AOGCM.

Finally, seasonal dependencies of the atmospheric responses were also assessed. Figure 2.20 shows the circulation response at +1 month lag in each month (December, January and February). The response pattern with the low SLP anomalies that span over much of the North Pacific was largely unchanged in different calendar months, but the amplitudes of the response were generally weaker in March. The response pattern in the observation exhibits notable differences in March

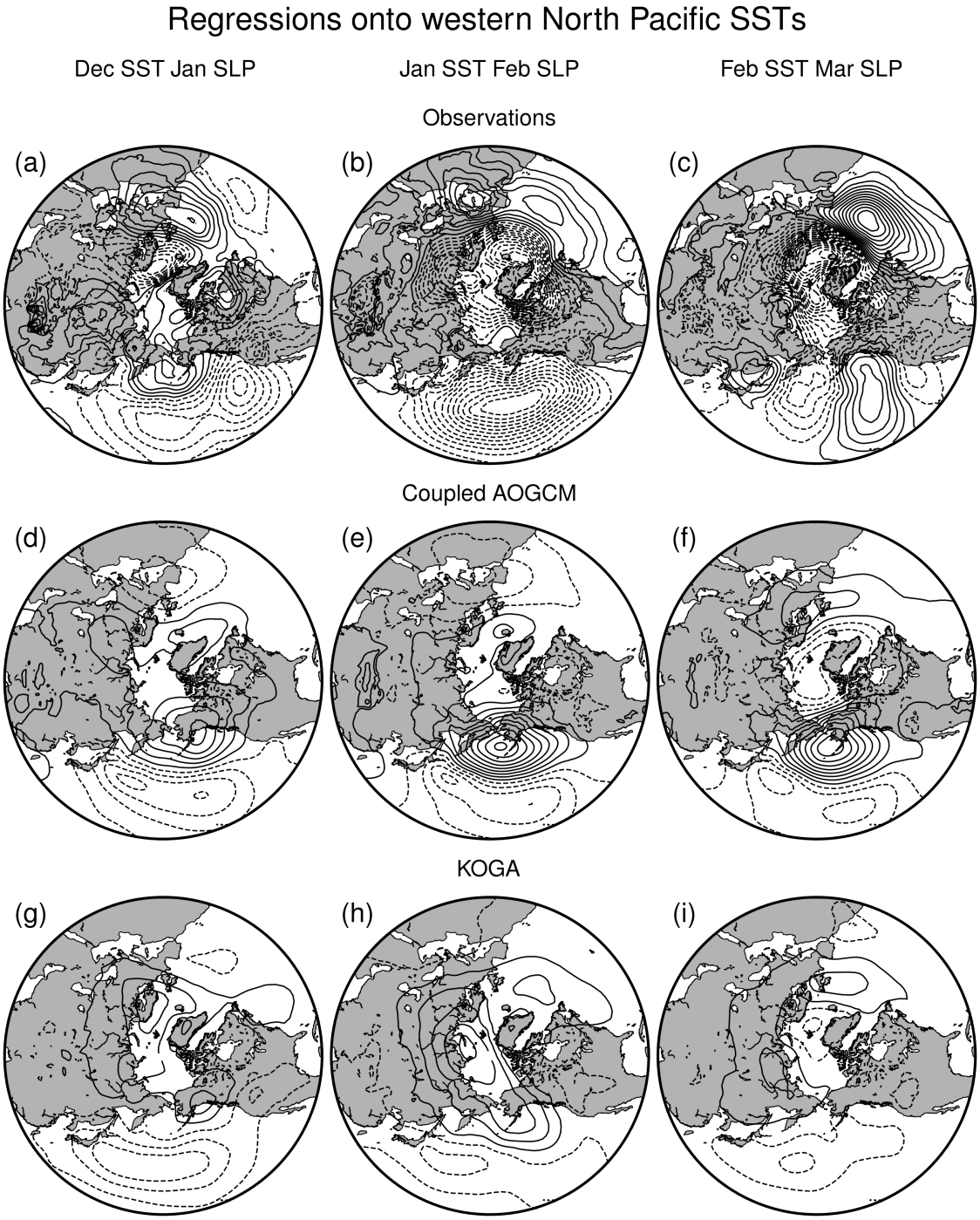

Figure 2.20: January (left), February (middle), and March (right) Z1000 responses to the KOE SST anomalies at lag -1 month, respectively. Results are shown for observations (top), the coupled AOGCM output (middle), and the KOGA output (bottom).

characterized by a wave train response over the North Pacific rather than the basin-wide low pressure anomalies shown in other months.

2.4 Discussion and conclusions

Extratropical atmosphere-ocean interactions potentially play a crucial role in climate variability. But key aspects of such interactions remain poorly understood. In part, this is because the linear response to midlatitude SST anomalies is expected to be small relative to the noise inherent in the midlatitude circulation [Hoskins and Karoly (1981)] and the total response is likely to include difficult to predict nonlinear changes in atmospheric eddies [Kushnir et al. (2002)].

In a recent study (WT18) we argued that the lead/lag relationships between the extratropical circulation and the SST field uniquely identify two structures associated with SST variability in the western North Pacific: 1) A pattern that leads SST variability and is consistent with forcing of the SST field by the atmospheric circulation; and 2) A pattern that lags SST variability and is consistent with the linear atmospheric response to extratropical SST anomalies [Hoskins and Karoly (1981)]. Lead/lag regressions alone do not prove causality. But the close correspondence between the lagged response and that expected from linear theory strongly suggests that it reflects the atmospheric response to SST anomalies. The results in WT18 build on a growing body of evidence that SST anomalies in the western boundary current regions can have a demonstrable effect on the tropospheric circulation (see discussion and references in Section 2.2).

Here we tested 1) the reproducibility of the observed lead/lag relationships from WT18 in output from a fully coupled AOGCM and 2) the reproducibility of the observed lagged circulation anomalies in a prescribed SST AMIP-style simulation. The key findings are the following:

1) The observed characteristics of atmosphere-ocean coupling in the North Pacific are well captured by the coupled AOGCM. Periods of anomalously high SSTs in the western North Pacific are preceded by circulation and heat flux anomalies that are consistent with atmospheric forcing of the SST field, and followed by circulation and heat flux anomalies that are consistent with the atmospheric response to the SST field.

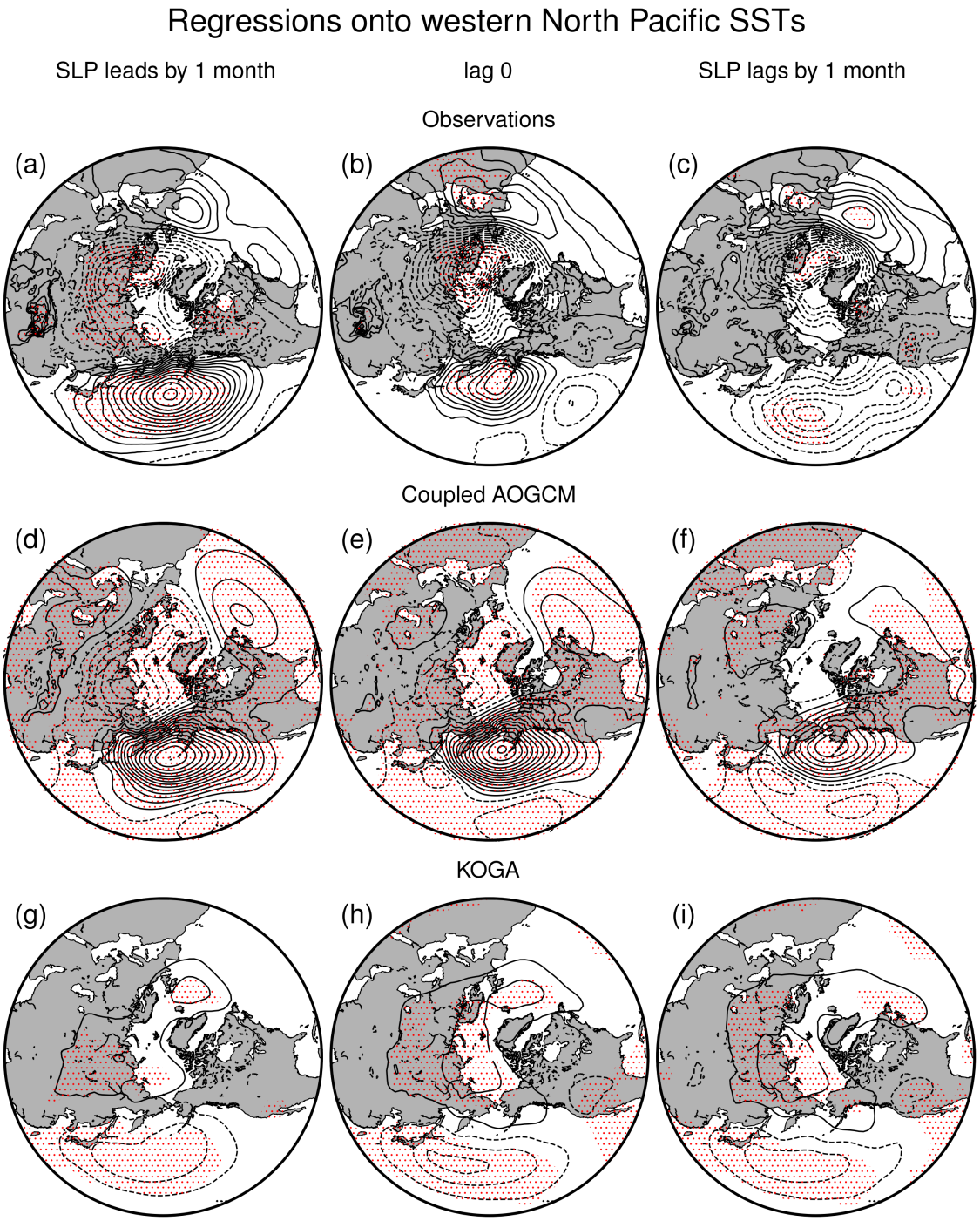

Figure 2.21: Z_{1000} regression coefficients reproduced from the top rows in Figure 2.5, Figure 2.8, and Figure 2.9. Stippling indicates regions where the significance of the attendant correlation coefficients are significant at the 95% level. See text for details.

2) The low-level component of the "response" pattern inferred from lag regressions in observations and the coupled AOGCM is recovered in numerical experiments forced with the time history of western North Pacific SST anomalies (the KOGA experiment).

3) The low-level component of the response pattern is highly robust in observations, the coupled AOGCM, and in the prescribed SST experiment (the KOGA experiment). In the latter case, the response pattern emerges not only in the ensemble mean but in most individual ensemble members.

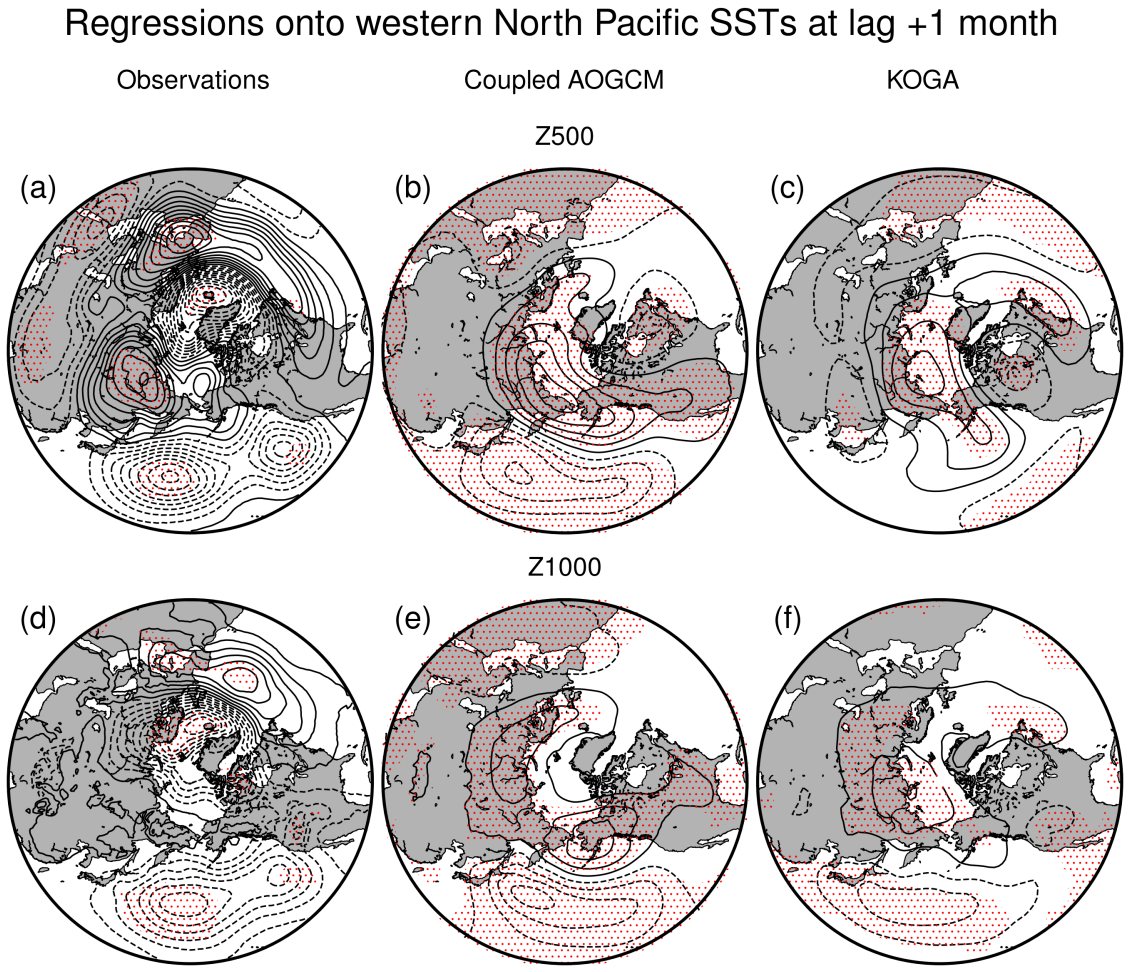

Figure 2.22: Z_{1000} regression coefficients reproduced from the top rows in Figure 2.5, Figure 2.8, and Figure 2.9. Stippling indicates regions where the significance of the attendant correlation coefficients are significant at the 95% level. See text for details.

One notable difference between results derived from the observations and coupled AOGCM relative to those derived from the KOGA simulation is the vertical structure of the response. The inferred responses from the observations and the coupled AOGCM have a deep equivalent barotropic component, whereas the response in the KOGA simulation is largest in the lower troposphere. We have speculated that the differences in the upper-level responses may derive from a range of factors, including differences in the horizontal resolution of the simulations, the amplitude of day-to-day variability in the SST field, and the representation of coupling between the atmosphere and SST field. These factors will be explored in a future study.

The *near-surface response* to KOE SST anomalies identified here is consistent with the linear response to SST anomalies predicted by linear theory [Hoskins and Karoly (1981)] and that found in numerous previous numerical studies [e.g., Kwon et al. (2011); Smirnov et al. (2015); see also the discussion in Kushnir et al. (2002)]. The inconsistency in the *upper-level response* found here is reminiscent of the inconsistency of the upper-level response found in previous studies. For example, many early studies found an equivalent barotropic response to midlatitude SST anomalies [e.g., see Table 1 in Kushnir et al. (2002)]. But the structure of the upper level response has proven sensitive to various aspects of the simulation. The upper-level responses explored in Peng et al. (1997), Peng and Whitaker (1999), and Peng and Robinson (2001) are dependent on the model climatology and patterns of internal variability. The upper-level response in Kwon et al. (2011) appears to be influenced by tropical-extratropical coupling. The upper-level response in Smirnov et al. (2015) varies depending on the model resolution. And the upper level response in Ma et al. (2015) and Ma et al. (2017) is strongly dependent on mesoscale features in the SST field.

Previous studies have suggested that the extratropical atmospheric response to midlatitude SST anomalies is a function of the seasonally-varying background flow [e.g., Peng and Whitaker (1999); Taguchi et al. (2012)]. The *simulated* pattern of low-level SLP anomalies found here does not vary notably in results stratified by calendar month (Figure 2.13). However, the *observed* lag-one regressions exhibit a more wavelike structure in data restricted to March (Figure 2.13). It is unclear whether the differences between results for March and those for other months are due

to variations in the climatological flow or sampling variability. Previous studies have also made clear the caveats associated with forcing an atmospheric GCM with the time history of prescribed SSTs [e.g., Bretherton and Battisti (2000)]. It is not clear how those caveats would influence the lead/lag relationships that are the focus here. Importantly, the amplitude of the ensemble-mean lagged response is reproducible in individual ensemble members (Figure 2.10).

Together, the results shown here suggest that the pattern identified in lead/lag regressions between the atmospheric circulation and the western North Pacific SST field reflects the atmospheric response to SST anomalies in the broad Kuroshio/Oyahshio extension region.

Chapter 3

Radiation-Climate Interactions

The purpose of this study is to quantify the role of 1) moist lapse rate and 2) surface temperature variability as constraints on the amplitude and structure of temperature variability in the tropical atmosphere. The authors analyze three sets of simulations run on the hierarchies of climate models: 1) a simulation run on a single-column radiative transfer model with a simple convective adjustment (Konrad), 2) a simulation run on global General Circulation Model (GCM) forced with prescribed Sea Surface Temperature (SST) in the Radiative-Convective-Equilibrium (RCE) setting, and 3) a simulation run on a coupled Earth System Models. The results of the RCE simulations, run on the single column radiative transfer model and the global GCM model, indicate that the tropical temperature variability exhibits a distinct maximum in the upper troposphere and that temperature variability is expected to increase under global warming. These characteristics of the simulated tropical temperature variability are consistent with predicted changes in the moist adiabatic thermal structure of the tropical atmosphere due to increases in mean surface temperature. In the fully coupled ESM simulations, atmospheric temperature variability is strongly influenced not only by change in mean surface temperature but also by changes in surface temperature variability. The ESM simulations exhibit large inter-model spreads in future projections of surface temperature variability, as well as in future changes in atmospheric temperature variability. Nevertheless, the estimation of atmospheric temperature variability based on the moist-lapse rate, with given information of surface temperature variability, reproduced qualitatively similar features of the simulated atmospheric temperature variability. The results highlight the role of the moist lapse rate feedback in combination with surface temperature variability as a potential constraint for climate variability in the tropical atmosphere.

3.1 Introduction

The tropical atmosphere is an engine of the global climate system modulating the global atmospheric circulation as well as the energy and moisture budget of Earth. The changes in tropical temperature can have substantial influences on regional weather and global climate, and affect various processes ranging from tropical cyclone, convection, to El Niño-southern oscillation (ENSO), Hadley cell, Brewer-Dobson circulation, and tropical-extratropical teleconnection (Brewer (1949); Philander (1983); Barnston and Livezey (1987); Trenberth et al. (1988); Emanuel (2005); Wang et al. (2000)). The amplitude and pattern of the tropical warming can also affect climate sensitivity and climate change (Andrews et al. (2018); Stevens et al. (2016); Zhou et al. (2016); Zhou et al. (2017)). Thus, understanding the nature of tropical atmospheric temperature is crucial to better understand and predict the global climate variability and change.

The fundamental physical constraints setting the equilibrium temperature profile of the tropical atmosphere are well understood. In the tropics, horizontal temperature advection is very small (Sobel and Bretherton (2000); Sobel et al. (2001); Charney (1963)), and thus the atmospheric temperature is strongly constrained by the balance between vertical advection of potential temperature and condensational heating in the convective region (i.e., Radiative-Convective Equilibrium, RCE; Manabe and Strickler (1964); Manabe and Wetherald (1967)). In a state of RCE, the atmospheric temperature in saturated regions can be expressed by a simple equation representing the temperature change associated with vertical motion conserving the moist static energy, the saturated isentropic (adiabatic) lapse rate, Γ_m (Bohren and Albrecht (1998); Yau and Rogers (1996)):

$$\Gamma_m = \Gamma_d \frac{1 + \frac{L_v q_s(T,P)}{R_d T}}{1 + \frac{L_v^2 q_s(T,P)}{C_p R_v T^2}} \tag{3.1}$$

with dry isentropic lapse rate Γ_d, specific heat capacity at constant pressure C_p, latent heat of vaporization L_v, saturation mixing ratio $q_s(T, P)$, gas constants for the dry air R_d and water vapor R_v, and temperature T. The saturated isentropic lapse rate represents the equilibrated profile of tropospheric temperature after energy-conserving convective adjustment (which results in cooling

of the surface and warming of the troposphere). That is the temperature profile in a state of radiative-convective equilibrium, adjusted from a state of radiative equilibrium, after redistribution of energy taken from the surface throughout the troposphere in the form of latent heat release via convective processes.

The physical constraints for the *long-term changes* in the tropical temperature profile under global warming are also well understood. The temperature profile of the tropical atmosphere becomes less steep in response to warming, because saturated air parcels at lower levels can hold more moisture than air parcels at upper levels following the Clausius-Clapeyron relationship, and thus the ascending air parcels can release more latent heat in the upper troposphere [Manabe and Stouffer (1980); Hansen et al. (1984); Soden et al. (2008)]. This leads to more warming of the upper troposphere than the lower troposphere.

The physical constraints governing the *variability* of the tropical atmospheric temperature are more complicated. The tropical temperature variability is shaped by a complex interplay of different physical processes, including the internal atmospheric variability associated with dynamical and thermodynamical processes intrinsic to the atmosphere or to the coupled ocean-atmosphere system [Madden (1976); Frankignoul and Hasselmann (1977); Feldstein (2000); Deser et al. (2003), Deser et al. (2012)], direct effect of CO2 [Miyawaki et al. (2020)] and cloud radiative effects [Slingo and Slingo (1988); Randall et al. (1989); Sherwood et al. (1994); Lee et al. (2001); Raymond (2001); Bony and Emanuel (2005); Fermepin and Bony (2014); Li et al. (2015)), overshooting convection [Sherwood and Dessler (2000); Kuang and Bretherton (2004); Dacie et al. (2019)] the Brewer-Dobson circulation [Andrews et al. (1987), textbook], water vapor feedback [Pierrehumbert (1995); Held and Soden (2000); Minschwaner and Dessler (2004)], anvil temperature [Hartmann and Larson (2002); Kuang and Hartmann (2007); Zelinka and Hartmann (2010)], and entrainment [Keil et al. (2021); Bao et al. (2021); Miyawaki et al. (2020)]. Thus, the relative importance of the moist lapse rate for *internal variability* of the tropical temperature remains uncertain. In other words, the extent to which the transient temperature variability in the tropics can be explained by the changes in isentropic lapse rate is also uncertain.

This study uses simulations run on the hierarchies of climate models to explore the role of 1) the saturated lapse rate and 2) surface temperature variability on the tropical atmospheric temperature variability as well as its change in a warming climate. First, we explore the simulations based on a single-column radiative transfer model with a simple convective adjustment (Konrad). We do this in order to understand the temperature variability associated with the moist lapse rate in a more controlled setting. We then repeat the analyses in a global context using the simulations run on the Community Atmosphere Model version 5 (CAM5) in the global RCE configuration. The CAM5 simulations are forced by a globally uniform fixed Sea Surface Temperature (SST). We also repeat the analysis using the outputs from simulations run on fully coupled Earth System Models to investigate the role of surface temperature variability originated from oceanic internal variability, on the atmospheric internal variability. A finding of the current study is that the moist lapse rate can explain the characteristics of the tropical-mean temperature variability as well as its changes under global warming.

3.2 Models

3.2.1 One-dimensional RCE model

We use a single-column model, Konrad [Kluft et al. (2019)], run on the RCE configuration [Popke et al. (2013); Kluft et al. (2019)] to simulate the tropical atmosphere in a more controlled setting. In Konrad, the Rapid Radiative Transfer Model for General circulation models [RRTMG; Mlawer et al. (1997)] is used to calculate radiative heating at each atmospheric layer. Then, the hard adjustment representing convective adjustment is applied to the atmospheric temperature profile below the convective top. The temperature profile is thus in a state of radiative-convective equilibrium following the isentropic lapse rate. All simulations are performed without actual clouds to exclude the influence of cloud-radiative effects. Relative humidity values are fixed at 80% with a vertically uniform profile, and fixed surface temperature and surface albedo (0.3) are used for the surface boundary condition. We followed the configurations of Konrad used in Kluft et al. (2019) and more details of the simulations are provided in their paper.

3.2.2 Global General Circulation Model (GCM) in the RCE

We analyze the global RCE simulations run on the Community Atmosphere Model version 5 [CAM5; Neale et al. (2010)], following the RCE setup widely used in previous studies [Popke et al. (2013); Reed et al. (2015)]. The RCE configuration represents the simplified basic state of the Earth's tropical atmosphere. The model consists of an ocean-covered Earth that has a globally uniform fixed SST, and diurnally varying but spatially uniform insolation. The planet's rotational rate is set to zero to remove the rotational effects.

The atmospheric temperature changes, in response to a fixed amount of surface temperature changes are analyzed in two different mean states, each prescribed with global SST of 290 K and 300 K. The model is first integrated over 36 months with the initial SST to reach the steady state. Then global 3K cooling is applied in the first month of each year for three consecutive years. After another year with the same SST, global 3 K warming is applied for three consecutive years. For example, the sequence of SST used in each year in the simulation with initial SST value of 290 K, is 290, 290, 290, 287, 284, 281, 281, 284, 287, and 300 K.

3.2.3 Coupled Earth System Models (ESM)

We analyse the existing output from the Large Ensemble experiments run on four different ESMs: the Community Earth System Model version 1 [CESM; Hurrell et al. (2013), Kay et al. (2015)], the Commonwealth Scientific and Industrial Research Organisation Mk3.6 [CSIRO-Mk3-6-0; Jeffrey et al. (2013)], the Canadian earth system model [CanESM2; Kirchmeier-Young et al. (2017)], and the Geophysical Fluid Dynamics Laboratory comprehensive Earth System Model ESM2M [GFDL-ESM2M; Rodgers et al. (2015)].

All four LENS simulations use the ESMs which consist of coupled atmosphere, ocean, land, and sea-ice models. The LENS experiments are integrated with CMIP5 historical forcing from 1920 to 2005 and representative concentration pathway 8.5 (RCP8.5) forcing over the period 2006-2100. We analyzed the output over the period 1920-2080 for CESM1, and 1950-2100 for other three ESMs. The LENSs consist of different numbers of runs (40 simulations on the

CESM1; 30 simulations on the CSIRO-Mk3-6-0; 50 simulations on the CanESM2; and 30 simulations on the ESM2M), generated with round-off level differences in the initial air temperature field. The LENS output is publicly available via the Multi-Model Large Ensemble Archive [MMLEA; Deser et al. (2020)] at the National Center for Atmospheric Research (https://doi.org/10.1038/s41558-020-0731-2), and archived on resources sponsored by the US CLIVAR Working Group on Large Ensembles and NSF/CISL/Yellowstone.

3.3 Hypothesis

Internal atmospheric variability arises from complex interactions among different physical and dynamical processes [Deser et al. (2012)]. Thus, understanding the characteristics of the internal atmospheric variability usually requires precise interpretations of the complicated aspects of the coupled interactions in the climate system. In the present study, we try to quantify the role of two physical processes on the internal temperature variability of the tropical atmosphere: 1) saturated isentropic lapse rate, which is a fundamental physical constraint modulating the atmospheric temperature profiles in a Radiative-Convective Equilibrium [Bohren and Albrecht (1998); Yau and Rogers (1996)], and 2) surface temperature variability, which contributes to atmospheric variability long-term, beyond a few weeks via dynamic and thermodynamic interactions in the coupled ocean-atmosphere system [Deser et al. (2012)].

We estimate the radiative-equilibrium response of the tropical atmosphere to surface temperature anomalies using the 1D-RCE model, Konrad. To reduce complexity of the problem, we make a few assumptions. Firstly, we assume only a one-way interaction is allowed between the atmosphere and ocean, as in "AMIP type" simulations for the Atmospheric Model Intercomparison Project. That is, the influence of atmospheric temperature variability on the surface temperature variability is assumed to be limited, and a fixed surface temperature (i.e., infinite heat capacity of surface) is used as the lower boundary condition instead of slab surface (i.e., finite heat capacity of surface). This assumption is valid since 1) we are interested in the atmospheric variability in response to the given surface temperature forcing, and 2) the heat

capacity of the atmosphere is much smaller than the heat capacity of the ocean mixed layer, thus any feedback on the surface temperature can be neglected. We are focusing on a large spatial scale that covers most of the tropics (i.e., tropical-mean) and a monthly timescale. Horizontal energy transport is negligible in such a spatiotemporal scale, and the timescale of interest is much longer than the convective timescale. With these assumptions, use of 1D-RCE to estimate the atmospheric temperature in response to variations in the surface temperature is justified.

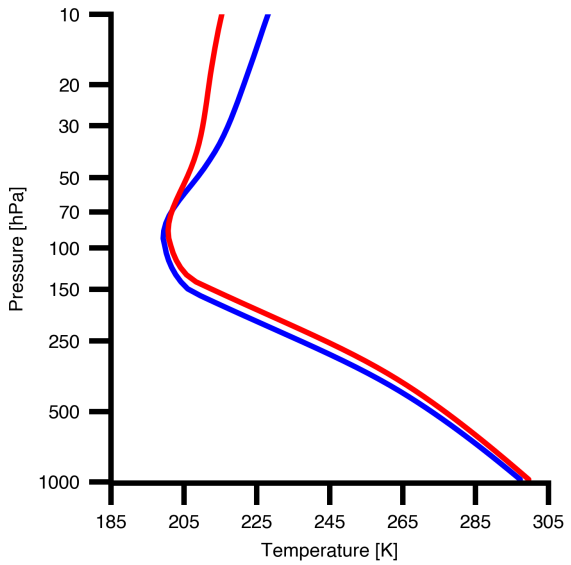

Figure 3.1: Mean temperature in tropical atmosphere in the Konrad simulations. (blue) A control simulation run with the present-day climate forcing and (red) a future climate simulation representing a warmer climate.

Figure 3.1 shows temperature profiles in the RCE simulated by the Konrad with different climate forcings: 1) a control simulation run with the present-day climate forcing, such as a fixed surface temperature of 298 K and CO2 concentration 342 ppm, and 2) a future climate simulation representing a warmer climate with quadrupling CO2 and 2.3 K warming of the surface temperature. The amount of tropical warming is estimated from a difference between the time-mean value of the tropical surface temperature from the CESM-LENS output over the period of 1981-2010 and the period of 2051-2080. Konrad reproduces observed characteristics of the vertical temperature profile of the tropical atmosphere fairly well [Kluft et al. (2019)]. For the

future climate projection in 2051-2080, warming of the troposphere juxtaposed with cooling of the stratosphere accompanied by a rise in the height of the tropopause, is shown. This is consistent with well-known features of changes in vertical structure of atmospheric temperature in response to increased CO2 forcing [Manabe and Wetherald (1967); Held et al. (1993); Kushner et al. (2001); Santer et al. (2003)].

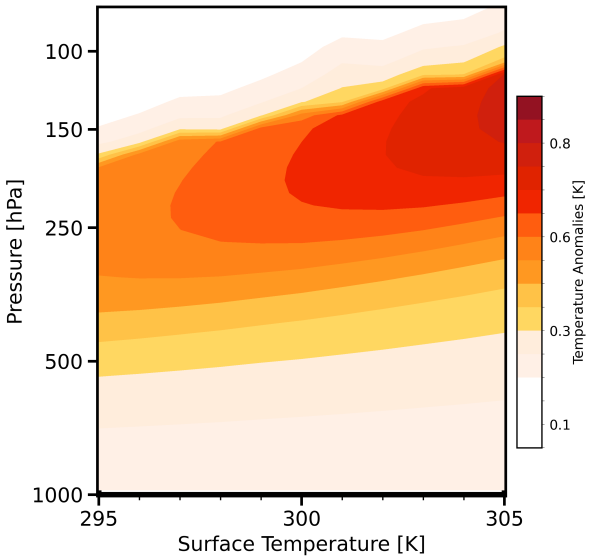

Figure 3.2: Changes in atmospheric temperatures in response to a given surface temperature perturbation for different mean surface temperatures ranging from 295 to 305 K at a 1 K interval. Both positive and negative surface temperature perturbations are imposed with a fixed amplitude of 0.2 K. The response is normalized by multiplying by a factor of 5 for 1 K of surface temperature perturbation.

Here we estimate the changes in the atmospheric temperature profile in response to 1 K warming in the surface temperature ($\frac{\Delta T(z)}{\Delta T_{sfc}}$) with different mean surface temperature ranging from 295 K (blue) to 305 K (red) using Konrad (Figure 3.2). The profile of atmospheric temperature anomalies is calculated as follows:

1) we calculated the equilibrium profile of atmospheric temperature using Konrad with an array of mean surface temperatures ranging from 295 to 305 K at a 1 K interval.

2) we also calculated the atmospheric temperature responses for both positive and negative surface temperature perturbations with a fixed amplitude of 0.2 K with respect to the mean temperatures.

3) The changes in atmospheric temperature from both the warming and cooling cases are averaged after flipping the sign of the temperature anomalies from the case with negative surface temperature perturbation.

4) The atmospheric temperature anomalies are multiplied by 5 to represent the atmospheric temperature response to 1 K of surface temperature anomalies.

For simplicity, the CO_2 concentration is also assumed to remain constant (346 ppm). This assumption does not qualitatively affect the results, since 1) the influence of variations in the CO_2 concentration is limited to the temperature profile above the convective top where the convective adjustment is not applied, and 2) we are focusing on the changes in atmospheric temperatures with respect to changes in surface temperature, not with CO_2 concentration (i.e., the perturbation experiments and control simulation are forced with same CO_2 concentration).

The atmospheric temperature response derived from the Konrad model exhibits more pronounced anomalies in the upper troposphere, regardless of the mean surface temperature (Figure 3.2). The results also suggest that, even with the same amplitude of surface temperature forcing, amplitude of atmospheric temperature response increases as mean surface temperature increases. The peak in atmospheric temperature anomalies is $\sim$2.5 K and found at the $\sim$200 hPa level in the case of with mean surface temperature at 280 K (blue), while the peak value is increased to $\sim$4.0 K and found at the slightly higher level of $\sim$180 hPa in the case with mean surface temperature at 300 K (red).

The reason why the amplitudes of the atmospheric temperature anomalies are pronounced in the upper troposphere has been extensively studied in previous literatures [Manabe and Stouffer (1980); Hansen et al. (1984); Soden et al. (2008)]. That is: 1) In a warmer climate, saturated air parcels ascending from the lower-level can hold more moisture following the Clausius-Clapeyron relationship, and 2) this results in a release of more latent heat in the upper troposphere and more

warming of the upper troposphere than the lower troposphere. Furthermore, the results shown in Figure 3.2 prove that the amplitudes of upper tropospheric temperature anomalies will increase even more with increasing mean surface temperature following the changes in moist lapse rate. Thus, the results from a simple single-column model suggest that internal atmospheric variability is expected to increase in a warmer climate (up to $\sim$20% with 4 K increase in mean surface temperature) even while other climate forcings of atmospheric variability remain the same in the future.

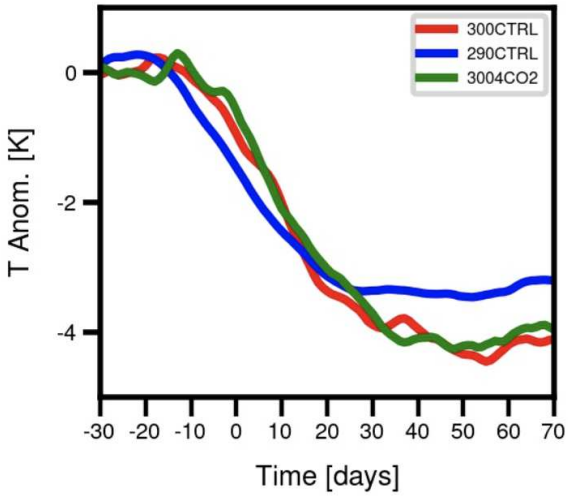

Figure 3.3: Changes in atmospheric temperature at 200 hPa level in response to 3 K of uniform surface cooling.

3.4 Interpretation of the global analyses

3.4.1 global RCE simulations

We repeat the analyses in a global context to explore whether this simple analogy based on the simple single-column model results also holds in a global atmosphere. Figure 3.3 reveals the time evolution of the global-mean temperature in response to 3 K of global surface cooling in the CAM5 global RCE simulation. A larger temperature response is shown in the case with a warmer initial surface temperature (300 K, red line) compared to the case with a colder initial surface

temperature (290 K, blue line), even with the same amount of surface cooling (Figure 3.3). A sensitivity of response to the different CO2 concentrations was tested in another experiment forced with four times CO2 and 300 K of surface temperature (green line). The results indicate that the atmospheric response, with respect to the surface temperature perturbations, is not sensitive to the CO_2 concentration in the global RCE simulations with convective parameterization.

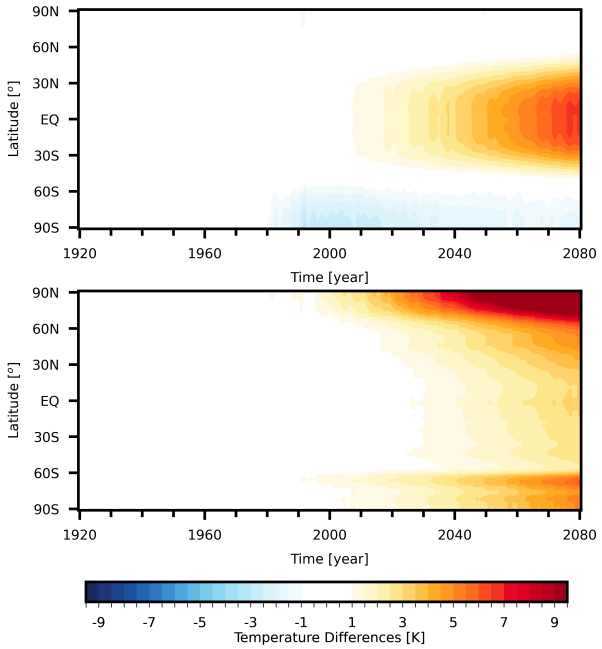

Figure 3.4: The zonal-mean temperature averaged over all ensembles is plotted as the function of time vs. latitude.

3.4.2 global ESM simulations

The internal atmospheric variability, especially with a timescale of longer than a few weeks, can be strongly influenced by oceanic variability through various coupled interactions between the atmosphere and ocean [Deser et al. (2012)]. Thus, we analyzed the simulations run on fully coupled ESM to assess the role of surface temperature variability on the atmospheric temperature variability.

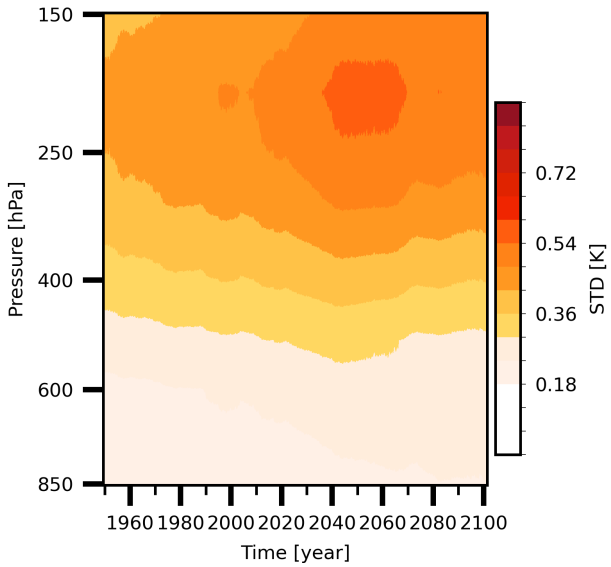

Figure 3.5: The standard deviation of tropical mean air temperatures plotted as a function of time and vertical level. The variance is calculated similarly to Figure 3.4, that is: the variance of tropical mean air temperature at each vertical level and each ensemble member is calculated in 30-year time window, starting from center-month of 1920 January and sliding the window month by month. A linear trend is removed in each window to reduce influence of any long-term trend within 30-year period on the temperature variance. Then, the variance is averaged over all ensemble members.

We first repeat the analyses using output from CESM-LENS simulations following the RCP8.5 scenario. Figure 3.4 shows the time evolution of zonal-mean atmospheric temperature at the 200 hPa (top) level and the surface temperature (bottom) in the CESM-LENS output. The zonal-mean atmospheric temperature shows a large increase in the tropical latitudes starting from the early 21st century. The tropical warming pattern is consistent with pronounced upper tropospheric warming following the moist lapse rate [Figure 3.4a; Manabe and Stouffer (1980); Hansen et al. (1984); Soden et al. (2008)]. The zonal-mean surface temperature also increases over the tropics, but larger warming is shown over the polar regions (Figure 3.4b). The surface warming over the polar latitudes is consistent with the well-known pattern of "polar amplification" due to positive temperature feedback from local sea ice losses in a warming climate [Screen and Simmonds (2010)].

In following section, we will explore the evolution of temperature variability over time based on the CESM output. To exclude the changes in mean temperature in response to external forcing,

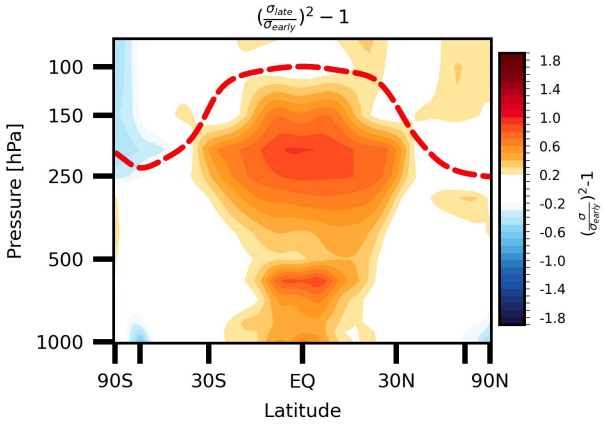

Figure 3.6: The zonal-mean temperature variance is plotted as a function of latitude and vertical (pressure) level.

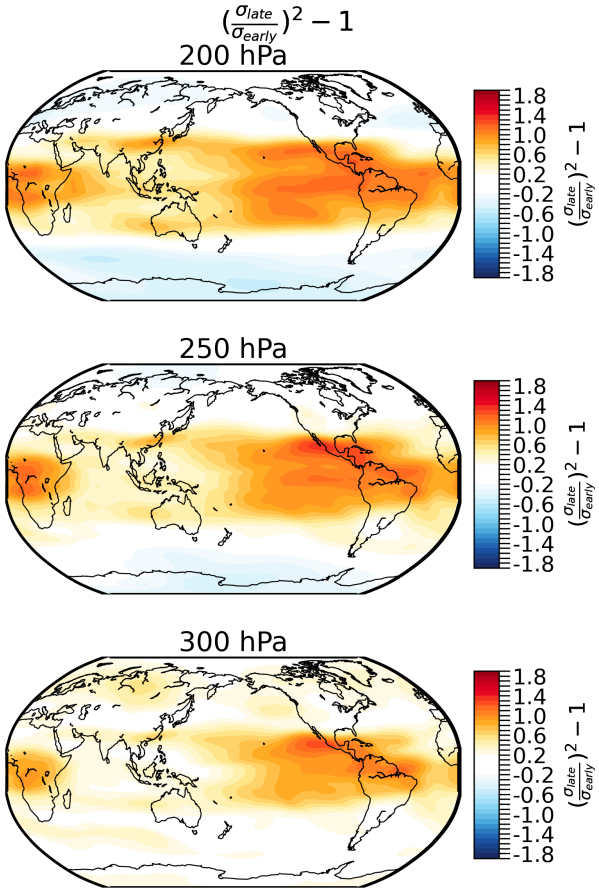

Figure 3.7: The temperature variance is plotted as a function of latitude and longitude at three different levels (top) 200, (middle) 250, and (bottom) 300 hPa level. The variance was calculated over time, and it was averaged over ensembles. The results are shown as fractional changes of variance during the 2050-2080 with respect to the variance during 1921-1950.

the ensemble mean of the temperature field is subtracted from each ensemble member before estimating the temperature variability. The profile of tropical temperature variability, derived from the global climate model, is shown in Figure 3.5, and it represents a qualitatively similar pattern compared to the one derived from the single-column model (Konrad, Figure 3.2). Both models show pronounced temperature variability in the upper troposphere 200 hPa level. Konrad output reveals an increase in temperature variance as surface temperature increases, and CESM output exhibits an increase in temperature variances over time accompanied by tropical surface warming due to greenhouse gas forcing. The peak amplitude of tropical temperature variability in the CESM is found around the 200 hPa level, and variance of temperature variability increases by $\sim$40% from 0.40 K in 1921-1950 (early period) to 0.55 K in 2051-2080 (late period) as the tropical mean surface temperature increases from 297.7 K to 300.2 K.

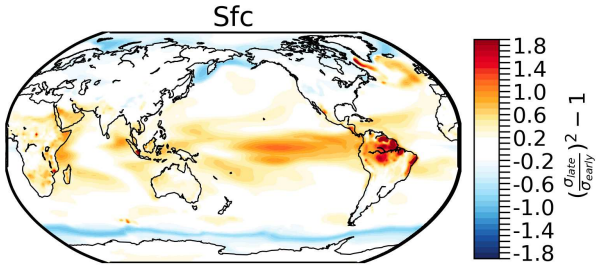

Figure 3.8: As in Figure7, but for the surface temperature variance

The global structure of the internal atmospheric temperature variability is further shown in Figure 3.6 and Figure 3.7. The vertical structure of variance in zonal-mean temperature is shown in Figure 3.6, and the global pattern of variance in air temperature at three different levels is shown in Figure 3.7. The results are shown as fractional changes in the variance during 2051-2080 with respect to the variance during 1921-1950. Again, temperature variance over the tropics increases markedly with height, and it reveals a distinct maximum in the middle to upper troposphere (from $\sim$400 hPa level to $\sim$150 hPa level; Figure 3.6). At three different levels, the global pattern of variance in atmospheric temperature reveals a similar pattern marked by large

increases in variance over the eastern tropical Pacific, consistent with the ENSO region (Figure 3.7)

A potential connection between the changes in internal oceanic variability and the increase in the temperature variance aloft is investigated in Figure 3.8 and Figure 3.9. Figure 3.8 shows a global pattern of variance in surface temperature. Figure 3.9 reveals the time evolution of variances in (top) atmospheric temperature at the 200 hPa level and (bottom) the surface temperature. The results in Figure 3.9 are shown as fractional changes with respect to the variance during 1921-1950.

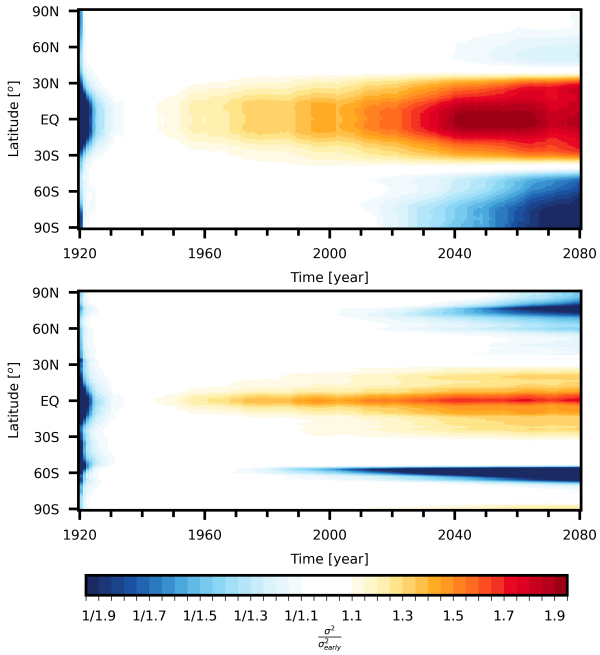

Figure 3.9: The temperature variance over all ensembles is plotted as the function of time and latitude. The time period is from 1920-2080, and the results are shown as fractional changes with respect to the variance during 1921-1950. The top panel represents the variance at 200 hPa, while the bottom panel represents the surface. The variance at each grid point and each ensemble member is calculated in 30-year time window, starting from center-month of 1920 January and sliding the window month by month. A linear trend is removed in each window to reduce influence of any long-term trend within 30-year period on the temperature variance. Then, the variance is averaged over all zonal grid points as well as ensemble members. A narrower window for calculating the variance is used in the period 1920-1935 and the period 2065-2080.

Both the atmospheric temperature at 200 hPa level and the surface temperature show increases in variability over time. The increase in surface temperature suggests either 1) other processes contribute to variance increases in surface temperature or 2) the variance increase due to the moist lapse rate initiates positive feedbacks with the surface temperature field. We note that the increase in variance over time is much larger in the 200 hPa atmospheric temperature than in the surface temperature field.

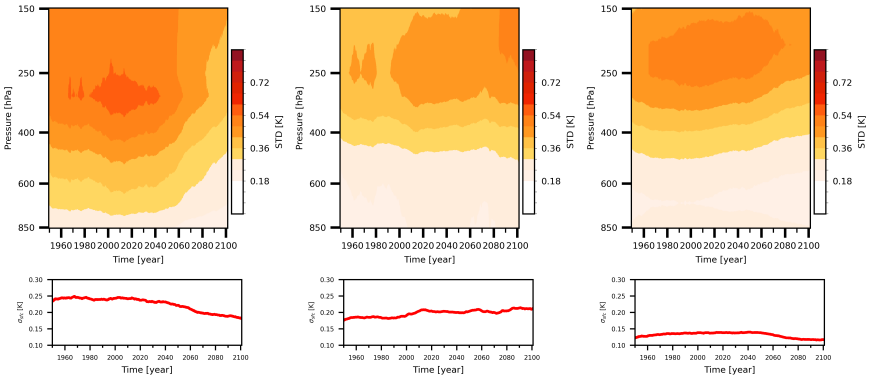

Figure 3.10: (Top) Figures show the standard deviation of tropical mean air temperatures plotted as a function of time and vertical level. The variance is calculated as: the variance of tropical mean air temperature at each vertical level and each ensemble member is calculated in 30-year time window, starting from center-month of 1920 January and sliding the window month by month. A linear trend is removed in each window to reduce influence of any long-term trend within 30-year period on the temperature variance. Then, the variance is averaged over all ensemble members. (Bottom) The line represents the time series of tropical mean surface temperature standard deviation calculated in a 30-year sliding window.

The increase in atmospheric temperature variability could arise from both 1) changes in the moist lapse rate due to increases in mean surface temperature as hypothesized from the RCE experiment with fixed SST setting, or 2) increases in surface temperature variability driven by other processes. In either case, the changes in variance of the tropical atmospheric temperature in the coupled climate system can also be explained by changes in the moist adiabatic thermal structure in response to 1) changes in mean surface temperature or 2) changes in surface temperature variability. Both will lead to greater changes in atmospheric variability around 200 hPa level.

We explore changes in temperature variance in large ensemble simulations run on three ESMs: the CSIRO-Mk3-6-0, CanESM2 and GFDL-ESM2M. Figure 3.10 shows the time evolution of tropical mean temperature variability as shown in Figure 5, but for the three other models. The top panels in Figure 3.10 reveal the atmospheric temperature variability at each level, and the bottom panels reveal the surface temperature variability. Multi-model large ensemble simulations exhibit large inter-model spreads in future projections of surface temperature variability, as well as in future changes in atmospheric temperature variability (Figure 3.10). The large discrepancies in future projections of surface temperature variability among different models render it difficult to estimate the changes in internal atmospheric temperature variability in future climate projections.

We thus repeat the analyses of tropical temperature variability, focusing on changes in temperature variability as a function of tropical mean surface temperature. Figure 3.11 shows tropical-mean 200 hPa atmospheric temperature regressed onto tropical-mean surface temperature based on (blue) the LENS outputs, and (black) the Konrad simulations. Figure 3.12 also shows the regression coefficients, as in Figure 3.11, but after multiplying them with standard deviations of tropical-mean surface temperature. The standard deviations of surface temperature are also shown as the green dots.

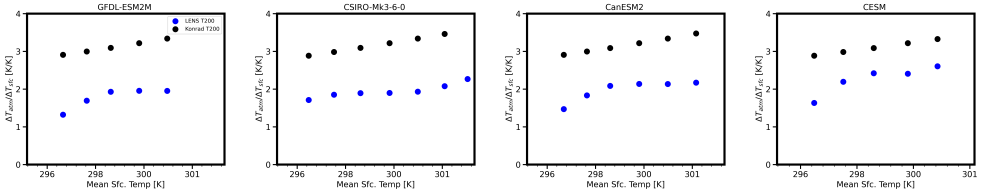

Figure 3.11:
Figure 11 shows a scatter plot of (abscissa) time-averaged tropical-mean surface temperatures versus (ordinate) the tropical-mean 200 hPa air temperatures regressed onto tropical-mean surface temperature based on (blue) LENS output and (black) Konrad output. Blue dots are calculated as follows: 1) To form the time series of temperature anomalies, the ensemble mean is removed from each ensemble member. 2) We sampled the air temperatures and surface temperatures based on 1 K interval in tropical-mean surface temperature over all period and ensembles. 3) The linear regression of 200 hPa air temperature anomalies onto surface temperature anomalies is calculated in each bin.

The atmospheric temperature anomaly per 1 K of surface temperature anomaly increases with mean surface temperature in output from multi-model ESM simulations (blue dots in Figure 3.11), which is qualitatively similar to the increase in amplitude of atmospheric response with increasing mean surface temperature estimated from the Konrad (black dots in Figure 3.11). Surface temperature variability in the ESMs reveals pronounced changes over time (CESM results shown in Figure 3.9 and results from other three ESMs shown in lower panels of Figure 3.10). To consider the amplitude of changes in surface temperature variability over time, the results in Figure 3.12 show that the atmospheric temperature anomaly per 1 σ of surface temperature anomaly follows the evolution of surface temperature variability in the ESMs. Figure 3.12 reveals that amplitude of atmospheric temperature response to surface temperature perturbations is also largely governed by changes in surface temperature variability.

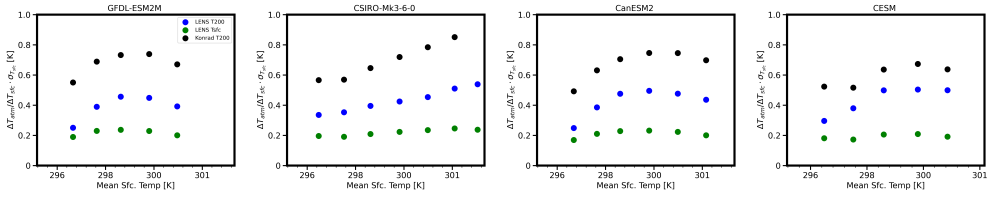

Figure 3.12:
Figure 12 shows a scatter plot of (abscissa) time-averaged tropical-mean surface temperatures versus (ordinate) the tropical-mean 200 hPa air temperatures regressed onto tropical-mean surface temperature based on (blue) LENS output and (black) Konrad output. The results are multiplied by (green) corresponding standard deviation of surface temperature anomalies.
Blue and green dots are calculated as follows: 1) To form the time series of temperature anomalies, the ensemble mean is removed from each ensemble member. 2) We sampled the air temperatures and surface temperatures based on 1 K interval in tropical-mean surface temperature over all period and ensembles. 3) The linear regression of 200 hPa air temperature anomalies onto surface temperature anomalies is calculated in each bin.

Together, the results suggest that: in the coupled simulations, the changes in atmospheric temperature variability could arise from either 1) changes in moist lapse rate due to increases in mean surface temperature as hypothesized from the RCE experiment with fixed SST setting (Figure 3.11), or 2) changes in surface temperature variability driven by other processes (Figure 3.12). In both cases, Konrad reproduces the qualitatively similar features of the results

from the ESM simulations. Thus, the changes in variance of the tropical atmospheric temperature in the coupled ESMs can also be explained by changes in moist adiabatic thermal structure in response to 1) increases in mean surface temperature or 2) changes in surface temperature variability.

The amplitude of atmospheric temperature anomalies, with respect to changes in surface temperature is smaller than the one derived from the Konrad (Figure 3.11 and Figure 3.12). This is expected since the fixed SST setting used in Konrad assumes infinite heat capacity of the ocean, and thus the surface can provide energy as much as it is needed for the atmosphere to reach another thermal equilibrium for the given surface perturbation. However, the heat capacity of the ocean in the coupled simulation is limited, and thus both the atmospheric and surface temperature anomalies will be transient. The surface temperature perturbations in the coupled simulations will not as persistent as the perturbations in the fixed SST setting because the heat anomalies are dissipated by energy transfer to the atmosphere or by other processes such as ocean dynamics or vertical diffusion. Thus, the surface temperature perturbation will not give enough time for the atmosphere to reach the equilibrium with respect to its initial amplitude, unlike in the fixed SST setting. There might also exist negative feedback, such as the anomalous downward longwave transfer from the atmosphere to the surface, due to cooling of the surface as the energy is taken out by the atmosphere, which may lead to less warming of the atmosphere.

3.5 Discussion

The importance of convective adjustment for shaping the climatological-mean temperature profile of the tropical atmosphere is well established [Manabe and Wetherald (1967); Figure 3.1], That is: 1) the mean profile of atmospheric temperature in the tropics approximately follows the moist adiabatic thermal structure, and 2) its change under global warming also follows changes in moist adiabatic lapse rate characterized by greater warming in the upper levels than in the lower levels.

We hypothesize that the pattern of internal temperature *variability* in the tropics is also governed by the same physical constraint, changes in the moist adiabatic thermal structure in response to the mean surface temperature variability. A warmer climate can hold a greater amount of atmospheric water vapor, which in turn leads to an increase in the amount of latent heat released into the atmosphere from moist convection. Thus, based on the hypothesis, internal variability of the tropical atmosphere is expected to increase in a warmer climate. The hypothesis is supported by the results from single column model RCE experiment (Figure 3.2).

We tested our hypothesis in a global context using simulations run on 1) atmopsheric GCM in RCE setting as well as 2) fully coupled ESMs. The results in Figure 3.3 support the hypothesis that increasing temperature variability in a warming climate also holds in the tropical atmosphere of the global GCM with a fixed SST setting. However, the patterns of tropical temperature variability derived from the coupled ESM simulations are more complicated. The tropical-mean atmospheric temperature variability in the coupled ESM output also reveals a pronounced maximum in the upper troposphere, but changes in atmospheric variability over time under the global warming scenario varied from model to model (Figure 3.5 and Figure 3.10). We attribute this disagreement in evolution of atmospheric temperature variability among models to large inter-model spreads in future projections of surface temperature variability. Nevertheless, the results from coupled simulations indicate the changes in atmospheric temperature variability could arise from:

1) changes in moist lapse rate due to increase in mean surface temperature. These are shown as atmospheric temperature anomalies with respect to unit amplitude (1 K) of surface temperature anomalies in Figure 3.11.

2) changes in surface temperature variability driven by other processes that are reflected aloft. These are shown as atmospheric temperature variability standardized by 1 standard deviation (1 σ) of surface temperature variability in Figure 3.12.

The qualitatively similar features of the results from the ESM simulations were reproduced by single column Konrad simulations (Figure 3.11 and Figure 3.12). Thus, the results suggest that

the changes in variance of the tropical atmospheric temperature in the coupled ESMs are also constrained by changes in moist adiabatic thermal structure in response to 1) increase in mean surface temperature or 2) changes in surface temperature variability.

Hence the results indicate that the moist lapse rate is a robust constraint for tropical climate variability, simulated by different model hierarchies. Variations in upper tropical tropospheric temperatures play a critical role in the global climate. Greater warming in the upper troposphere in response to surface warming leads to an increase in outgoing longwave radiation, which in turn plays a key role in determining the negative sign of the global lapse rate feedback [Feldl et al. (2020)]. These temperatures also determine the height of the tropopause as well as the static stability of the troposphere. Understanding these thermophysical constraints on upper tropical tropospheric temperature variability can help us better predict and understand the climate variability of the tropical atmosphere and its possible impacts on global climate.

Chapter 4

Chemistry-Climate Interactions[2]

The effects of coupled chemistry-climate interactions on the amplitude and structure of stratospheric temperature variability are quantified. To do so, two simulations run on the Whole Atmosphere Coupled Climate Model version 4 (WACCM) are examined: A "free running" simulation that includes fully coupled chemistry-climate interactions; and a "specified chemistry" version of the model forced with prescribed climatological-mean chemical composition. The results indicate that the inclusion of coupled chemistry-climate interactions increases the internal variability of temperature by a factor of two in the lower tropical stratosphere and – to a lesser extent – in the Southern Hemisphere polar stratosphere. The increased temperature variability in the lower tropical stratosphere is associated with dynamically driven ozone-temperature feedbacks which are only included in the coupled-chemistry simulation. The results highlight the fundamental role of two-way feedbacks between the atmospheric circulation and chemistry in driving climate variability in the lower stratosphere.

4.1 Introduction

The key role of stratospheric chemistry in setting the *climatological-mean* stratospheric circulation is well established. The absorption of shortwave radiation by ozone leads to increasing temperature with height and thus contributes to high values of static stability at stratospheric levels [Brasseur and Solomon (2005)]. Water vapor contributes to radiative cooling above the extratropical tropopause [Forster and Shine (2002)] which leads to the formation of a region of enhanced static stability in the lowermost stratosphere [the tropopause inversion layer; Birner (2006); Randel et al. (2007)]. The climatological-mean overturning circulation in the stratosphere

[2]The results outlined in Chapter 4 have been published in the *Journal of Climate*: Yook, S., D. W. Thompson, S. Solomon, and S.-Y. Kim, 2020: The key role of coupled chemistry–climate interactions in tropical stratospheric temperature variability. *Journal of Climate*, **33 (17)**, 7619–7629.

is mainly driven by the mixing of potential vorticity by atmospheric waves, but is also influenced by the radiative forcing due to trace gases such as ozone, water vapor and carbon dioxide [Holton and Wehrbein (1980)]. Consequently, precise knowledge of the chemical composition of the stratosphere is required for an accurate understanding of the stratospheric thermal structure and mean circulation.

The key role of stratospheric chemistry for *long-term changes* in the stratospheric circulation is also well established. The Antarctic ozone hole has resulted in a colder and stronger Southern Hemisphere (SH) stratospheric polar vortex [Randel and Wu (1999); Waugh et al. (1999)] and a poleward shift of the tropospheric westerly jet, which has significant impacts on SH surface climate [Thompson and Solomon (2002); Gillett and Thompson (2003)]. The effects of Northern Hemisphere (NH) polar ozone depletion on the circulation are in general much weaker, consistent with the relatively small ozone losses there [e.g., Calvo et al. (2015); Stone et al. (2019); Ivy et al. (2017)]. Changes in atmospheric carbon dioxide (CO_2) have led to a colder stratosphere [Ramaswamy et al. (2001); Shine et al. (2003)], and several modeling studies show that greenhouse gases and ozone depleting substances have also strengthened the stratospheric Brewer-Dobson circulation [Butchart and Scaife (2001); Garcia and Randel (2008); Polvani et al. (2019)).

The importance of stratospheric chemistry for *internal variability* in the stratospheric circulation remains more uncertain. For example, Smith et al. (2014) compared the mean and variability of the simulated climate in two preindustrial simulations run on the National Center for Atmospheric Research (NCAR) Whole Atmosphere Community Climate Model (WACCM) with varying configurations of chemical process: 1) a "free running" simulation that includes fully coupled chemistry-climate interactions; and 2) a "specified chemistry" simulation forced with prescribed, annually-repeating, climatological-mean chemical composition of ozone and other radiatively active gases (atomic and molecular oxygen (O and O_2), nitrogen oxide (NO) and carbon dioxide (CO_2)) in the middle atmosphere derived from the free-running experiment. Both models are coupled to active ocean, land, and sea-ice models. The main conclusion from their

work is that prescribing annually-repeating values of chemical composition leads to an effectively identical mean climate as that found in the coupled simulation. However, they did not explore in detail the role of coupled chemistry in driving the variability in climate about its seasonal-cycle throughout the global stratosphere. More recent works have explored the role of feedbacks between chemistry and dynamics for stratosphere–troposphere coupling [Haase and Matthes (2019)], the annual temperature cycle in the lower tropical stratosphere [Fueglistaler et al. (2011); Gilford and Solomon (2017); Ming et al. (2017)], and for temperature variability in the polar stratosphere [Rieder et al. (2019)]. But again, the importance of such feedbacks for temperature variability throughout the global stratosphere has not been quantified.

Here we revisit the "free running" and "specified chemistry" simulations produced with the NCAR WACCM to systematically explore the importance of coupled-chemistry interactions for internal climate variability throughout the global stratosphere. A key result of the current study is that the inclusion of coupled chemistry - and thus of variability in ozone about the seasonal cycle - leads to a roughly two-fold increase in temperature variability in the lower tropical stratosphere and – to a lesser extent – in the SH polar stratosphere, but relatively modest changes elsewhere. Section 4.2 provides a description of the climate models, the output used in the analyses, and the analyses methods. Section 4.3 explores the differences in temperature variance between simulations run with and without coupled chemistry and Section 4.4 probes the connections between stratospheric ozone, radiative heating, and temperature variance. Section 4.5 provides a discussion and summary of the results.

4.2 Model and Analysis Details

4.2.1 WACCM

We analyze existing 200 year long time-slice preindustrial experiments run with two different versions of the Whole Atmosphere Community Climate Model version 4: 1) an experiment run on a free-running, fully coupled-chemistry version of the model [FR-WACCM; Marsh et al.

(2013)], and 2) an experiment run on a version of the model with seasonally-varying specified chemistry [SC-WACCM; Smith et al. (2014)].

WACCM is the atmospheric component of the National Center for Atmospheric Research (NCAR) Community Earth System Model Version 1 (CESM). The chemistry module includes 59 species, 217 gas-phase chemical reactions, 17 heterogeneous reactions on three aerosols types, and heating from volcanic aerosols [Marsh et al. (2013)]. Both the FR-WACCM and SC-WACCM simulations are run with horizontal resolution of 1.9°×2.5°, 66 vertical levels, a model top at approximately 140 km, and identical interactive ocean, land, and sea-ice models.

The FR-WACCM simulation was run with 1850 preindustrial emissions, no volcanic forcings, and no Quasi-Biennial Oscillation (QBO). Chemical species such as O_x, NO_x, and HO_x were calculated by the chemistry model. The SC-WACCM simulation is essentially identical in all respects to the FR-WACCM simulation except that 1) the concentrations of ozone are prescribed everywhere and other radiatively active atmospheric constituents (O, O_2, NO and CO_2) are prescribed in the upper atmosphere (above 70 km) based on annually-repeating, long-term mean values derived from the FR-WACCM run, 2) the concentrations of water vapor and other radiatively active trace gases [e.g., nitrous oxide (N_2O) and methane (CH_4)] in the atmosphere are calculated using the relatively simple Garcia and Solomon two-dimensional model [Garcia and Solomon (1994)] rather than fully comprehensive chemistry, and 3) methane oxidation processes in the middle atmosphere are simplified as the conversion of each loss of CH_4 molecule into the production of two water vapor molecules. That is: The long-term, seasonally-varying chemical concentrations are identical in the FR-WACCM and SC-WACCM, but only FR-WACCM explicitly simulates the coupling between atmospheric dynamics and chemistry and includes variability in concentrations about the seasonal cycle. More details of the FR-WACCM and SC-WACCM simulations are provided in Marsh et al. (2013) and Smith et al. (2014), respectively.

4.2.2 Coupled Model Intercomparison Project (CMIP5 and CMIP6) and Reanalysis output

We also analyze output from a) thirteen coupled atmosphere-ocean simulations from the CMIP5 archive run with and without coupled chemistry processes and b) the Community Atmosphere Model 6 (CAM6) from the CMIP6 archive. The models all extend to at least 1 hPa and are all run with preindustrial forcings. The model output is linearly interpolated to the same 1.9° latitude by 2.5° longitude mesh and pressure levels as the WACCM output. Observations are derived from the European Centre for Medium-Range Weather Forecasts interim Re-Analysis [ERA-Interim; Simmons (2006)].

4.2.3 Analysis Methods

We analyze model (WACCM) output of anomalous monthly-mean temperature, ozone concentrations, short-wave (SW) heating rates, long-wave (LW) heating rates, and vertical velocity. Anomalies are defined as deviations from the long-term mean annual cycle at all grid points. The F statistic is used to assess the statistical significance of the ratios between variances. Area averages are weighted by pressure and cosine of latitude as necessary.

4.3 Results

Figure 4.1 and Figure 4.2 summarize the key differences in ozone and temperature variability between the "free-running" coupled-chemistry (FR) and specified-chemistry (SC) simulations. The top panels show the variances in zonal-mean ozone concentrations in the FR simulation (note that the variances are by construction zero in the SC simulation); the middle panels the variances in zonal-mean temperature in the FR simulation; the bottom panels the ratios of the variances in zonal-mean temperature between the FR and SC simulations. Figure 4.1 is based on output from all months of the year. Figure 4.2 highlights results at 60 hPa as a function of calendar month.

Ozone variability in the FR simulation increases markedly with height at stratospheric levels (Figure 4.1a). It exhibits two distinct maxima in the middle stratosphere: One at tropical latitudes

and another at polar latitudes (Figure 4.1a). At the 60 hPa level, variability in polar ozone peaks during the winter months in the Northern Hemisphere and during the late winter/spring months in the Southern Hemisphere (Figure 4.2a). Month-to-month variability in tropical ozone peaks during the NH winter months (Figure 4.2a), consistent with the season when the wave-driven vertical motion is largest in the tropical stratosphere [Yulaeva et al. (1994); Norton (2006); Randel et al. (2007); Grise and Thompson (2013)].

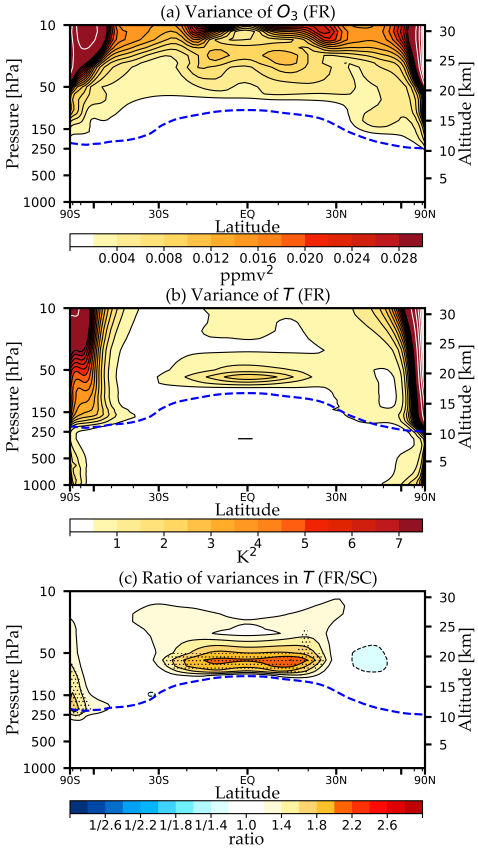

Figure 4.1: Variance in zonal-mean (a) ozone concentration and (b) temperature in the free-running coupled chemistry (FR) simulations. (c) Ratios of the variance in zonal-mean temperature between the coupled chemistry (FR) and fixed chemistry (SC) simulations. Stippling indicates regions where the ratios exceed the 95% threshold. The contour intervals with white solid lines are 10 times the contour intervals with black solid lines. The blue dashed line indicates the climatological-mean tropopause height in FR run. The mean tropopause heights in both simulations are effectively identical to each other.

As is the case for ozone, temperature variability in the FR simulation also exhibits distinct maxima in the polar stratosphere and the lower tropical stratosphere (Figure 4.1b). Variability in

polar temperatures peaks during the winter months in the Northern Hemisphere and during the late winter/spring months in the Southern Hemisphere (Figure 4.2b), consistent with the seasonally varying dynamic variability in the high latitude stratosphere [Andrews et al. (1987)]. Variability in tropical temperatures peaks during the NH winter months (Figure 4.2b), consistent with the seasonally varying dynamic variability in the tropical stratosphere [Yulaeva et al. (1994); Norton (2006); Randel et al. (2007); Grise and Thompson (2013)]. The most distinct differences between the patterns of temperature and ozone variance lie at tropical latitudes, where 1) the peak in temperature variance is found at lower altitudes than the peak in ozone variance (Figure 4.1a and Figure 4.1b) and 2) the temperature variance exhibits a more pronounced tropical maximum (Figure 4.2a and Figure 4.2b).

The ratios in zonal-mean temperature variance between the FR and SC simulations indicate that coupled chemistry leads to several significant changes in stratospheric temperature variance (Figure 4.1c and Figure 4.2c). By far the most pronounced differences in zonal-mean temperature variance between the FR and SC simulations are found in the lower tropical stratosphere. Coupled chemistry leads to increases in temperature variance of $>150\%$ throughout the tropical stratosphere from the tropopause to $\sim$30 hPa and $\sim 200\%$ around the $\sim$70 hPa level (Figure 4.1c). The increases in temperature variance in the FR run are highly significant and peak during the NH spring months February-June, when they approach 300% (Figure 4.2c). Weaker but significant temperature variance increases are found in both polar regions during local summer (Figure 4.2c), and temperature variance decreases are found in the middle latitudes, particularly during NH spring (Figure 4.2c).

Recent work has noted the importance of coupled chemistry for polar stratospheric temperature variability during the spring months [Rieder et al. (2019)]. The results in Figure 4.2 support these findings. But they also indicate that by far the most pronounced effects of coupled chemistry on stratospheric temperature variability are found not in the NH polar stratosphere, but in the lower tropical stratosphere, where temperature variances increase by up to a factor of three when coupled-chemistry is included in the simulation.

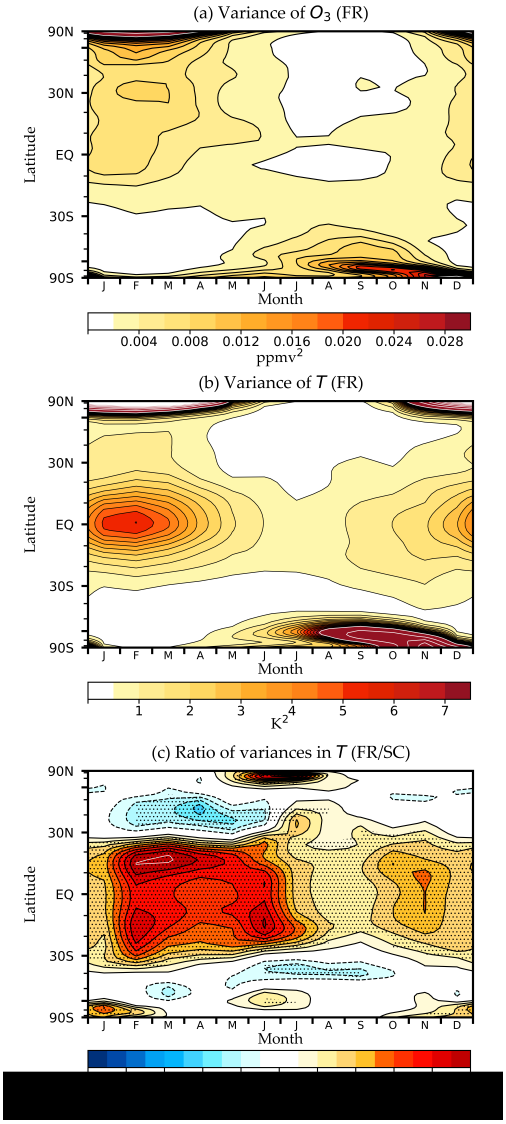

Figure 4.2: As in Fig. 1, but for the variance in zonal-mean ozone concentrations and temperature at 60 hPa for each calendar month. In (c) solid (dashed) contours are used for ratio values larger (smaller) than 1.

4.4 Interpretation

Why does coupled-chemistry lead to increases in stratospheric temperature variance? FR-WACCM and SC-WACCM differ from each other only in their treatment of atmospheric chemistry. They have identical seasonal cycles, but only FR-WACCM includes intraseasonal and interannual variability in ozone about the seasonal cycle. We hypothesize that the changes in temperature variance with coupled chemistry arise primarily from the changes in both shortwave and longwave heating on dynamically induced variations in ozone.

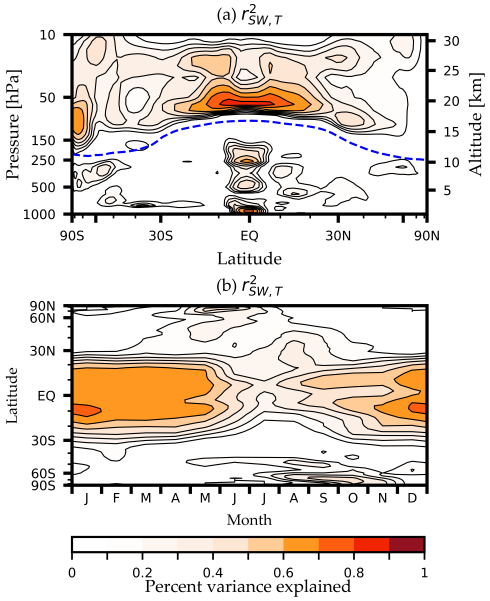

Figure 4.3: Percentage of (a) zonal-mean temperature variability explained by variations in the zonal-mean SW heating rates in the FR simulation. (b) As in (a), but for results at 60 hPa as a function of calendar month.

To test this hypothesis we show first the temperature variance explained by variations in SW heating rates in the FR simulation. Variations in shortwave heating account for a relatively large fraction of the temperature variance in two primary regions: 1) the tropical stratosphere and 2) the SH polar stratosphere during spring (Figure 4.3a and Figure 4.3b). The correlations are particularly high in the lower tropical stratosphere, where they approach r=0.92 based on 200 years of monthly-mean output. In contrast, variations in shortwave heating account for a

relatively small fraction of the temperature variance in the middle latitude stratosphere. Figure 4.3 thus reveals that 1) regions where variations in the SW heating rates explain a large fraction of the variability in the temperature field (Figure 4.3a) correspond closely to 2) regions where the inclusion of coupled chemistry leads to increases in the temperature variance (Figure 4.1c).

We also note that small increases in temperature variance are found over the polar stratosphere in the Southern hemisphere. We attribute the smaller correlation between SW radiation and temperature in the Northern hemisphere compared to the Southern hemisphere to 1) the larger contribution of polar vortex dynamics and internal atmospheric variability to stratospheric temperature variability in the NH, and 2) positive ozone-temperature feedbacks associated with heterogeneous ozone chemistry on PSCs (cooling enhances catalytic ozone depletion), which occur more efficiently in the Southern hemisphere.

This is supported by Figure 4.3b which reveals increases in the Northern Hemisphere correlations between SW and T during April to July (when the strength of the wave-driven circulation is weaker) and almost zero correlations during October-February when the wave-driving is a dominant factor determining temperature variability. Also, increases in the correlations between SW and T in the Southern hemisphere are larger during the Antarctic spring (from September to November).

We computed similar results for LW heating (Figure 4.4). Variations in LW heating include changes not only in the absorption and emission of longwave radiation by ozone, but also in the longwave emission by all radiatively active gases (the Planck feedback). As discussed below, the changes in absorption and emission of longwave radiation by ozone likely play an important role in setting the vertical structure of the temperature response to coupled chemistry, much as they play an important role in the seasonal cycle of lower stratospheric temperatures [Gilford and Solomon (2017)].

Why are the SW heating rates most closely coupled to stratospheric temperatures in the tropical stratosphere? Variability in SW heating is expected to contribute most to temperature variability in regions where 1) the mean shortwave radiation is large and/or 2) other radiative processes (e.g.,

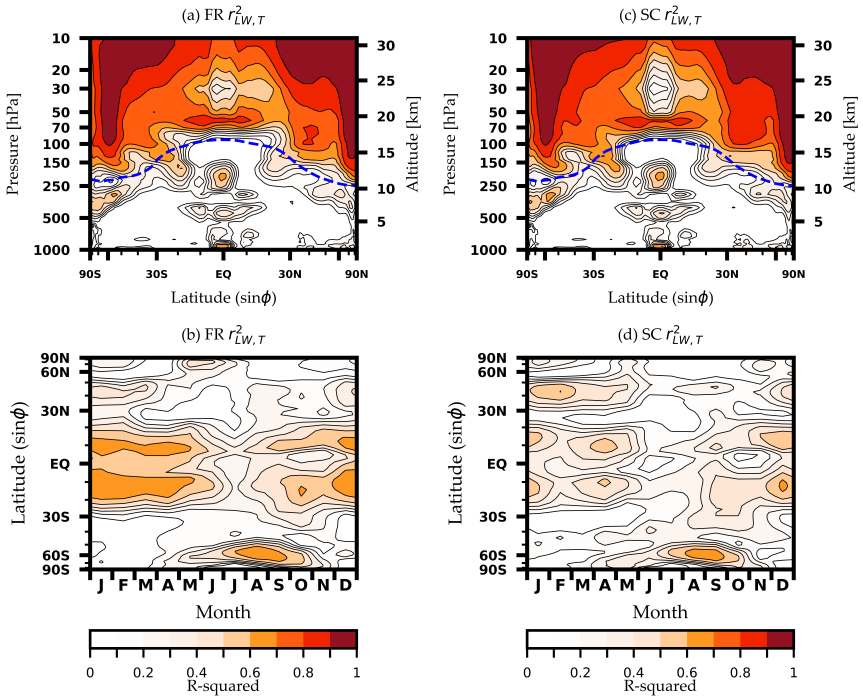

Figure 4.4: Correlation coefficients between the longwave cooling rates and temperature in (left) FR and (right) SC.

longwave radiative relaxation) or dynamical processes (e.g., the eddy transports of heat) do not dominate the thermodynamic energy budget. Both conditions are met in the tropical stratosphere and - to a lesser extent - at high latitudes during the warm season months. The seasonal cycle of the variances explained by SW heating (Figure 4.3b) follows from the seasonal cycle of the ozone variances (Figure 4.2a). Within the tropics, dynamically-driven variations in vertical motion - and thus ozone - are most pronounced during the NH cold season months [Figure 4.2a; Yulaeva et al. (1994)]. As such, variations in SW heating account for a larger fraction of variability in temperature during roughly the same season (Figure 4.3b).

And why are the SW heating rates more closely coupled to temperatures in the lower stratosphere (i.e., below 50hPa) than the middle stratosphere? The vertical structures of both 1) the temperature variances explained by SW heating (Figure 4.3a) and 2) the increases in temperature variances between the FR and SC simulations (Figure 4.1c) are consistent with the competing longwave and shortwave radiative effects of ozone. For example: Consider the tropical

stratospheric response to anomalous downward motion. The resulting dynamically-induced increases in stratospheric temperatures and ozone should lead to anomalous SW heating through changes in the transmission and absorption of solar radiation, anomalous LW heating due to the absorption of upwelling and downwelling radiation within the 9.6 micron band, and anomalous LW cooling due to increased temperature [Petty (2006); Plass (1956); Kiehl and Solomon (1986); Gilford and Solomon (2017)]. The different effects are not vertically uniform: Both the SW heating and LW cooling will be larger in the middle stratosphere where ozone concentrations are high, there is more ultraviolet radiation, and there is less absorption overhead. In contrast, the LW heating by ozone will be largest in the lower stratosphere due to increased absorption of 1) upwelling longwave radiation from the troposphere and 2) downwelling longwave radiation from the middle stratosphere. As a result of the above, LW cooling due to ozone is more effective at damping temperature changes in the middle stratosphere than it is in the lowermost stratosphere, and the net radiative effects of ozone variability on stratospheric temperatures should be most pronounced in the lower stratosphere [e.g., see also de F. Forster and Shine (1997); Fels et al. (1980)].

To analyze the influence of dynamically driven ozone variability on the stratospheric temperature, we regressed zonal-mean temperature, ozone, SW heating rates, and LW heating rates against a simple index that measures the dynamical upwelling in the tropical stratosphere (Figure 4.5 and Figure 4.6). Recall that the LW heating rates include both the effects of changes in emissivity and temperature, and thus the LW fluxes shown below include changes in both 1) absorption and emission of both upwelling and longwave radiation within the 9.6 micron band and 2) the Planck feedback.

The tropical upwelling index was formed as follows:

1) The Eulerian-mean vertical velocity was averaged 20°S-20°N and between 100 hPa and 10 hPa level as a function of calendar month to form a time series $w(t)$ of tropical stratospheric vertical velocity, where t denotes each month.

2) The lag between tropical upwelling and stratospheric temperatures [Newman and Rosenfield (1997); Randel et al. (2002); Ueyama and Wallace (2010)] was accounted for by averaging consecutive values of the resulting monthly-mean vertical velocity time series, such that $W(t) = 2/3 \times w(t-1) + 1/3 \times w(t)$, where $W(t)$ is the tropical upwelling index.

3) The resulting tropical upwelling index $W(t)$ values were standardized so that a unit change in the index corresponds to a typical fluctuation in tropical stratospheric vertical velocity. Note that the tropical upwelling index $W(t)$ is defined as an average of vertical velocity in pressure coordinates. Thus, positive values of the index correspond to anomalous downward motion, and vice versa.

In practice, the tropical upwelling index can be recovered as a linear combination of the first two PCs of tropical stratospheric vertical velocity anomalies in both SC and FR, which explain more than 95$\%$ of the variability in the tropical stratospheric vertical velocity field.

Figure 4.5 and Figure 4.6 explore the differences in radiative effects between FR and SC associated with a typical fluctuation in tropical upwelling. The top panels show the differences between 1) temperature regressed on $W(t)$ in FR-WACCM and 2) temperature regressed on $W(t)$ in SC-WACCM. Subsequent panels show comparable results for ozone concentrations, SW heating rates and LW heating rates, respectively. Figure 4.5 shows results for all months of the year. Figure 4.6 highlights results at 60 hPa as a function of calendar month.

Anomalous sinking motion in the tropics (i.e., positive values of the tropical upwelling index $W(t)$) leads to larger increases in atmospheric temperatures due to adiabatic warming in FR than it does in SC, as evidenced by the differences in the regression coefficients shown in the top panels in Figure 4.5 and Figure 4.6. The larger temperature response in FR is primarily confined to the lower stratosphere at tropical latitudes (Figure 4.5a). The temperature anomalies associated with a typical fluctuation in vertical motion in FR exceed those in SC by up to 0.6 $K\,month^{-1}\,\sigma^{-1}$ (Figure 4.6a). The most pronounced differences between the regression patterns of temperature (Figure 4.6a) are found in the tropics during the NH winter months.

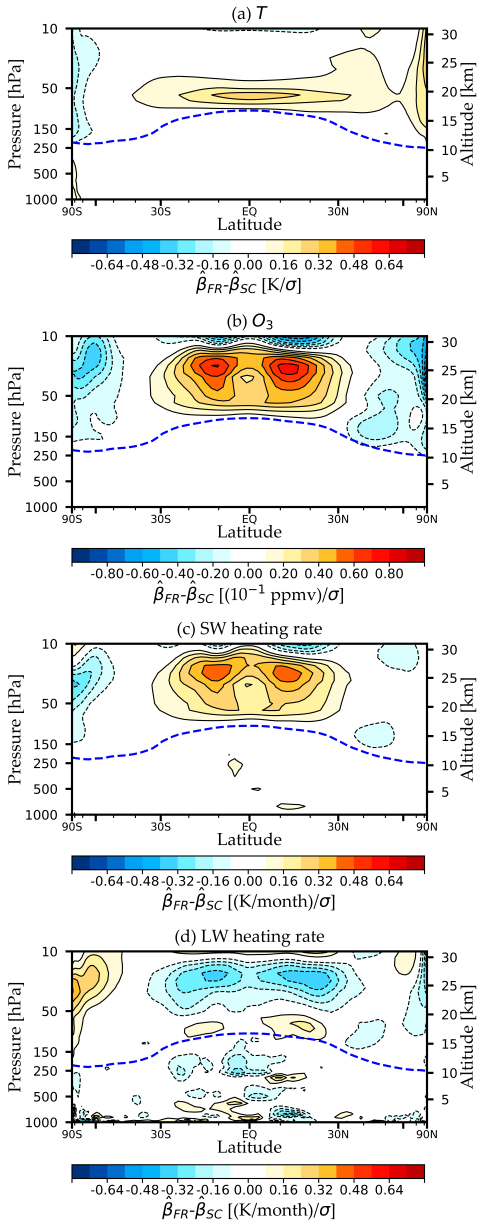

Figure 4.5: Differences between regressions on an index of tropical upwelling in the FR and SC simulations. Rows correspond to the differences in regression coefficients for (a) temperature, (b) ozone, (c) SW heating rate, and (d) LW heating rate. Results are based on output for all calendar months.

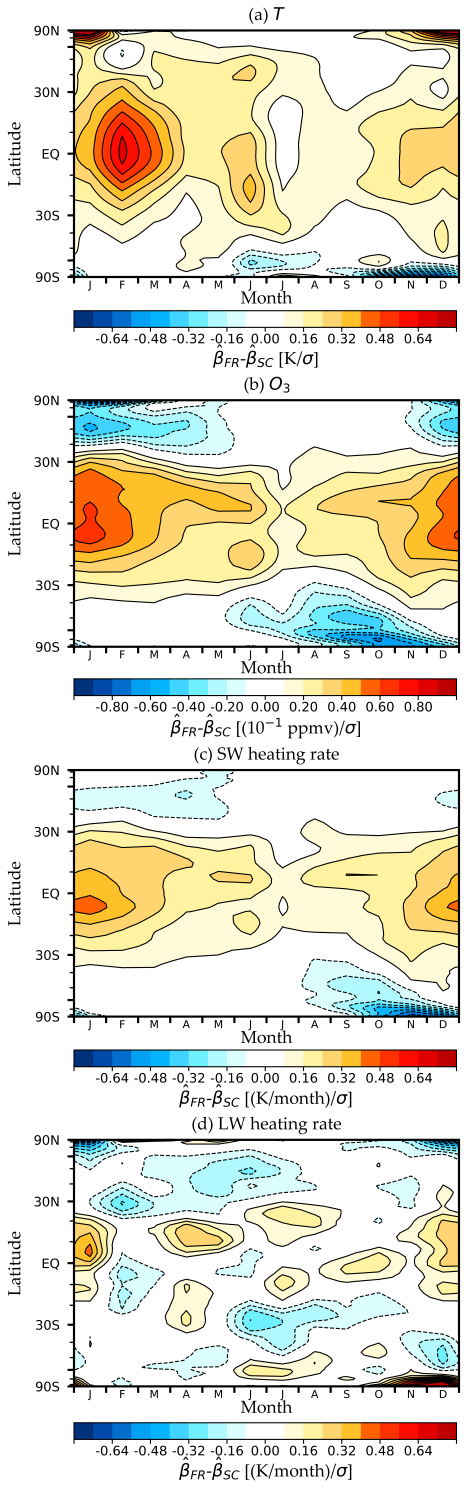

Figure 4.6: As in Fig. 4, but for the results at 60 hPa for each calendar month.

Anomalous downwelling in the tropical stratosphere is accompanied by widespread increases in ozone concentrations throughout the lower and middle tropical stratosphere below ∼15 hPa (Figure 4.5b). Note that since there is no ozone variability in SC, the results in Figures 4b and 5b are equivalent to the regressions for FR since the regression coefficients for SC are zero everywhere. The increases in ozone are consistent with anomalous downward transport of high ozone air from upper levels. Like the differences in temperature variations between the coupled and specified chemistry simulations, they also peak during the NH cold season months (Figure 4.6b). Unlike the differences in temperature variations between the coupled and specified chemistry simulations, the differences in ozone peak in middle stratosphere ∼30 hPa rather than ∼70 hPa. The decreases in ozone in the tropical stratosphere above ∼15hPa are consistent with the facts that 1) ozone is controlled primarily by photochemistry rather than transport there, and 2) warming due to anomalous downwelling leads to decreases in ozone through changes in the gas-phase catalytic destruction of ozone [e.g., Fusco and Salby (1999); Eyring et al. (2010)]. The decreases in ozone at high latitudes reflect the fact that anomalous downwelling in the tropical stratosphere is accompanied by anomalous upwelling at latitudes (vertical motion at high latitudes not shown).

The differences in SW heating rates between periods of tropical downwelling in the FR-WACCM and SC-WACCM simulations (Figure 4.5c and Figure 4.6c) are qualitatively very similar to the differences in ozone (Figure 4.5b and Figure 4.6b). At first glance, the differences in LW heating rates (Figure 4.5d and Figure 4.6d) bear close resemblance to the differences in ozone variability. However, closer inspection reveals that the anomalous cooling due to enhanced emission of longwave radiation is confined to levels above about 50hPa. That is: Anomalous LW cooling opposes anomalous SW heating at levels above ∼50 hPa, but is ∼zero or even weakly positive in the lower tropical stratosphere (Figure 4.5d and Figure 4.6d). The vertical structure of the differences in LW heating is consistent with the physical reasoning outlined earlier, namely that 1) the Planck feedback is more efficient at higher levels, where the opacity of the overlying atmosphere is smaller [Hitchcock et al. (2010)]; and 2) the increased absorption of both

downwelling and upwelling longwave radiation by ozone should be largest in the lower stratosphere, as is the case in the seasonal cycle there [Gilford and Solomon (2017)].

Together, the results in Figure 4.5 and Figure 4.6 suggest that the inclusion of ozone variability in coupled chemistry simulations is most effective at increasing the temperature variance in the lower tropical stratosphere since LW radiative cooling is less effective at opposing radiative heating there. The vertical profile of the increases in temperature variance due to coupled chemistry is thus consistent with our understanding of the radiative balance in the lower stratosphere and its relatively long radiative timescales [e.g., de F. Forster and Shine (1997); Fels et al. (1980); Hitchcock et al. (2010)]. In fact, consistent with our hypothesis, coupled chemistry leads not only to marked increases in lower tropical stratospheric temperature variance, but also in the memory in lower tropical stratospheric temperatures from one month to the next (Figure 4.7).

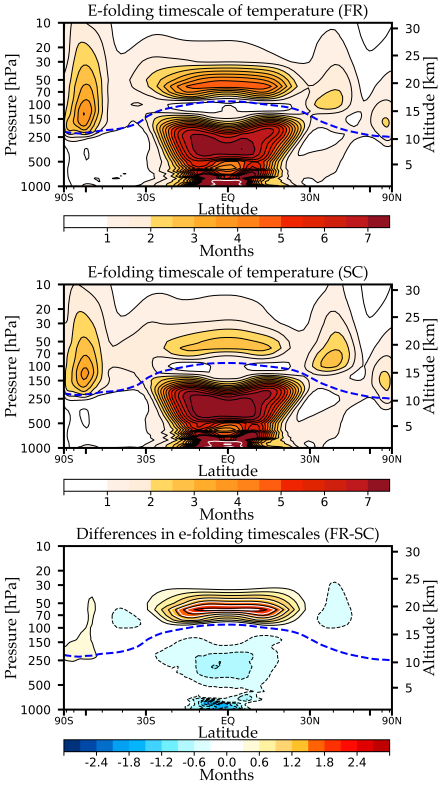

Figure 4.7: The e-folding time scale of zonal-mean temperature anomalies in (top) the coupled chemistry simulation (FR) and (middle) the prescribed chemistry simulation (SC), and (bottom) the differences between FR and SC.

Previous studies have suggested that dynamical feedbacks other than the ozone-radiation feedback highlighted here may affect tropical stratospheric temperature variability. For example, changes in the stratification of the atmosphere affect vertical motion and its influence on adiabatic temperature change [Birner and Charlesworth (2017); Fueglistaler et al. (2011)], and variations in the dynamical and radiative timescales affect stratospheric temperature variance [Charlesworth et al. (2019)]. Importantly, the differences in stratospheric temperature variance revealed here do not seem to derive from changes in the variance of stratospheric dynamics, that is, the variance of the temperature tendency due to vertical motion (ωS) is roughly unchanged in the tropical stratosphere between the FR and SC-WACCM simulations.

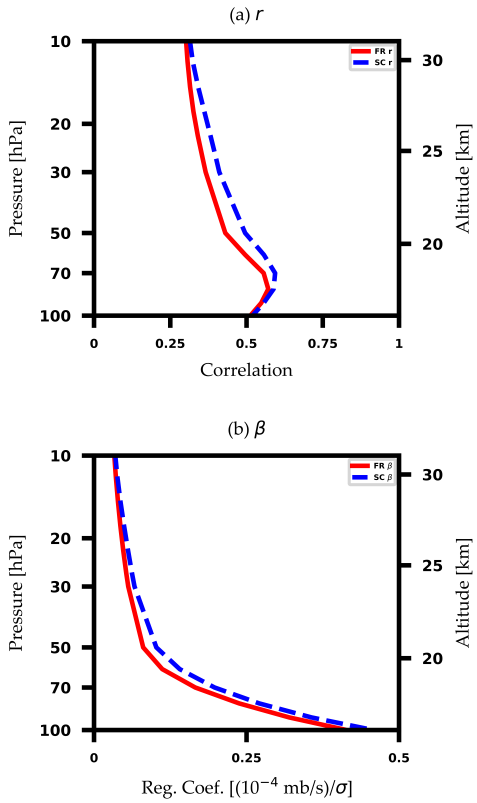

Figure 4.8: (upper panel) Correlations and (lower panel) regression coefficients between the tropical upwelling index and vertical velocities in the tropics in (red thick line) FR and (blue dashed line) SC.

To understand the relation between the tropical upwelling index and the vertical structure of the dynamical perturbation, we calculated the correlations and regression coefficients between the

vertical velocity fields averaged over the tropics (20S-20N) at each pressure level and the tropical upwelling index used in this study. The dynamical perturbation associated with the tropical upwelling index decreases exponentially with height (See Figure 4.8b at the end of our Responses.), and the correlations peak around 70 hPa level and decrease above the 50 hPa level (Figure 4.8).

We also applied EOF analysis of the vertical velocity field in the tropical stratosphere (20S-20N, 100-10 hPa). The covariance matrixes are weighted by pressure thickness. The leading EOFs of vertical velocity are very similar in the FR and SC simulations and together explain in excess of 95% of the total variance in the tropical stratospheric region (see Figures Figure 4.8 and Figure 4.9). In both FR and SC, the leading EOFs have vertical structures that are qualitatively similar to those associated with the tropical upwelling index and explain 77.5% and 78.8% of the total variances in FR and SC, respectively (Figure 4.8a-b and Figure 4.9a-b). The second EOFs change sign around 50 hPa, and explains 17.4% and 16.4% of the total variances in FR and SC, respectively (Figure 4.9c-d).

The tropical upwelling proxy and the PC time series of the first two modes are significantly ($p < 0.01$) correlated to each other (Table 4.1).

Thus, we infer that the tropical upwelling index used in this study is linear sum of the first two EOFs of the tropical vertical velocity field.

Table 4.1: Correlations between the tropical upwelling index and the PC time series of first three modes.

	Mode 1	Mode 2	Mode 3
FR	0.52	-0.22	-0.02
SC	0.56	-0.19	-0.05

To quantify the proportion of the each mode contributing to the variances in the proxy index, we performed multiple linear regression analysis. The tropical upwelling indexes have been

reconstructed using the PC time series of first 5 dominants modes as predictor variables (the total variances explained by the 5 modes exceed 99.9% both in FR and SC).

$$\mathbf{Y} = \sum_{n=1}^{5} a_n \mathbf{X_n} + \epsilon \tag{4.1}$$

Y denotes reconstructed time series of the tropical upwelling index, n denotes mode, a_n is regression coefficients and X_n is PC time series of each mode.

The first and second mode explains the 80.3% (86.8%) and 14.9% (10.6%) of the total variances in the tropical upwelling index in FR (SC), respectively.

To understand the vertical structure of the dynamical forcing associated with the tropical upwelling index, we reconstructed the vertical structure of the anomalies by combining the first few EOF modes weighted by the coefficients from the multiple linear regression analysis.

$$\mathbf{V} = \sum_{n=1}^{5} a_n \mathbf{V_n} (k = 2 or 5) \tag{4.2}$$

V denotes reconstructed EOF pattern, and V_n is each EOF mode.

The vertical structures of reconstructed variability modes (Figure 4.10) resemble the vertical structure derived from the linear regression (Figure 4.8) and are not sensitive to the number of modes used for the reconstruction if it includes first two modes.

The main conclusions drawn from the above analysis are summarized below: 1) The tropical upwelling index used in the study reflects - to first order - a linear combination of the first two EOFs of tropical stratospheric vertical velocity. This is now noted in the text. 2) The leading EOFs of vertical velocity are very similar in both SC and FR. 3) The structure of the perturbation supports why the temperature responses to ozone and its intraseasonal to interannual variability is most significant below the 50 hPa level.

The results indicated in Figure 4.1-Figure 4.6 also appear to extend to simulations used in the AR5 and AR6 reports. Figure 4.11 compares the lower stratospheric temperature variance in FR-WACCM and SC-WACCM with that found in the observations (ERA-Interim), a range of

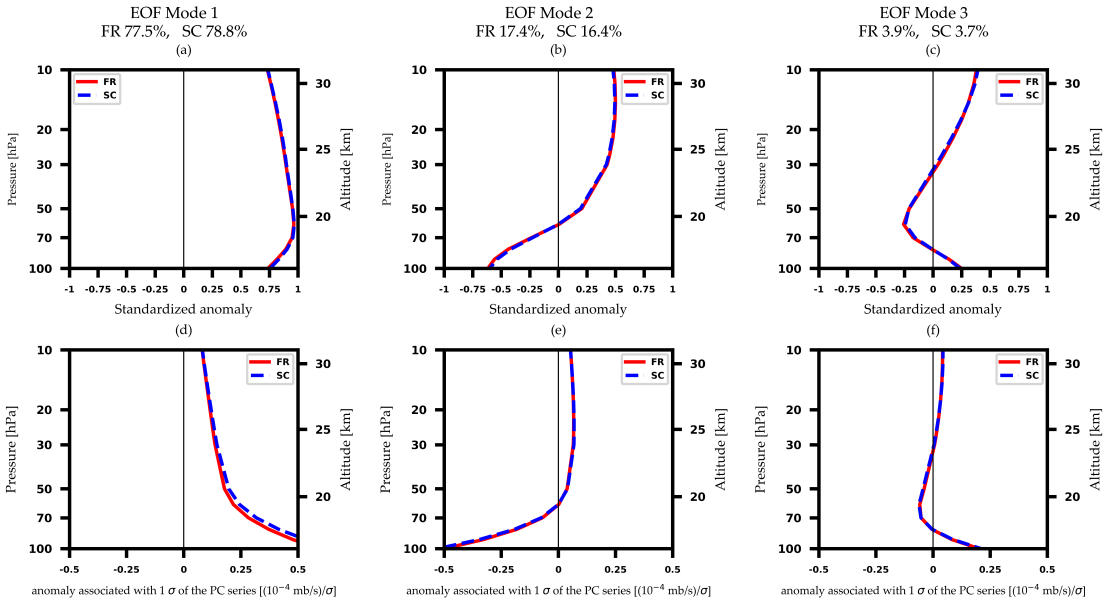

Figure 4.9: Anomalies associated with 1 standard deviation of the PC time series. Each column denotes each (first to third) mode of the variability. Upper panels are anomalies divided by the standard deviation of vertical velocity at each level.

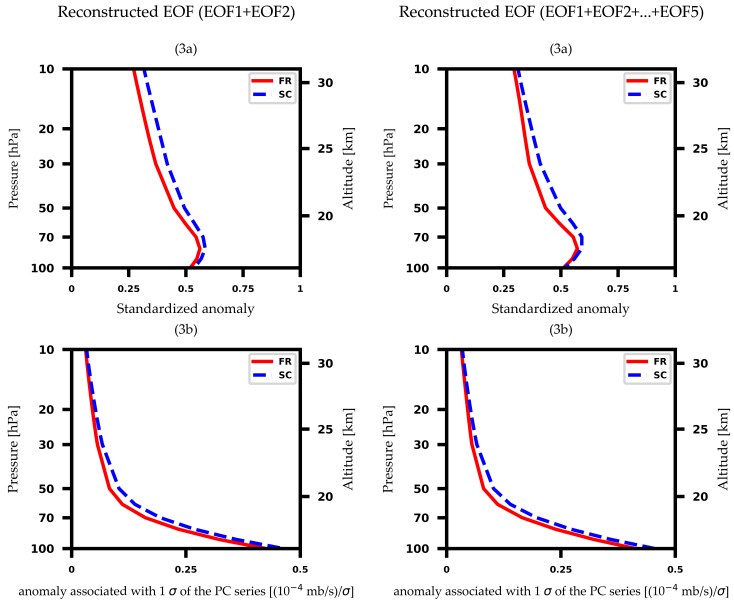

Figure 4.10: Figure 4.9, but for the vertical structure of reconstructed variability modes using (left) the first two (1st and 2nd) and (right) first five (from 1st to 5th) modes.

high-top CMIP5 models, and output from the low-top version of the NCAR Community Atmospheric Model (CAM6) used in the AR6 report. The high-top models are grouped into two different categories: 1) models with a parameterized QBO (left); and 2) models without a QBO (right). The temperature variances are found in model output by 1) forming temperature anomalies by removing the long-term mean seasonal cycle from the output; 2) averaging the anomalies over the region 30°S-30°N and 70-50 hPa, and then 3) computing the variances of the spatially averaged-temperature time series. The observed variance is found in a similar manner, except that we also remove the influence of volcanic eruptions since they are not included in the numerical output. The influence of volcanic eruptions on lower stratospheric temperature variance is mitigated by excluding data during 1982-1984 and 1991-93 (i.e., the years surrounding the eruptions of El Chichón and Mount Pinatubo, respectively).

Together, the results in Figure 4.11 reveal that: 1) models with interactive chemistry (FR-WACCM, GFDL-CM3, and MIROC-ESM-CHEM) all indicate larger tropical stratospheric temperature variances than models with prescribed chemistry, when the output is binned by model treatments of the QBO; 2) The tropical stratospheric temperature variance in the coupled chemistry version of WACCM (FR) is very similar to the observed, whereas the variance in the prescribed chemistry version (SC) notably underestimates the observations (Figure 4.11); and 3) The tropical stratospheric variance in CAM6 (far right bar in Figure 4.11) is similar to that found in the prescribed chemistry version of WACCM, and thus also significantly underestimates the observations.

Figure 4.12 shows the correlations between the SW heating rate and temperature in the troposphere. We have not analyzed the physical mechanisms accounting for the correlations in the tropical troposphere in details, since 1) they appear not only in FR but also in SC (see a and c in Figure 4.12, below), and 2) the magnitude of the temperature changes associated with variations in SW heating are negligible there (see b and d in Figure 4.12, below). However, we suspect that the positive correlations in the tropical troposphere may arise from the linkages between clouds

and shortwave cooling. But exploring the linkages between clouds and SW cooling is beyond the scope of this paper.

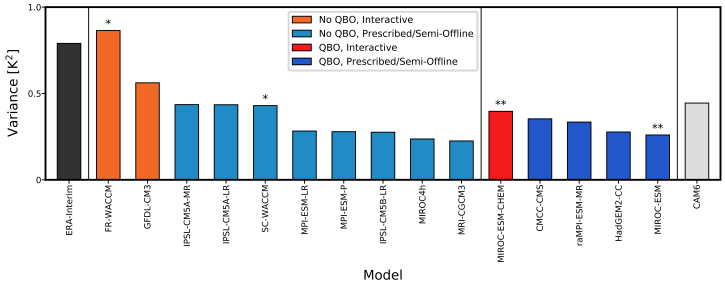

Figure 4.11: The temperature variances in the lower tropical stratosphere in the observations (ERA-Interim), high-top models from the CMIP5 archive, and CAM6 from the CMIP6 archive. Orange- and red-colored bars denote models with interactive chemistry, while cyan- and blue-colored bars denote models with prescribed chemistry. Orange and cyan bars denote models with a QBO parameterization, while red and blue bars denote models without QBO parameterization. The black bar denotes ERA-Interim and the gray bar denotes CAM6.

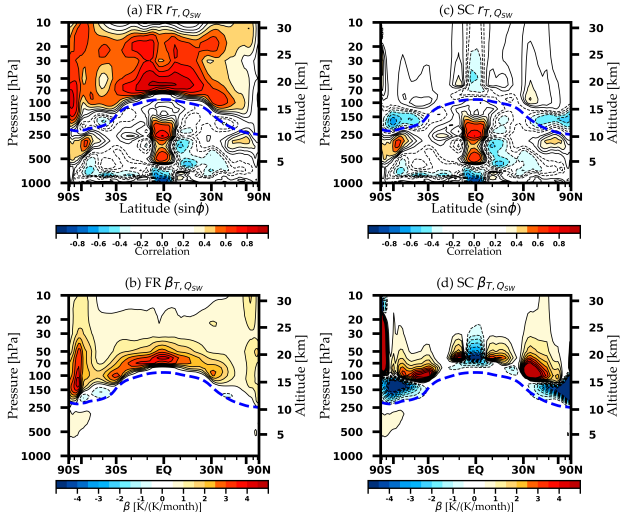

Figure 4.12: (upper panel) Correlations between the temperature and SW heating rate in (left) FR and (right) SC. (lower panel) As in upper panels, but for the regression coefficients.

4.5 Discussion

Previous studies have suggested that "the climatology and variability of the stratosphere ... [is] nearly identical" in simulations run on coupled and prescribed-chemistry versions of the NCAR Whole Atmosphere Community Climate Model [Smith et al. (2014)]. The results shown here indicate that - in fact - coupled-climate chemistry interactions play an *essential* role in driving temperature variability in the tropical lower stratosphere and - to a lesser extent - the polar regions during summer. In the tropical lower stratosphere, simulations with explicit interactions between dynamics, ozone and radiation indicate $\sim$two fold increases in month-to-month temperature variability relative to simulations with prescribed chemistry. The increases in lower tropical stratospheric temperature variance are consistent with the changes in shortwave and longwave radiative heating rates that accompany dynamically-driven ozone variability in tropical stratosphere. The variance increases are most pronounced in the lowermost stratosphere where 1) heating due to the absorption of both upwelling and downwelling longwave radiation are important [Gilford and Solomon (2017)] and 2) longwave radiative cooling is relatively inefficient at damping temperature variability on monthly timescales.

The conclusions are drawn from analyses of 200 year long simulations run on two different versions of the WACCM: 1) a fully coupled-chemistry version of the model [FR-WACCM; Marsh et al. (2013)] and 2) a specified chemistry version of the model [SC-WACCM; Smith et al. (2014)]. Importantly, they also extend to models run for IPCC AR5: Lower stratospheric temperature variability is consistently larger in models with interactive chemistry relative to models with prescribed chemistry. Hence the results indicate the critical role of explicitly simulated coupled-chemistry interactions for the fidelity of simulating stratospheric climate variability in climate change simulations.

Variations in lower tropical stratospheric temperatures play an outsized role in global climate variability [e.g., Fueglistaler et al. (2011)]. They set the amplitude of stratospheric water vapor concentrations [Brewer (1949); Fueglistaler et al. (2009)] which, in turn, play a key role in the radiative forcing at the tropopause [de F. Forster and Shine (1999)]. The climatological-mean

seasonal cycle of water vapor in the tropical upper troposphere-lower stratosphere region is well simulated in both FR-WACCM and SC-WACCM [Smith et al. (2014)]. However, in contrast to ozone, water vapor is not strictly prescribed in the SC simulation. For example, like ozone, stratospheric water vapor concentrations in FR-WACCM are calculated using prognostic chemistry. However, unlike ozone, stratospheric water vapor concentrations in SC-WACCM are not prescribed from annually repeating values, but rather are calculated including transport, approximate methane oxidation and photolysis rates. Hence, it is difficult to use the differences between FR-WACCM and SC-WACCM to assess the role of coupled chemistry on stratospheric water vapor variability. We view it critical for future work to quantify the importance of the nearly two-fold increase in temperature variability documented here for stratospheric water vapor and the resulting radiative forcing of the tropopause as well as its possible influences on tropospheric climate.

Chapter 5

Wildfire-Climate Interactions[3]

The latter months of 2020 and 2021 were marked by two of the largest Antarctic ozone holes on record. That such large ozone holes occurred despite ongoing ozone recovery raises questions about their origins and climate impacts. Here we provide novel evidence that supports the hypothesis that the ozone holes were influenced by two distinct and extraordinary events: the Australian wildfires of early 2020 and the eruption of La Soufriere in 2021. We further reveal that both ozone holes were associated with widespread changes in Southern Hemisphere climate that are consistent with the established climate impacts of Antarctic ozone depletion, including a strengthening of the polar stratospheric vortex, enhanced surface westerlies over the Southern Ocean, and surface temperature changes over Antarctica and Australia. The results thus provide suggestive evidence that injections of both wildfire smoke and volcanic emissions into the stratosphere can lead to hemispheric-scale changes in surface climate.

5.1 Introduction

The Antarctic ozone hole has a pronounced effect on Southern Hemisphere surface climate [Thompson and Solomon (2002); Thompson et al. (2011); Polvani et al. (2011); Fogt and Marshall (2020)]. The radiative effects of polar ozone depletion act to cool and strengthen the stratospheric polar vortex [Randel and Wu (1999); Waugh et al. (1999)], and dynamical coupling between the stratosphere and troposphere acts to connect the changes in the stratospheric flow to the surface [Baldwin and Dunkerton (2001); Thompson et al. (2005)]. At the surface, the changes in the flow associated with the ozone hole project onto the southern annular mode [Thompson and

[3]The results outlined in Chapter 5 have been published in the *Geophysical Research Letters*: Yook, S., D. W. Thompson, and S. Solomon, 2022a: Climate impacts and potential drivers of the unprecedented antarctic ozone holes of 2020 and 2021. *Geophysical Research Letters*, **49 (10)**, e2022GL098 064.

Solomon (2002); Shindell and Schmidt (2004)]. Thus the ozone hole has been linked to long-term changes in surface climate that span much of the Southern Hemisphere mid and high latitudes.

The linkages between the Antarctic ozone hole and the SAM are important for the interpretation of Southern Hemisphere climate change. Over the 1970s-1990s, the development of the ozone hole was associated with widespread changes in Southern Hemisphere surface climate that are consistent with forcing by ozone depletion [Thompson et al. (2011)]. Paleoclimate studies indicate that the resulting changes in the austral summer SAM index are unprecedented over the last thousand years, pointing toward the remarkable role of the ozone hole in Southern Hemisphere climate change [Fogt and Marshall (2020)].

In recent years, the Antarctic ozone hole has exhibited signs of healing consistent with recent decreases in anthropogenic emissions of ozone-depleting substances [Solomon et al. (2016)]. The healing of the ozone hole is apparent when viewed in the context of decades, especially during September when dynamic variability in the vortex is modest [Abrahamsen et al. (2020); Hassler et al. (2011); Solomon et al. (2016); Strahan et al. (2019)]. Recent studies have correspondingly shown that trends in the SAM have paused or slightly reversed [Banerjee et al. (2020); Zambri et al. (2021)]. Yet the ozone holes of late 2020 and 2021 rate amongst some of the largest on record during October and later months, and they have obscured the overall trend towards recovery of the ozone hole [https://ozonewatch.gsfc.nasa.gov; Stone et al. (2021)].

Why were the ozone holes of 2020 and 2021 so large given the overall trend towards ozone recovery? One possibility is internal dynamical variability. That is: the ozone hole forms due to chemical processes, but atmospheric dynamics contribute to year-to-year variations in its size and strength, particularly during October and November [Randel et al. (2002); Shindell et al. (1997); Weber et al. (2011); Safieddine et al. (2020); Wargan et al. (2020)]. Years marked by anomalously weak extratropical stratospheric wave driving are associated with anomalously low polar cap ozone concentrations due to both 1) dynamically-induced changes in ozone transport and 2) feedbacks between polar stratospheric temperatures and heterogeneous ozone chemistry. The Southern Hemisphere stratospheric wave driving was unusually weak in late 2020 and 2021

(https://ozonewatch.gsfc.nasa.gov) and thus dynamical processes likely contributed to the size of the 2020 and 2021 ozone holes.

Another possibility is that the 2020 and 2021 ozone holes were influenced by anomalously large stratospheric aerosol loadings due to two episodic events: The catastrophic Australian bushfires of early 2020 and the April 2021 eruption of La Soufriere on Saint Vincent.

The Australian bushfires of early 2020 injected large amounts of particulate matter into the stratosphere [Hirsch and Koren (2021); Khaykin et al. (2020); Magaritz-Ronen and Raveh-Rubin (2021); Ohneiser et al. (2020); Peterson et al. (2021); Schwartz et al. (2020); Yu et al. (2021); Ansmann et al. (2022)]. Observations indicate that some of the smoke settled into the Southern Hemisphere polar stratosphere in the latter part of 2020 [Khaykin et al. (2020); Peterson et al. (2021); Yu et al. (2021); Ansmann et al. (2022)]. Wildfire smoke is theorized to contribute to ozone depletion if the smoke particles become coated with sulfuric acid and water as they age, so that they behave like liquid polar stratospheric cloud particles and thus provide a surface for heterogeneous chemistry [Ansmann et al. (2021); Ansmann et al. (2022); Yu et al. (2021)]. Solomon et al. (2022) provide observational evidence supporting this view.

The April 2021 eruption of La Soufriere on Saint Vincent contributed to the stratospheric sulfate aerosol burden in the tropics in mid-2021 [Babu et al. (2022)] and - as suggested here - late-2021 as well. Previous work has argued that volcanic eruptions can influence the stratospheric circulation through a variety of processes. The absorption of longwave radiation by volcanic aerosols directly influences stratospheric temperatures and thus winds [e.g., Kodera (1994); Robock and Mao (1995); Robock (2000); Toohey et al. (2014); DallaSanta et al. (2019)]; indirect mechanisms have also been proposed [e.g., Coupe and Robock (2021)] The resulting changes in stratospheric temperatures and winds can contribute to changes in ozone transport and temperature-dependent heterogeneous ozone chemistry [Langematz et al. (2018); Weber et al. (2011)]. And volcanic sulfuric acid aerosols provide a surface for heterogeneous ozone chemistry [Portmann et al. (1996); Solomon (1999); Tabazadeh et al. (2002); Wilka et al. (2018)].

Here we demonstrate that both the 2020 and 2021 Antarctic ozone holes were associated not only with large stratospheric aerosol loadings but also pronounced changes in the Southern Hemisphere circulation that extended from the stratosphere to the surface. Our goal is not to prove the specific physical mechanisms that drove the unusual 2020 and 2021 Antarctic ozone holes. Rather, it is to document a series of physically consistent linkages between the Australian bush fires in early 2020, the eruption of La Soufriere on Saint Vincent in April 2021, the 2020 and 2021 ozone holes, and hemispheric-scale changes in the Southern Hemisphere tropospheric circulation. The results are of interest irrespective of causal factors. If the 2020 and 2021 ozone holes arose due to internal variability or dynamical forcing by particulate matter, then the results point to surprising effects of the ozone hole on SH surface climate despite evidence for ozone recovery. If the unusually strong 2021 ozone hole was influenced by the eruption of La Soufriere, then the results add to the already substantial body of evidence that volcanoes influence surface climate over regions far removed from the eruption itself. And if the unusually strong 2020 ozone hole was influenced by smoke from the Australian bush fires, then the results suggest that large injections of wildfire smoke into the stratosphere can lead to widespread changes in surface climate that persist long after the cessation of smoke production.

5.2 Data and Methods

Ozone and extinction values for 2020 and 2021 are based on data from the Ozone Mapping and Profiler Suite Limb Profiler (OMPS-LP) instrument [Taha et al. (2021); Zawada et al. (2018)]. OMPS-LP measurements have been used in numerous studies of the Antarctic ozone hole [Kramarova et al. (2014); Yu et al. (2021); Rieger et al. (2021)]. Aerosol extinction is retrieved at a single wavelength channel of 745 nm and clouds are removed using the cloud detection algorithm [Chen et al. (2016)]. OMPS-LP ozone concentrations below 10 hPa are derived from visible wavelengths. OMPS-LP observations are weighted for the number of samples when observations are available, and area averages are weighted by pressure and the cosine of latitude

as necessary. Tropospheric aerosol extinction and ozone concentrations are neglected in the calculations of all vertical averages.

Ozone values for the extended 1979-2021 period were obtained from the NASA ozone watch and consist of Southern Hemisphere polar cap ozone hole area and total column ozone values (http://ozonewatch.gsfc.nasa.gov). Atmospheric temperatures, winds, and geopotential height are based on the European Centre for Medium-Range Weather Forecasts Re-Analysis 5 [Hersbach et al. (2020)].

All results are shown as anomalies with respect to the 2012-2019 mean seasonal cycle (the OMPS-LP data are available starting 2012). We omit 2015 from the base climatology since it was marked by large stratospheric aerosol loadings from the Calbuco eruption [Zhu et al. (2018)].

5.3 Results and Discussion

5.3.1 Aerosol burdens and ozone depletion in 2020 and 2021

Figure 5.1A and Figure 5.3A summarize the aerosol loadings that occurred in the Southern Hemisphere over the 2020-2021 period. Figure 5.1A shows extinction at 100 hPa as a function of latitude and day of year; Figure 5.3A shows extinction averaged over the extratropics (30-90S) as a function of height and day. As shown in previous studies [Khaykin et al. (2020); Peterson et al. (2021); Yu et al. (2021); Ansmann et al. (2022)], the SH lower stratosphere was marked by enhanced extinction values throughout 2020. Extinction increased rapidly following the Australian bush fires in January and persisted throughout the SH middle and high latitudes until at least the end of the year [Figure 5.1A, Figure 5.3A; Khaykin et al. (2020); Peterson et al. (2021); Yu et al. (2021); Ansmann et al. (2022)]. The lag between the fires in early 2020 and the emergence of high extinction values in the lower polar stratosphere in late 2020 (Figure 5.1A) is consistent with the lofting of material at low latitudes followed by the poleward transport and descent of particles at polar latitudes [see also Rieger et al. (2021), figure 3]. The signature of the fires is partially obscured by the lack of data in polar night (Figure 5.1A) and below the tropopause (Figure 5.3A). Nevertheless, the time evolution of extinction in 2020 strongly suggests

that the high polar values found in late 2020 originated from the Australian fires that occurred earlier that year [Yu et al. (2021)].

The SH lower stratosphere was also marked by enhanced extinction values throughout 2021. In this case, the increases in extinction began soon after the eruption of La Soufriere in the tropics (Figure 5.1A, Figure 5.3A). Interestingly, the polar extinction anomalies in late 2021 are comparable to those in late 2020. It is noteworthy that the extinction values are shown with respect to the OMPS climatology in years without major eruptions (Methods), and thus the high values at polar latitudes do not reflect the seasonal cycle of aerosol loadings. Further, the OMPS aerosol extinction values are based on a cloud screened version of the data which filters out the possible influence of clouds, including polar stratospheric clouds [Chen et al. (2016)].

Figure 5.1B and Figure 5.3B summarize the attendant anomalies in ozone concentration. Figure 5.1B again shows results at 100 hPa while Figure 5.3B shows results averaged over the polar regions (50-90S). The ozone anomalies are shown with respect to the same base as that period used for extinction. As noted in Stone et al. (2021), the 2020 ozone hole was among the largest on record in October. From Figure 5.1B and Figure 5.3B , it is clear that the 2021 polar ozone anomalies were comparable in magnitude to those found in 2020. Interestingly, the large 2021 ozone hole was preceded by large wintertime ozone anomalies in the middle stratosphere that bear the hallmark of dynamic variability (Figure 5.3B). The unusual nature of the 2020 and 2021 ozone holes is apparent in their sizes [Stone et al. (2021)]. It is also apparent in the magnitude of the ozone anomalies with respect to the rest of the OMPS record (Figure 5.3A and Figure 5.3B).

5.3.2 Connections to the hemispheric-scale circulation and surface climate

Figure 5.1C and Figure 5.3C summarize the accompanying changes in the atmospheric circulation. Figure 5.1C shows the changes in geopotential height at 100 hPa; Figure 5.3C reveals the vertical structure of geopotential height anomalies averaged over the polar cap (60-90S). The 2020 and 2021 ozone holes were both associated with large decreases in polar stratospheric

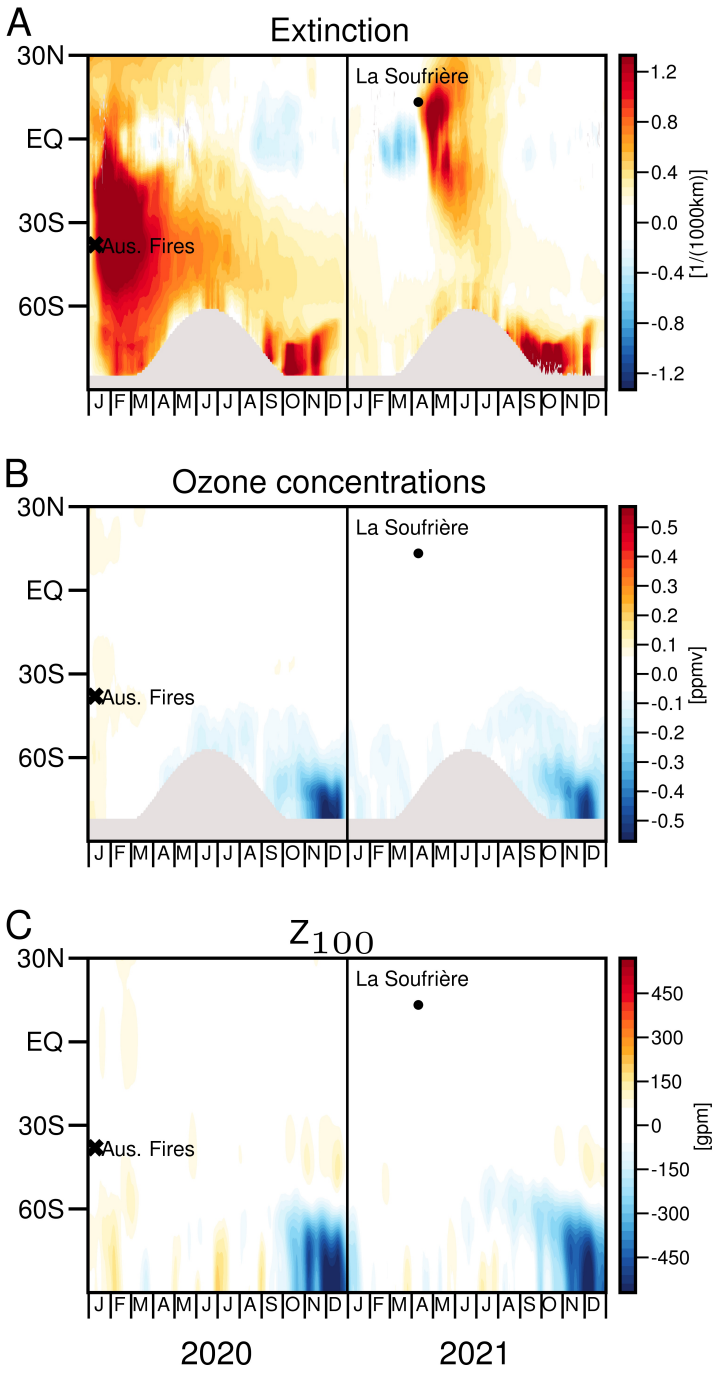

Figure 5.1: Time series of zonal-mean stratospheric aerosol extinction, ozone concentrations, and geopotential height anomalies during 2020-2021. Results are shown at the 100 hPa level (Panels A and B are shown at the 70 hPa level in Figure 5.2). The cross and dot indicate the Australian bushfires of early 2020 and the April 2021 eruption of La Soufriere, respectively. Aerosol extinction (A, 10^{-3} km^{-1}) and ozone concentrations (B, ppmv) are derived from the OMPS-LP instrument. Geopotential heights (C, in geopotential meters; gpm) are derived from ERA5. Anomalies are calculated with respect to the base period 2012-2019 (omitting 2015 due to the eruption of Calbuco). The results are smoothed with an 11-point (11-degree by 11-day) running mean filter.

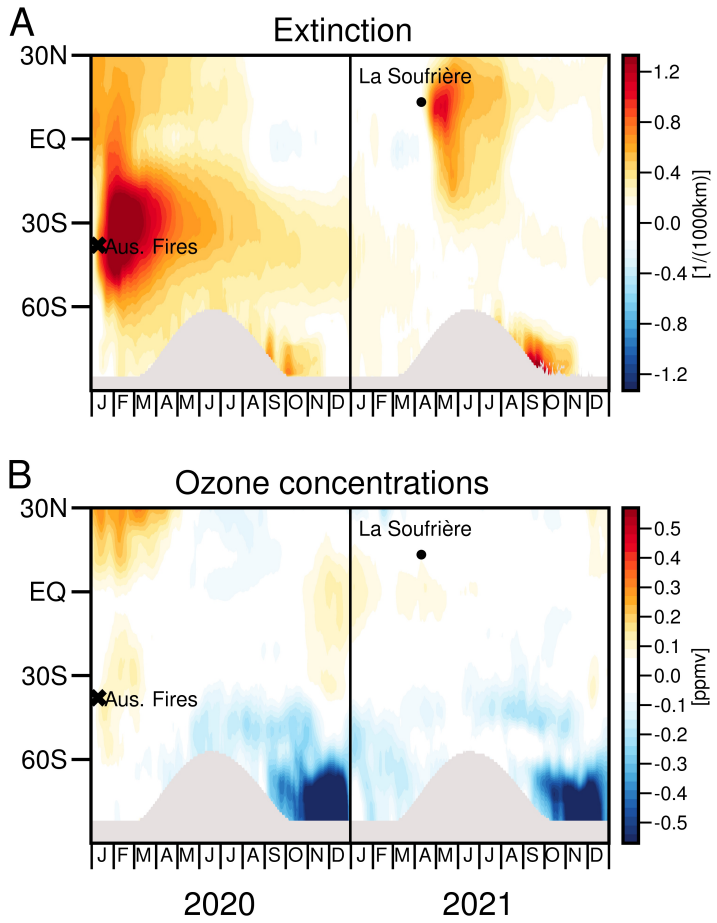

Figure 5.2: Time series of zonal-mean stratospheric aerosol extinction, and ozone concentrations anomalies during 2020-2021. Results are shown at the 70 hPa level. (A) Aerosol extinction (10^{-3} km^{-1}) and (B) ozone concentrations (ppmv) are derived from the OMPS-LP instrument. Anomalies are calculated with respect to the base period 2012-2019 (omitting 2015 due to the eruption of Calbuco). The results are smoothed with an 11-point (11-degree by 11-day) running mean filter.

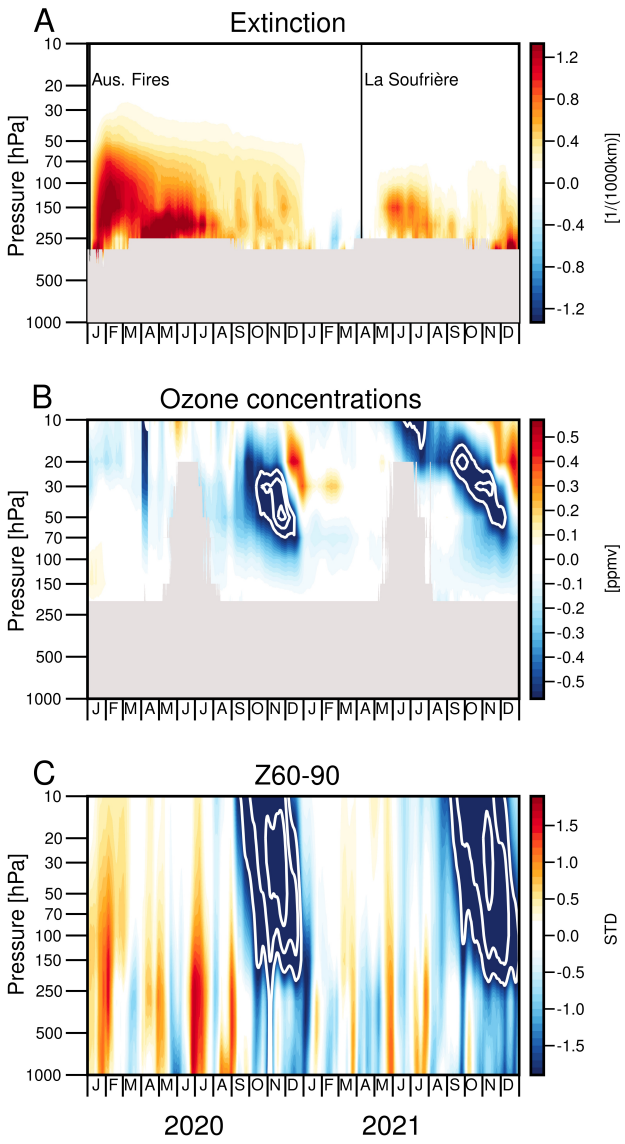

Figure 5.3: Time series of area-mean stratospheric aerosol extinction, ozone concentrations, and polar cap geopotential height anomalies. OMPS-LP aerosol extinction data (A, 10^{-3} km^{-1}) are averaged over 30-90 deg., ozone concentrations (B, ppmv) are averaged over 50-90 deg., and geopotential anomalies (C, normalized) are averaged over 60-90 deg. White contour lines are spaced at -0.6, -0.8, -1.0... ppmv for the ozone anomalies and $\pm$2, 3, 4... gpm for the geopotential anomalies. Black lines in the top panel mark the onset day of the Australian bushfires and the La Soufriere eruption. Regions within the troposphere or with a relatively small number (<200) of observations are masked out. The results are smoothed with an 11-day running mean filter. Anomalies are calculated with respect to the base period 2012-2019 (omitting 2015 due to the eruption of Calbuco).

geopotential consistent with cooling of the polar cap (Figure 5.1C). The decreases in polar geopotential height reflect a strengthening of the circumpolar vortex and thus positive anomalies in the southern annular mode at stratospheric levels. Consistent with our understanding of stratosphere/troposphere coupling [Baldwin and Dunkerton (2001); Thompson et al. (2005); Kidston et al. (2015); Fogt and Marshall (2020)], the anomalies in the stratospheric circumpolar flow extend to Earth's surface over a period of several weeks during both late 2020 and late 2021 (Figure 5.3C).

The extension of the circulation anomalies to tropospheric levels is clearly reflected in various changes in surface climate during late 2020 and 2021. Tropospheric geopotential height exhibited anomalies that resemble the high index polarity of the southern annular mode at tropospheric levels during both the 2020 and 2021 late austral spring/early summer seasons (Figure 5.4A, Figure 5.4B). The attendant changes in the surface circulation include various established regional climate impacts of the SAM, including anomalously westerlies over much of the Southern Ocean (Figure 5.4C, Figure 5.4D), anomalously cool conditions over the Antarctic plateau juxtaposed against warm conditions over the Antarctic peninsula [Figure 5.4C, Figure 5.4D; Thompson and Solomon (2002)], and anomalously cool conditions over much of Australia [Figs. Figure 5.5E, Figure 5.5F; Hendon et al. (2007)].

Figure 5.5 shows SH polar ozone anomalies plotted against SH extratropical-mean extinction (Fig. Figure 5.5A), the SH large-scale stratospheric circulation (Fig. Figure 5.5B), and the SH large-scale tropospheric circulation (Fig. Figure 5.5C). The scatter plots highlight both a) the robust nature of the linkages between the ozone hole and the SH circulation and b) the extraordinary nature of the 2020 and 2021 spring seasons. Note that the results in the left panel are shown for the OMPS period of record only while results in the middle and right panels are shown for the period starting 1979 (Methods).

The extinction anomalies during October-November of 2020 and 2021 (Fig. Figure 5.5A; blue and green dots) were exceeded only by those found after the eruption of the Calbuco volcano in 2015 (black dot). All three years were associated with extreme column ozone losses (left) and, in

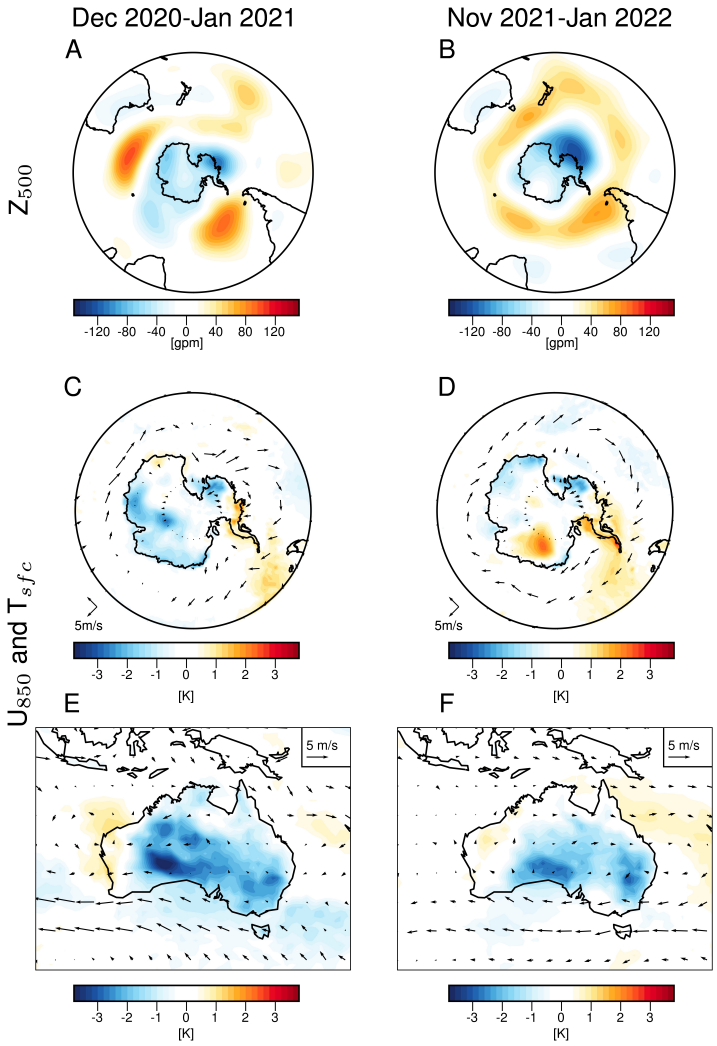

Figure 5.4: Surface climate anomalies during the 2020 and 2021 seasons. Monthly-mean anomalies in (A, B) geopotential height at 500 hPa (gpm) in the SH, (C, D, E, F) 2m-air temperature and the 850 hPa flow over (C, D) the Antarctic and (E, F) Australia. Results are shown for the periods of (A, C, E) December-January in 2020/21 and (B, D, F) November-January in 2021/22. Anomalies are calculated with respect to the base period 2012-2019 (omitting 2015 due to the eruption of Calbuco).

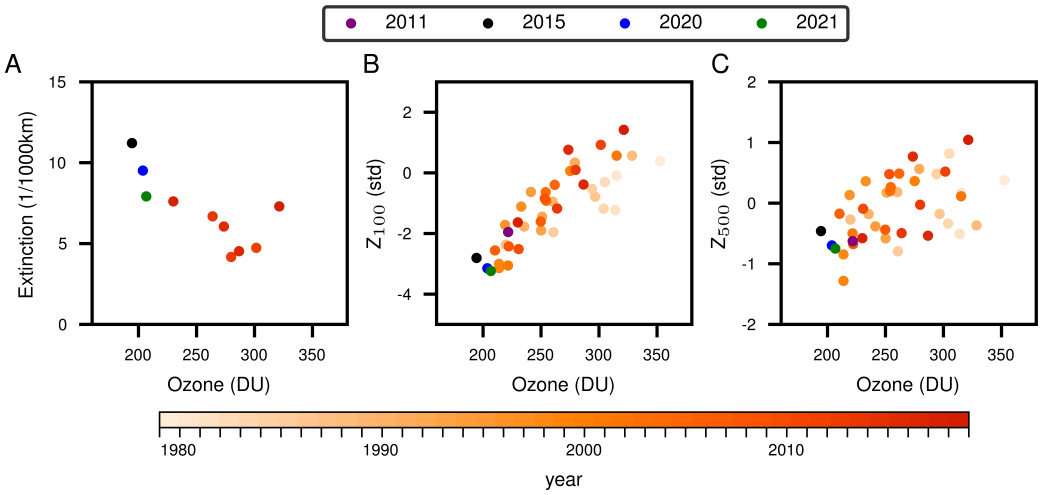

Figure 5.5: Scatter plots of total column ozone derived from the NASA Ozone Watch averaged over October to November (abscissa) versus (A) OMPS total column stratospheric aerosol extinction averaged over October to November, ERA5 polar cap geopotential height at (B) 100 hPa averaged over November to December and (C) 500 hPa averaged over November to January. The aerosol extinction data are averaged 30°-90°; ozone concentrations are averaged 63°-90°; and geopotential heights are averaged 60°-90°. Selected years with high aerosol loadings are indicated by the top colorbar; other years are indicated by the bottom colorbar. Anomalies are calculated with respect to the base period 2012-2019 (omitting 2015 due to the eruption of Calbuco).

turn, anomalously low polar stratospheric geopotential heights (middle). The outlier in Figure 5.5A, when ozone reached 325DU but extinction was not extremely low, was associated with the minor sudden stratospheric warming event in 2019 and is thus consistent with dynamic variability [Safieddine et al. (2020); Shen et al. (2020); Wargan et al. (2020)]. Other years marked by low polar ozone and stratospheric geopotential height anomalies include 2011, which coincides with the eruption of Cordon Caulle (purple dot in the middle panel), and the late 1990s, which coincide with the period of largest stratospheric chlorine loadings (dark orange dots). Apparently, extreme ozone losses and stratospheric geopotential height falls are associated with large chlorine loadings and/or enhanced particulate matter.

The years 2011, 2015, 2020 and 2021 also standout in terms of the attendant anomalies in the tropospheric circulation (right panel). All four years are associated with relatively low values of polar geopotential height at tropospheric levels during the late spring months indicative of the positive index polarity of the SAM.

Taken together, the scatter plots in Figure 5.5 reveal that both 2020 and 2021 stand out in terms of extinction (left ordinate), column ozone losses (abscissas), changes in the stratospheric circulation (middle ordinate), and changes in the tropospheric circulation (right ordinate). Note that the fits in all three panels are highly significant ($p < 0.01$) based on the t-statistic assuming one degree of freedom per calendar year, and that the associated variances explained by the linear fits are extremely high ($\sim$60%, 70% and 26% for panels a-c, respectively). The results are not sensitive to the latitudinal domain used to average the aerosol extinction values, i.e., similar results are derived using domains spanning 30°-90°S to 60°-90°S as shown in Figure 5.6.

Figure 5.5A is reproduced for different latitude bands. The specific choice of domain does not qualitatively affect the results. We now explicitly discuss this and the significance of the fits in the text.

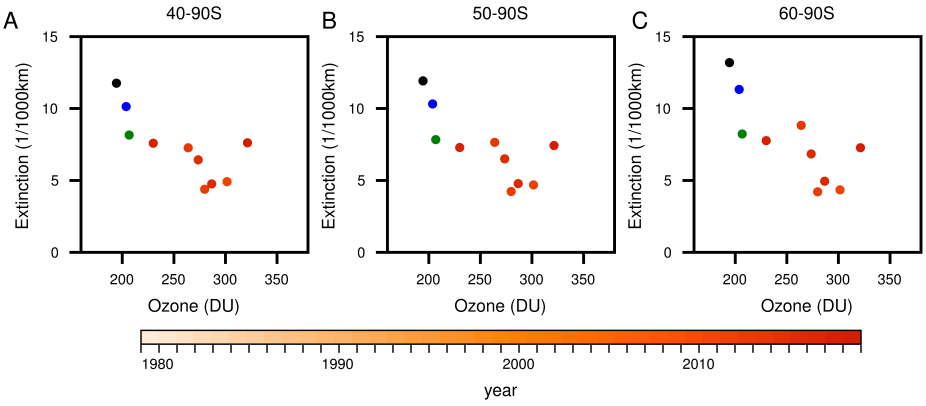

Figure 5.6: As in Figure 5.5A, but for different latitude bands to average the aerosol extinction values: (A) 40°-90°S, (B) 50°-90°S, and (C) 60°-90°S.

The uniqueness of the 2020 and 2021 seasons is further highlighted by the histograms in 5.7 The gray bars indicate histograms of daily values for all years in the record (Methods); the colored bars indicate histograms of daily values during late 2020 (left) and 2021 (right). The histograms are normalized such that the largest value on the ordinate axis is the same for 2020, 2021, and the historical periods; the number of days used to populate each histogram is indicated

on the figures. Again, it is clear that both late 2020 and 2021 were marked by unusually high values of extinction (top), low concentrations of polar ozone (second from top), and low pressures in the polar atmosphere consistent with a strengthening of the circumpolar westerly from the stratospheric levels to the surface (bottom two rows).

5.4 Conclusions

The 2020 and 2021 Antarctic ozone holes were among the largest on record despite the overall trend towards ozone recovery [https://ozonewatch.gsfc.nasa.gov; Stone et al. (2021)]. The results shown here reveal that both events were associated with changes in Southern Hemisphere surface climate consistent with the linkages between stratospheric ozone depletion and the large-scale SH circulation.

The results thus attest to the continuing role of stratospheric ozone depletion in surface climate change despite the onset of ozone recovery. They also indicate potentially important linkages between enhanced stratospheric particulate matter, ozone depletion, and changes in the hemispheric scale circulation from the stratosphere to the surface.

As discussed in the Introduction, the linkages between explosive volcanic eruptions and stratospheric ozone depletion are well established, whereas the linkages between wildfires and ozone depletion have only recently drawn comparable attention. Various mechanisms have been proposed. For examples: Yu et al. (2021) indicate significant simulated decreases in polar ozone following the 2020 Australian fires due to a combination of dynamical and chemical mechanisms. Solomon et al. (2022) show evidence for mid-latitude chemistry driving large observed nitrogen oxide changes following the fires. Santee et al. (2022) and Bernath et al. (2022) show remarkable changes in hydrochloric acid and chlorine nitrate at mid-latitudes after the Australian fires, but the chemical mechanism causing those changes has not yet been identified, nor has a clear link to polar chemistry been established. Wildfire soot may also contribute to dynamical changes in the strength of the vortex through changes in radiative heating, but this mechanism has yet to be explored.

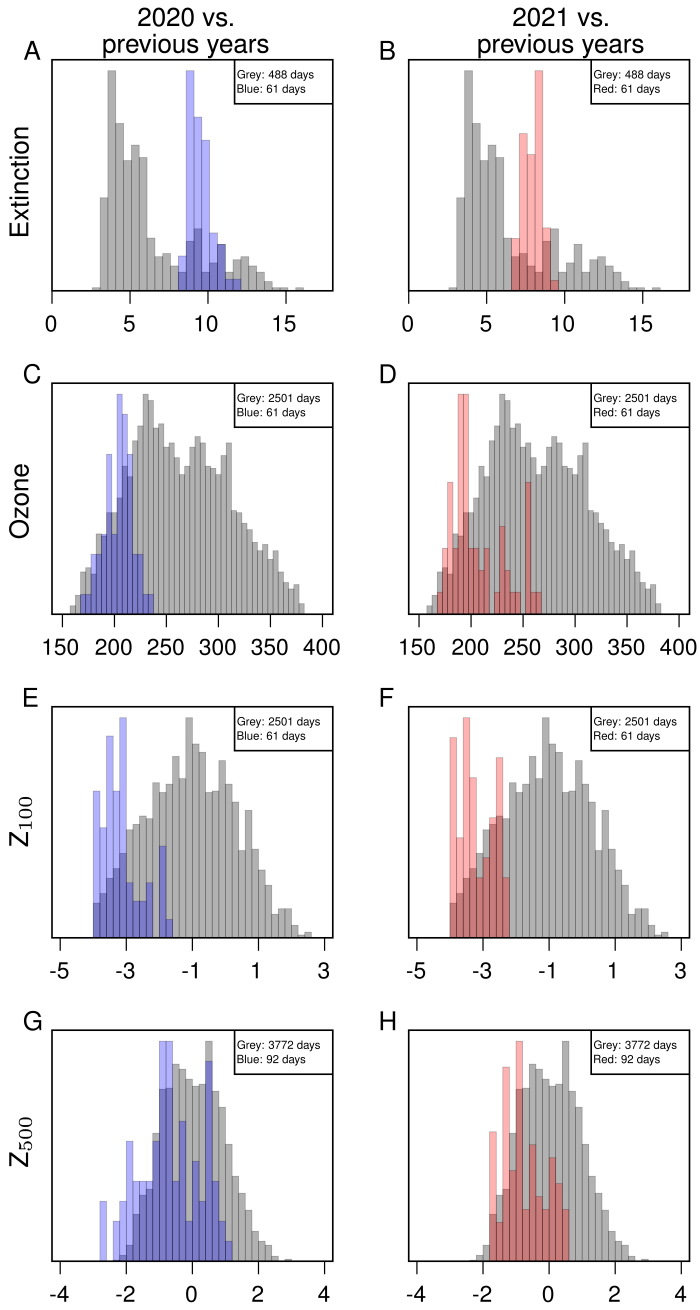

Figure 5.7: Histograms of daily-mean, OMPS total column stratospheric aerosol extinction, NASA Ozone Watch total column ozone, and ERA5 geopotential height anomalies at indicated levels. Results are derived from all days during Oct.-Nov. for aerosol extinction and total column ozone, Nov.-Dec. for 100hPa height, Nov.-Jan. for 500hPa height. The aerosol extinction data are averaged 30°-90°; ozone concentrations are averaged 63°-90°; and geopotential heights are averaged 60°-90°. Colored bars denote days during 2020 and 2021; gray bars denote days during all other years in the available record. The PDFs are normalized to the same height; the number of days used to construct the PDFs is indicated on the plots. Anomalies are calculated with respect to the base period 2012-2019 (omitting 2015 due to the eruption of Calbuco).

The number of high aerosol loading events in the OMPS-LP record is limited and thus internal variability cannot be completely ruled out. Nevertheless, the results shown here are strongly suggestive of causal linkages between stratospheric aerosol loadings and widespread changes in Southern Hemisphere surface climate. Notably, the results highlight the intriguing possibility that catastrophic wildfires may have a profound effect on the hemispheric-scale circulation long after the cessation of smoke production.

Chapter 6

Conclusion

This research investigated the role of interactions between different components of the Earth system such as oceanic variability, atmospheric chemistry, and atmospheric radiation and large-scale atmospheric circulation on climate variability. The research aimed to identify the physical processes that govern the climate interactions and to quantify their impacts on climate variability through 1) observational studies and 2) modeling studies based on a series of numerical experiments run on different configurations and hierarchies of climate models.

In chapter 2, we investigated the role of Sea Surface Temperature (SST) variability over the Kuroshio-Oyashio Extension (KOE) region on the large-scale atmospheric circulation over the North Pacific. Based on the analyses of two sets of climate simulations run with different types of atmosphere-ocean coupling, the results 1) support the interpretation of the observed lead/lag relationships between western North Pacific SST anomalies and the atmospheric circulation, and 2) provide numerical evidence that SST variability over the western North Pacific has a demonstrable effect on the large-scale atmospheric circulation throughout the North Pacific sector.

The air-sea interaction in the extratropics can play a crucial role in the variability of the extratropical jet and the Annular mode, both of which can lead to global climate impacts. Thus, understanding the air-sea interaction is an important research goal in order to 1) improve our understanding of the natural variability existing in the extratropical atmosphere and 2) reduce uncertainties in our future climate projections. The present study provides modeling evidence for the key role of extratropical SST variability on the large scale circulation in the North Pacific. The current findings of the study indicate that it would be of interest to further explore the role of nonlinear feedback from extratropical eddies on air-sea interaction, atmospheric circulation response in upper levels, and characteristics of air-sea interactions over different basins using different climate models.

In chapter 3, we assessed the role of 1) the moist lapse rate and 2) surface temperature variability as constraints on the amplitude and structure of temperature variability in the tropical atmosphere. We hypothesize that not only the mean temperature profile of the tropical atmosphere, but also the variability of the atmospheric temperature can be explained by the thermal structure of the tropical atmosphere following the moist adiabat. The moist lapse rate calculated from a single column radiative transfer model suggests that the internal variability of tropical atmospheric temperature exhibits a distinct maximum in the upper troposphere and that temperature variability is expected to increase under global warming. The changes in variance of the tropical atmospheric temperature in the coupled ESMs are explained by changes in moist adiabatic thermal structure in response to 1) increase in mean surface temperature or 2) changes in surface temperature variability. In both cases, Konrad reproduces the qualitatively similar features of the results from the ESM simulations. Hence the results herein indicate that the moist lapse rate is a robust constraint for tropical climate variability simulated by different model hierarchies.

Variations in upper tropical tropospheric temperatures play a critical role in the global climate. The upper troposphere temperature determines the net Outgoing Longwave Radiation (OLR) as well as the water vapor concentration entering the stratosphere, and thus can have significant impacts on climate sensitivity. These temperatures also determine the height of the tropopause along with the static stability of the troposphere which can largely affect large-scale atmospheric circulation. The results herein shows the key role of the moist lapse rate on the variability of upper tropical tropospheric temperature. Suggested topics for future study include assessing the role of upper tropical temperature variability in changes in other fields such as OLR, stratospheric water vapor, and tropical upwelling. Additional studies may extend to identifying factors contributing to the changes in surface temperature variability in future climate projections.

In chapter 4, we explored the impact of stratospheric chemistry-climate interactions on the temperature variability in the lower tropical stratosphere. The findings from the analyses of two sets of chemistry-climate simulations run with different types of chemistry-climate coupling suggest that the inclusion of coupled chemistry-climate interactions increases the internal

variability of temperature by a factor of two in the lower tropical stratosphere. Dynamically driven ozone-temperature feedback, which are only included in the coupled-chemistry simulation, is responsible for the increased temperature variability in the lower tropical stratosphere. The results also indicate that the climate models without coupled-chemistry underestimate the temperature variability in the lower tropical stratosphere as compared to the observations.

The temperature variability in the lower tropical stratosphere plays an outsized role in stratospheric climate. Most notably, it controls stratospheric water vapor concentration and Brewer-Dobson circulation, which in turn can have influences on the troposphere and surface climate. The findings from this study highlight the fundamental role of two-way feedbacks between the atmospheric circulation and chemistry in driving climate variability in the lower stratosphere. Suggested scope of future study includes investigating the role of chemistry-climate interactions on climate variability in other regions such as the Arctic surface and the tropical ocean.

In chapter 5, we continue to analyze the effects of coupled chemistry-climate interactions on the large-scale atmospheric based on two observational case studies of the Antarctic ozone holes of 2020 and 2021. We document that both the 2020 and 2021 Antarctic ozone holes were associated not only with large stratospheric aerosol loadings but also pronounced changes in the Southern Hemisphere circulation that extended from the stratosphere to the surface. The results provide suggestive evidence that injections of both wildfire smoke and volcanic emissions into the stratosphere can lead to hemispheric-scale changes in surface climate.

In future studies, it would be valuable to perform a series of numerical experiments with different configurations of chemistry-climate coupling to disentangle the complex aspects of the climate interactions. For example, comparisons of simulations done on specified-chemistry configuration with different aerosol or ozone forcing will reveal the radiative effects of the specific forcing driving atmospheric circulation anomalies. Similarly, comparisons of simulations done in specified-dynamics configuration with different background meteorology will elucidate

the influence of circulation anomalies on ozone chemistry. The findings will therefore improve our understanding of the impacts of wildfire and volcanic aerosols on the global climate.

This dissertation addresses four different research questions in climate science, focuses on discovering the key processes and interactions among different components of the Earth's system on climate variability using observational, modeling and theoretical studies. Many other aspects of the climate interactions, and the details of mechanism responsible for the changes in climate variability can be further investigated in future works.

References

Abrahamsen, E. P., and Coauthors, 2020: Antarctica and the southern ocean. *Bulletin of the American Meteorological Society*, **101 (8)**, S287–S320.

Alexander, M., 2010: Extratropical air-sea interaction, sea surface temperature variability, and the pacific decadal oscillation. *Climate dynamics: why does climate vary?*, **189**, 123–148.

Andrews, D. G., J. R. Holton, and C. B. Leovy, 1987: *Middle atmosphere dynamics*. 40, Academic press.

Andrews, T., and Coauthors, 2018: Accounting for changing temperature patterns increases historical estimates of climate sensitivity. *Geophysical Research Letters*, **45 (16)**, 8490–8499.

Ansmann, A., and Coauthors, 2021: Tropospheric and stratospheric wildfire smoke profiling with lidar: mass, surface area, ccn, and inp retrieval. *Atmospheric Chemistry and Physics*, **21 (12)**, 9779–9807.

Ansmann, A., and Coauthors, 2022: Ozone depletion in the arctic and antarctic stratosphere induced by wildfire smoke. *Atmospheric Chemistry and Physics*, **22 (17)**, 11 701–11 726.

Athanasiadis, P. J., S. Yeager, Y.-O. Kwon, A. Bellucci, D. W. Smith, and S. Tibaldi, 2020: Decadal predictability of north atlantic blocking and the nao. *NPJ Climate and Atmospheric Science*, **3 (1)**, 20.

Babu, S. R., L. S. P. Nguyen, G.-R. Sheu, S. M. Griffith, S. K. Pani, H.-Y. Huang, and N.-H. Lin, 2022: Long-range transport of la soufrière volcanic plume to the western north pacific: Influence on atmospheric mercury and aerosol properties. *Atmospheric Environment*, **268**, 118 806.

Baldwin, M. P., and T. J. Dunkerton, 2001: Stratospheric harbingers of anomalous weather regimes. *Science*, **294 (5542)**, 581–584.

Banerjee, D. S., G. Stephenson, and S. G. Das, 2020: Segmentation and analysis of mother machine data: Sam. *bioRxiv*, 2020–10.

Bao, J., B. Stevens, L. Kluft, and D. Jiménez-de-la Cuesta, 2021: Changes in the tropical lapse rate due to entrainment and their impact on climate sensitivity. *Geophysical Research Letters*, **48 (18)**, e2021GL094 969.

Barnston, A. G., and R. E. Livezey, 1987: Classification, seasonality and persistence of low-frequency atmospheric circulation patterns. *Monthly weather review*, **115 (6)**, 1083–1126.

Bernath, P., C. Boone, and J. Crouse, 2022: Wildfire smoke destroys stratospheric ozone. *Science*, **375 (6586)**, 1292–1295.

Birner, T., 2006: Fine-scale structure of the extratropical tropopause region. *Journal of Geophysical Research: Atmospheres*, **111 (D4)**.

Birner, T., and E. J. Charlesworth, 2017: On the relative importance of radiative and dynamical heating for tropical tropopause temperatures. *Journal of Geophysical Research: Atmospheres*, **122 (13)**, 6782–6797.

Bohren, C., and B. Albrecht, 1998: Atmospheric thermodynamics oxford university press. *New York*.

Bony, S., and K. A. Emanuel, 2005: On the role of moist processes in tropical intraseasonal variability: Cloud–radiation and moisture–convection feedbacks. *Journal of the atmospheric sciences*, **62 (8)**, 2770–2789.

Brasseur, G. P., and S. Solomon, 2005: *Dynamics and Transport*. Springer.

Bretherton, C. S., and D. S. Battisti, 2000: An interpretation of the results from atmospheric general circulation models forced by the time history of the observed sea surface temperature distribution. *Geophysical Research Letters*, **27 (6)**, 767–770.

Bretherton, C. S., M. Widmann, V. P. Dymnikov, J. M. Wallace, and I. Bladé, 1999: The effective number of spatial degrees of freedom of a time-varying field. *Journal of climate*, **12 (7)**, 1990–2009.

Brewer, A., 1949: Evidence for a world circulation provided by the measurements of helium and water vapour distribution in the stratosphere. *Quarterly Journal of the Royal Meteorological Society*, **75 (326)**, 351–363.

Butchart, N., and A. A. Scaife, 2001: Removal of chlorofluorocarbons by increased mass exchange between the stratosphere and troposphere in a changing climate. *Nature*, **410 (6830)**, 799–802.

Calvo, N., L. M. Polvani, and S. Solomon, 2015: On the surface impact of arctic stratospheric ozone extremes. *Environmental research letters*, **10 (9)**, 094 003.

Chang, P., and Coauthors, 2020: An unprecedented set of high-resolution earth system simulations for understanding multiscale interactions in climate variability and change. *Journal of Advances in Modeling Earth Systems*, **12 (12)**, e2020MS002 298.

Charlesworth, E. J., T. Birner, and J. R. Albers, 2019: Ozone transport-radiation feedbacks in the tropical tropopause layer. *Geophysical Research Letters*, **46 (23)**, 14 195–14 202.

Charney, J. G., 1963: A note on large-scale motions in the tropics. *Journal of the Atmospheric Sciences*, **20 (6)**, 607–609.

Chelton, D., M. Schlax, M. Freilich, and R. Milliff, 2004: Satellite radar measurements reveal short-scale features in the wind stress field over the world ocean. *Science*, **303 (5660)**, 978–983.

Chelton, D. B., and S.-P. Xie, 2010: Coupled ocean-atmosphere interaction at oceanic mesoscales. *Oceanography*, **23 (4)**, 52–69.

Chen, Z., M. DeLand, and P. K. Bhartia, 2016: A new algorithm for detecting cloud height using omps/lp measurements. *Atmospheric Measurement Techniques*, **9 (3)**, 1239–1246.

Ciasto, L. M., and D. W. Thompson, 2004: North atlantic atmosphere–ocean interaction on intraseasonal time scales. *Journal of climate*, **17 (8)**, 1617–1621.

Coupe, J., and A. Robock, 2021: The influence of stratospheric soot and sulfate aerosols on the northern hemisphere wintertime atmospheric circulation. *Journal of Geophysical Research: Atmospheres*, **126 (11)**, e2020JD034 513.

Czaja, A., and C. Frankignoul, 2002: Observed impact of atlantic sst anomalies on the north atlantic oscillation. *Journal of Climate*, **15 (6)**, 606–623.

Czaja, A., C. Frankignoul, S. Minobe, and B. Vannière, 2019: Simulating the midlatitude atmospheric circulation: what might we gain from high-resolution modeling of air-sea interactions? *Current Climate Change reports*, **5**, 390–406.

Dacie, S., and Coauthors, 2019: A 1d rce study of factors affecting the tropical tropopause layer and surface climate. *Journal of Climate*, **32 (20)**, 6769–6782.

DallaSanta, K., E. P. Gerber, and M. Toohey, 2019: The circulation response to volcanic eruptions: The key roles of stratospheric warming and eddy interactions. *Journal of Climate*, **32 (4)**, 1101–1120.

Davis, R. E., 1976: Predictability of sea surface temperature and sea level pressure anomalies over the north pacific ocean. *Journal of Physical Oceanography*, **6 (3)**, 249–266.

de F. Forster, P. M., and K. P. Shine, 1997: Radiative forcing and temperature trends from stratospheric ozone changes. *Journal of Geophysical Research: Atmospheres*, **102 (D9)**, 10 841–10 855.

de F. Forster, P. M., and K. P. Shine, 1999: Stratospheric water vapour changes as a possible contributor to observed stratospheric cooling. *Geophysical research letters*, **26 (21)**, 3309–3312.

Deser, C., M. A. Alexander, and M. S. Timlin, 2003: Understanding the persistence of sea surface temperature anomalies in midlatitudes. *Journal of Climate*, **16 (1)**, 57–72.

Deser, C., A. Phillips, V. Bourdette, and H. Teng, 2012: Uncertainty in climate change projections: the role of internal variability. *Climate dynamics*, **38**, 527–546.

Deser, C., and M. S. Timlin, 1997: Atmosphere–ocean interaction on weekly timescales in the north atlantic and pacific. *Journal of climate*, **10 (3)**, 393–408.

Deser, C., and Coauthors, 2020: Insights from earth system model initial-condition large ensembles and future prospects. *Nature Climate Change*, **10 (4)**, 277–286.

Emanuel, K., 2005: Increasing destructiveness of tropical cyclones over the past 30 years. *Nature*, **436 (7051)**, 686–688.

Eyring, V., and Coauthors, 2010: Multi-model assessment of stratospheric ozone return dates and ozone recovery in ccmval-2 models. *Atmospheric Chemistry and Physics*, **10 (19)**, 9451–9472.

Feldl, N., S. Po-Chedley, H. K. Singh, S. Hay, and P. J. Kushner, 2020: Sea ice and atmospheric circulation shape the high-latitude lapse rate feedback. *NPJ climate and atmospheric science*, **3 (1)**, 41.

Feldstein, S. B., 2000: The timescale, power spectra, and climate noise properties of teleconnection patterns. *Journal of Climate*, **13 (24)**, 4430–4440.

Fels, S., J. Mahlman, M. Schwarzkopf, and R. Sinclair, 1980: Stratospheric sensitivity to perturbations in ozone and carbon dioxide- radiative and dynamical response. *Journal of the Atmospheric Sciences*, **37 (10)**, 2265–2297.

Fermepin, S., and S. Bony, 2014: Influence of low-cloud radiative effects on tropical circulation and precipitation. *Journal of Advances in Modeling Earth Systems*, **6 (3)**, 513–526.

Fogt, R. L., and G. J. Marshall, 2020: The southern annular mode: variability, trends, and climate impacts across the southern hemisphere. *Wiley Interdisciplinary Reviews: Climate Change*, **11 (4)**, e652.

Forster, P. M. d. F., and K. Shine, 2002: Assessing the climate impact of trends in stratospheric water vapor. *Geophysical research letters*, **29 (6)**, 10–1.

Frankignoul, C., 1985: Sea surface temperature anomalies, planetary waves, and air-sea feedback in the middle latitudes. *Reviews of geophysics*, **23 (4)**, 357–390.

Frankignoul, C., and K. Hasselmann, 1977: Stochastic climate models, part ii application to sea-surface temperature anomalies and thermocline variability. *Tellus*, **29 (4)**, 289–305.

Frankignoul, C., and N. Sennéchael, 2007: Observed influence of north pacific sst anomalies on the atmospheric circulation. *Journal of Climate*, **20 (3)**, 592–606.

Frankignoul, C., N. Sennéchael, Y.-O. Kwon, and M. A. Alexander, 2011: Influence of the meridional shifts of the kuroshio and the oyashio extensions on the atmospheric circulation. *Journal of Climate*, **24 (3)**, 762–777.

Fueglistaler, S., A. Dessler, T. Dunkerton, I. Folkins, Q. Fu, and P. W. Mote, 2009: Tropical tropopause layer. *Reviews of Geophysics*, **47 (1)**.

Fueglistaler, S., P. Haynes, and P. Forster, 2011: The annual cycle in lower stratospheric temperatures revisited. *Atmospheric Chemistry and Physics*, **11 (8)**, 3701–3711.

Fusco, A. C., and M. L. Salby, 1999: Interannual variations of total ozone and their relationship to variations of planetary wave activity. *Journal of climate*, **12 (6)**, 1619–1629.

Garcia, R. R., and W. J. Randel, 2008: Acceleration of the brewer–dobson circulation due to increases in greenhouse gases. *Journal of the Atmospheric Sciences*, **65 (8)**, 2731–2739.

Garcia, R. R., and S. Solomon, 1994: A new numerical model of the middle atmosphere: 2. ozone and related species. *Journal of Geophysical Research: Atmospheres*, **99 (D6)**, 12 937–12 951.

Gilford, D. M., and S. Solomon, 2017: Radiative effects of stratospheric seasonal cycles in the tropical upper troposphere and lower stratosphere. *Journal of Climate*, **30 (8)**, 2769–2783.

Gillett, N. P., and D. W. Thompson, 2003: Simulation of recent southern hemisphere climate change. *Science*, **302 (5643)**, 273–275.

Grise, K. M., and D. W. Thompson, 2013: On the signatures of equatorial and extratropical wave forcing in tropical tropopause layer temperatures. *Journal of the atmospheric sciences*, **70 (4)**, 1084–1102.

Haase, S., and K. Matthes, 2019: The importance of interactive chemistry for stratosphere–troposphere coupling. *Atmospheric Chemistry and Physics*, **19 (5)**, 3417–3432.

Hall, N. M., J. Derome, and H. Lin, 2001: The extratropical signal generated by a midlatitude sst anomaly. part i: Sensitivity at equilibrium. *Journal of Climate*, **14 (9)**, 2035–2053.

Hansen, J., A. Lacis, D. Rind, G. Russell, P. Stone, I. Fung, R. Ruedy, and J. Lerner, 1984: Climate sensitivity: Analysis of feedback mechanisms. *Climate processes and climate sensitivity*, **29**, 130–163.

Hartmann, D. L., and K. Larson, 2002: An important constraint on tropical cloud-climate feedback. *Geophysical research letters*, **29 (20)**, 12–1.

Hassler, B., J. Daniel, B. Johnson, S. Solomon, and S. Oltmans, 2011: An assessment of changing ozone loss rates at south pole: Twenty-five years of ozonesonde measurements. *Journal of Geophysical Research: Atmospheres*, **116 (D22)**.

Held, I. M., R. S. Hemler, and V. Ramaswamy, 1993: Radiative-convective equilibrium with explicit two-dimensional moist convection. *Journal of Atmospheric Sciences*, **50 (23)**, 3909–3927.

Held, I. M., and B. J. Soden, 2000: Water vapor feedback and global warming. *Annual review of energy and the environment*, **25 (1)**, 441–475.

Hendon, H. H., D. W. Thompson, and M. C. Wheeler, 2007: Australian rainfall and surface temperature variations associated with the southern hemisphere annular mode. *Journal of Climate*, **20 (11)**, 2452–2467.

Hersbach, H., and Coauthors, 2020: The era5 global reanalysis. *Quarterly Journal of the Royal Meteorological Society*, **146 (730)**, 1999–2049.

Hirsch, E., and I. Koren, 2021: Record-breaking aerosol levels explained by smoke injection into the stratosphere. *Science*, **371 (6535)**, 1269–1274.

Hitchcock, P., T. G. Shepherd, and S. Yoden, 2010: On the approximation of local and linear radiative damping in the middle atmosphere. *Journal of the atmospheric sciences*, **67 (6)**, 2070–2085.

Holton, J. R., and W. M. Wehrbein, 1980: A numerical model of the zonal mean circulation of the middle atmosphere. *pure and applied geophysics*, **118**, 284–306.

Hoskins, B. J., and D. J. Karoly, 1981: The steady linear response of a spherical atmosphere to thermal and orographic forcing. *Journal of the atmospheric sciences*, **38 (6)**, 1179–1196.

Hurrell, J. W., J. J. Hack, D. Shea, J. M. Caron, and J. Rosinski, 2008: A new sea surface temperature and sea ice boundary dataset for the community atmosphere model. *Journal of Climate*, **21 (19)**, 5145–5153.

Hurrell, J. W., and Coauthors, 2013: The community earth system model: a framework for collaborative research. *Bulletin of the American Meteorological Society*, **94 (9)**, 1339–1360.

Ivy, D. J., S. Solomon, N. Calvo, and D. W. Thompson, 2017: Observed connections of arctic stratospheric ozone extremes to northern hemisphere surface climate. *Environmental Research Letters*, **12 (2)**, 024 004.

Jeffrey, S., L. Rotstayn, M. Collier, S. Dravitzki, C. Hamalainen, C. Moeseneder, K. Wong, and J. Syktus, 2013: Australia's cmip5 submission usingthe csiro-mk3. 6 model. *Australian Meteorological and Oceanographic Journal*, **63 (1)**, 1–13.

Johnson, Z. F., Y. Chikamoto, S.-Y. S. Wang, M. J. McPhaden, and T. Mochizuki, 2020: Pacific decadal oscillation remotely forced by the equatorial pacific and the atlantic oceans. *Climate Dynamics*, **55**, 789–811.

Kay, J. E., and Coauthors, 2015: The community earth system model (cesm) large ensemble project: A community resource for studying climate change in the presence of internal climate variability. *Bulletin of the American Meteorological Society*, **96 (8)**, 1333–1349.

Keil, P., H. Schmidt, B. Stevens, and J. Bao, 2021: Variations of tropical lapse rates in climate models and their implications for upper-tropospheric warming. *Journal of Climate*, **34 (24)**, 9747–9761.

Khaykin, S., and Coauthors, 2020: The 2019/20 australian wildfires generated a persistent smoke-charged vortex rising up to 35 km altitude. *Communications Earth & Environment*, **1 (1)**, 22.

Kidston, J., A. A. Scaife, S. C. Hardiman, D. M. Mitchell, N. Butchart, M. P. Baldwin, and L. J. Gray, 2015: Stratospheric influence on tropospheric jet streams, storm tracks and surface weather. *Nature Geoscience*, **8 (6)**, 433–440.

Kiehl, J., and S. Solomon, 1986: On the radiative balance of the stratosphere. *Journal of Atmospheric Sciences*, **43 (14)**, 1525–1534.

Kirchmeier-Young, M. C., F. W. Zwiers, and N. P. Gillett, 2017: Attribution of extreme events in arctic sea ice extent. *Journal of Climate*, **30 (2)**, 553–571.

Kluft, L., S. Dacie, S. A. Buehler, H. Schmidt, and B. Stevens, 2019: Re-examining the first climate models: Climate sensitivity of a modern radiative–convective equilibrium model. *Journal of Climate*, **32 (23)**, 8111–8125.

Kodera, K., 1994: Influence of volcanic eruptions on the troposphere through stratospheric dynamical processes in the northern hemisphere winter. *Journal of Geophysical Research: Atmospheres*, **99 (D1)**, 1273–1282.

Kooy, B. K., 2015: Stanford encyclopedia of philosophy–http://plato. stanford. edu. *Reference Reviews*, **29 (8)**, 14–16.

Kosaka, Y., and S.-P. Xie, 2013: Recent global-warming hiatus tied to equatorial pacific surface cooling. *Nature*, **501 (7467)**, 403–407.

Kramarova, N., and Coauthors, 2014: Measuring the antarctic ozone hole with the new ozone mapping and profiler suite (omps). *Atmospheric Chemistry and Physics*, **14 (5)**, 2353–2361.

Kuang, Z., and C. S. Bretherton, 2004: Convective influence on the heat balance of the tropical tropopause layer: A cloud-resolving model study. *Journal of the atmospheric sciences*, **61 (23)**, 2919–2927.

Kuang, Z., and D. L. Hartmann, 2007: Testing the fixed anvil temperature hypothesis in a cloud-resolving model. *Journal of Climate*, **20 (10)**, 2051–2057.

Kushner, P. J., I. M. Held, and T. L. Delworth, 2001: Southern hemisphere atmospheric circulation response to global warming. *Journal of Climate*, **14 (10)**, 2238–2249.

Kushnir, Y., W. Robinson, I. Bladé, N. Hall, S. Peng, and R. Sutton, 2002: Atmospheric gcm response to extratropical sst anomalies: Synthesis and evaluation. *Journal of Climate*, **15 (16)**, 2233–2256.

Kwon, Y.-O., M. A. Alexander, N. A. Bond, C. Frankignoul, H. Nakamura, B. Qiu, and L. A. Thompson, 2010: Role of the gulf stream and kuroshio–oyashio systems in large-scale atmosphere–ocean interaction: A review. *Journal of Climate*, **23 (12)**, 3249–3281.

Kwon, Y.-O., C. Deser, and C. Cassou, 2011: Coupled atmosphere–mixed layer ocean response to ocean heat flux convergence along the kuroshio current extension. *Climate dynamics*, **36**, 2295–2312.

Kwon, Y.-O., and T. M. Joyce, 2013: Northern hemisphere winter atmospheric transient eddy heat fluxes and the gulf stream and kuroshio–oyashio extension variability. *Journal of Climate*, **26 (24)**, 9839–9859.

Kwon, Y.-O., H. Seo, C. C. Ummenhofer, and T. M. Joyce, 2020: Impact of multidecadal variability in atlantic sst on winter atmospheric blocking. *Journal of Climate*, **33 (3)**, 867–892.

Langematz, U., M. Tully, N. Calvo, M. Dameris, J. de Laat, A. R. Klekociuk, R. Müller, and P. Young, 2018: Polar stratospheric ozone: Past, present, and future, chapter 4 in wmo scientific assessment of ozone depletion (2018). *UNEP/WMO Scientific Assessment of Ozone Depletion: 2018 (Report)*, **58**.

Lau, N.-C., and M. J. Nath, 1994: A modeling study of the relative roles of tropical and extratropical sst anomalies in the variability of the global atmosphere-ocean system. *Journal of Climate*, **7 (8)**, 1184–1207.

Lee, M.-I., I.-S. Kang, J.-K. Kim, and B. E. Mapes, 2001: Influence of cloud-radiation interaction on simulating tropical intraseasonal oscillation with an atmospheric general circulation model. *Journal of Geophysical Research: Atmospheres*, **106 (D13)**, 14 219–14 233.

Li, Y., D. W. Thompson, and S. Bony, 2015: The influence of atmospheric cloud radiative effects on the large-scale atmospheric circulation. *Journal of Climate*, **28 (18)**, 7263–7278.

Ma, X., P. Chang, R. Saravanan, R. Montuoro, H. Nakamura, D. Wu, X. Lin, and L. Wu, 2017: Importance of resolving kuroshio front and eddy influence in simulating the north pacific storm track. *Journal of Climate*, **30 (5)**, 1861–1880.

Ma, X., and Coauthors, 2015: Distant influence of kuroshio eddies on north pacific weather patterns? *Scientific reports*, **5 (1)**, 17 785.

Madden, R. A., 1976: Estimates of the natural variability of time-averaged sea-level pressure. *Monthly Weather Review*, **104 (7)**, 942–952.

Magaritz-Ronen, L., and S. Raveh-Rubin, 2021: Wildfire smoke highlights troposphere-to-stratosphere pathway. *Geophysical research letters*, **48 (23)**, e2021GL095 848.

Manabe, S., and R. J. Stouffer, 1980: Sensitivity of a global climate model to an increase of co2 concentration in the atmosphere. *Journal of Geophysical Research: Oceans*, **85 (C10)**, 5529–5554.

Manabe, S., and R. F. Strickler, 1964: Thermal equilibrium of the atmosphere with a convective adjustment. *Journal of the Atmospheric Sciences*, **21 (4)**, 361–385.

Manabe, S., and R. T. Wetherald, 1967: Thermal equilibrium of the atmosphere with a given distribution of relative humidity.

Marsh, D. R., M. J. Mills, D. E. Kinnison, J.-F. Lamarque, N. Calvo, and L. M. Polvani, 2013: Climate change from 1850 to 2005 simulated in cesm1 (waccm). *Journal of climate*, **26 (19)**, 7372–7391.

Ming, A., A. C. Maycock, P. Hitchcock, and P. Haynes, 2017: The radiative role of ozone and water vapour in the annual temperature cycle in the tropical tropopause layer. *Atmospheric Chemistry and Physics*, **17 (9)**, 5677–5701.

Minobe, S., A. Kuwano-Yoshida, N. Komori, S.-P. Xie, and R. J. Small, 2008: Influence of the gulf stream on the troposphere. *Nature*, **452 (7184)**, 206–209.

Minobe, S., M. Miyashita, A. Kuwano-Yoshida, H. Tokinaga, and S.-P. Xie, 2010: Atmospheric response to the gulf stream: Seasonal variations. *Journal of Climate*, **23 (13)**, 3699–3719.

Minschwaner, K., and A. E. Dessler, 2004: Water vapor feedback in the tropical upper troposphere: Model results and observations. *Journal of Climate*, **17 (6)**, 1272–1282.

Miyawaki, O., Z. Tan, T. A. Shaw, and M. F. Jansen, 2020: Quantifying key mechanisms that contribute to the deviation of the tropical warming profile from a moist adiabat. *Geophysical Research Letters*, **47 (20)**, e2020GL089 136.

Mlawer, E. J., S. J. Taubman, P. D. Brown, M. J. Iacono, and S. A. Clough, 1997: Radiative transfer for inhomogeneous atmospheres: Rrtm, a validated correlated-k model for the longwave. *Journal of Geophysical Research: Atmospheres*, **102 (D14)**, 16 663–16 682.

Murray, D., and Coauthors, 2020: Facility for weather and climate assessments (facts): a community resource for assessing weather and climate variability. *Bulletin of the American Meteorological Society*, **101 (7)**, E1214–E1224.

Nakamura, H., T. Sampe, A. Goto, W. Ohfuchi, and S.-P. Xie, 2008: On the importance of midlatitude oceanic frontal zones for the mean state and dominant variability in the tropospheric circulation. *Geophysical Research Letters*, **35 (15)**.

Nakamura, H., T. Sampe, Y. Tanimoto, and A. Shimpo, 2004: Observed associations among storm tracks, jet streams and midlatitude oceanic fronts. *Earth's Climate: The Ocean–Atmosphere Interaction, Geophys. Monogr*, **147**, 329–345.

Neale, R. B., and Coauthors, 2010: Description of the ncar community atmosphere model (cam 5.0). *NCAR Tech. Note NCAR/TN-486+ STR*, **1 (1)**, 1–12.

Newman, P. A., and J. E. Rosenfield, 1997: Stratospheric thermal damping times. *Geophysical research letters*, **24 (4)**, 433–436.

Norton, W., 2006: Tropical wave driving of the annual cycle in tropical tropopause temperatures. part ii: Model results. *Journal of the atmospheric sciences*, **63 (5)**, 1420–1431.

Ohneiser, K., and Coauthors, 2020: Smoke of extreme australian bushfires observed in the stratosphere over punta arenas, chile, in january 2020: optical thickness, lidar ratios, and depolarization ratios at 355 and 532 nm. *Atmospheric Chemistry and Physics*, **20 (13)**, 8003–8015.

O'Reilly, C. H., and A. Czaja, 2015: The response of the pacific storm track and atmospheric circulation to kuroshio extension variability. *Quarterly Journal of the Royal Meteorological Society*, **141 (686)**, 52–66.

O'Reilly, C. H., S. Minobe, A. Kuwano-Yoshida, and T. Woollings, 2017: The gulf stream influence on wintertime north atlantic jet variability. *Quarterly Journal of the Royal Meteorological Society*, **143 (702)**, 173–183.

O'Neill, L. W., D. B. Chelton, S. K. Esbensen, and F. J. Wentz, 2005: High-resolution satellite measurements of the atmospheric boundary layer response to sst variations along the agulhas return current. *Journal of Climate*, **18 (14)**, 2706–2723.

Peng, S., and W. A. Robinson, 2001: Relationships between atmospheric internal variability and the responses to an extratropical sst anomaly. *Journal of climate*, **14 (13)**, 2943–2959.

Peng, S., W. A. Robinson, and M. P. Hoerling, 1997: The modeled atmospheric response to midlatitude sst anomalies and its dependence on background circulation states. *Journal of Climate*, **10 (5)**, 971–987.

Peng, S., and J. S. Whitaker, 1999: Mechanisms determining the atmospheric response to midlatitude sst anomalies. *Journal of climate*, **12 (5)**, 1393–1408.

Peterson, D. A., and Coauthors, 2021: Australia's black summer pyrocumulonimbus super outbreak reveals potential for increasingly extreme stratospheric smoke events. *NPJ climate and atmospheric science*, **4 (1)**, 38.

Petty, G. W., 2006: *A first course in atmospheric radiation*. Sundog Pub.

Philander, S. G. H., 1983: El nino southern oscillation phenomena. *Nature*, **302 (5906)**, 295–301.

Pierrehumbert, R. T., 1995: Thermostats, radiator fins, and the local runaway greenhouse. *Journal of the atmospheric sciences*, **52 (10)**, 1784–1806.

Plass, G. N., 1956: The influence of the 9.6 micron ozone band on the atmospheric infra-red cooling rate. *Quarterly Journal of the Royal Meteorological Society*, **82 (351)**, 30–44.

Polvani, L. M., D. W. Waugh, G. J. Correa, and S.-W. Son, 2011: Stratospheric ozone depletion: The main driver of twentieth-century atmospheric circulation changes in the southern hemisphere. *Journal of Climate*, **24 (3)**, 795–812.

Polvani, L. M., and Coauthors, 2019: Large impacts, past and future, of ozone-depleting substances on brewer-dobson circulation trends: A multimodel assessment. *Journal of Geophysical Research: Atmospheres*, **124 (13)**, 6669–6680.

Popke, D., B. Stevens, and A. Voigt, 2013: Climate and climate change in a radiative-convective equilibrium version of echam6. *Journal of Advances in Modeling Earth Systems*, **5 (1)**, 1–14.

Portmann, R., S. Solomon, R. Garcia, L. Thomason, L. Poole, and M. McCormick, 1996: Role of aerosol variations in anthropogenic ozone depletion in the polar regions. *Journal of Geophysical Research: Atmospheres*, **101 (D17)**, 22 991–23 006.

Ramaswamy, V., and Coauthors, 2001: Stratospheric temperature trends: Observations and model simulations. *Reviews of Geophysics*, **39 (1)**, 71–122.

Randall, D. A., D. A. Dazlich, T. G. Corsetti, and Coauthors, 1989: Interactions among radiation, convection, and large-scale dynamics in a general circulation model. *Journal of the Atmospheric sciences*, **46 (13)**, 1943–1970.

Randel, W. J., R. R. Garcia, and F. Wu, 2002: Time-dependent upwelling in the tropical lower stratosphere estimated from the zonal-mean momentum budget. *Journal of the Atmospheric Sciences*, **59 (13)**, 2141–2152.

Randel, W. J., and F. Wu, 1999: Cooling of the arctic and antarctic polar stratospheres due to ozone depletion. *Journal of Climate*, **12 (5)**, 1467–1479.

Randel, W. J., F. Wu, and P. Forster, 2007: The extratropical tropopause inversion layer: Global observations with gps data, and a radiative forcing mechanism. *Journal of the Atmospheric Sciences*, **64 (12)**, 4489–4496.

Raymond, D. J., 2001: A new model of the madden–julian oscillation. *Journal of the atmospheric sciences*, **58 (18)**, 2807–2819.

Reed, K. A., B. Medeiros, J. T. Bacmeister, and P. H. Lauritzen, 2015: Global radiative–convective equilibrium in the community atmosphere model, version 5. *Journal of the Atmospheric Sciences*, **72 (5)**, 2183–2197.

Révelard, A., C. Frankignoul, N. Sennéchael, Y.-O. Kwon, and B. Qiu, 2016: Influence of the decadal variability of the kuroshio extension on the atmospheric circulation in the cold season. *Journal of Climate*, **29 (6)**, 2123–2144.

Rieder, H. E., G. Chiodo, J. Fritzer, C. Wienerroither, and L. M. Polvani, 2019: Is interactive ozone chemistry important to represent polar cap stratospheric temperature variability in earth-system models? *Environmental Research Letters*, **14 (4)**, 044 026.

Rieger, L., W. Randel, A. Bourassa, and S. Solomon, 2021: Stratospheric temperature and ozone anomalies associated with the 2020 australian new year fires. *Geophysical Research Letters*, **48 (24)**, e2021GL095 898.

Robock, A., 2000: Volcanic eruptions and climate. *Reviews of geophysics*, **38 (2)**, 191–219.

Robock, A., and J. Mao, 1995: The volcanic signal in surface temperature observations. *Journal of Climate*, **8 (5)**, 1086–1103.

Rodgers, K. B., J. Lin, and T. L. Frölicher, 2015: Emergence of multiple ocean ecosystem drivers in a large ensemble suite with an earth system model. *Biogeosciences*, **12 (11)**, 3301–3320.

Safieddine, S., and Coauthors, 2020: Antarctic ozone enhancement during the 2019 sudden stratospheric warming event. *Geophysical Research Letters*, **47 (14)**, e2020GL087 810.

Santee, M., and Coauthors, 2022: Prolonged and pervasive perturbations in the composition of the southern hemisphere midlatitude lower stratosphere from the australian new year's fires. *Geophysical Research Letters*, **49 (4)**, e2021GL096 270.

Santer, B. D., and Coauthors, 2003: Contributions of anthropogenic and natural forcing to recent tropopause height changes. *science*, **301 (5632)**, 479–483.

Saulière, J., D. J. Brayshaw, B. Hoskins, and M. Blackburn, 2012: Further investigation of the impact of idealized continents and sst distributions on the northern hemisphere storm tracks. *Journal of the atmospheric sciences*, **69 (3)**, 840–856.

Schneider, E., and J. Kinter, 1994: An examination of internally generated variability in long climate simulations. *Climate Dynamics*, **10**, 181–204.

Schwartz, M. J., and Coauthors, 2020: Australian new year's pyrocb impact on stratospheric composition. *Geophysical Research Letters*, **47 (24)**, e2020GL090 831.

Screen, J. A., and I. Simmonds, 2010: The central role of diminishing sea ice in recent arctic temperature amplification. *Nature*, **464 (7293)**, 1334–1337.

Shen, X., L. Wang, and S. Osprey, 2020: Tropospheric forcing of the 2019 antarctic sudden stratospheric warming. *Geophysical Research Letters*, **47 (20)**, e2020GL089 343.

Sherwood, S. C., and A. E. Dessler, 2000: On the control of stratospheric humidity. *Geophysical research letters*, **27 (16)**, 2513–2516.

Sherwood, S. C., V. Ramanathan, T. P. Barnett, M. K. Tyree, and E. Roeckner, 1994: Response of an atmospheric general circulation model to radiative forcing of tropical clouds. *Journal of Geophysical Research: Atmospheres*, **99 (D10)**, 20 829–20 845.

Shindell, D. T., and G. A. Schmidt, 2004: Southern hemisphere climate response to ozone changes and greenhouse gas increases. *Geophysical Research Letters*, **31 (18)**.

Shindell, D. T., S. Wong, and D. Rind, 1997: Interannual variability of the antarctic ozone hole in a gcm. part i: The influence of tropospheric wave variability. *Journal of the atmospheric sciences*, **54 (18)**, 2308–2319.

Shine, K. P., and Coauthors, 2003: A comparison of model-simulated trends in stratospheric temperatures. *Quarterly Journal of the Royal Meteorological Society: A journal of the atmospheric sciences, applied meteorology and physical oceanography*, **129 (590)**, 1565–1588.

Simmons, A., 2006: Era-interim: New ecmwf reanalysis products from 1989 onwards. *ECMWF newsletter*, **110**, 25–36.

Simpson, I. R., S. G. Yeager, K. A. McKinnon, and C. Deser, 2019: Decadal predictability of late winter precipitation in western europe through an ocean–jet stream connection. *Nature Geoscience*, **12 (8)**, 613–619.

Siqueira, L., and B. P. Kirtman, 2016: Atlantic near-term climate variability and the role of a resolved gulf stream. *Geophysical Research Letters*, **43 (8)**, 3964–3972.

Slingo, A., and J. Slingo, 1988: The response of a general circulation model to cloud longwave radiative forcing. i: Introduction and initial experiments. *Quarterly Journal of the Royal Meteorological Society*, **114 (482)**, 1027–1062.

Small, R. J., F. O. Bryan, S. P. Bishop, S. Larson, and R. A. Tomas, 2020: What drives upper-ocean temperature variability in coupled climate models and observations? *Journal of Climate*, **33 (2)**, 577–596.

Small, R. J., F. O. Bryan, S. P. Bishop, and R. A. Tomas, 2019: Air–sea turbulent heat fluxes in climate models and observational analyses: What drives their variability? *Journal of Climate*, **32 (8)**, 2397–2421.

Small, R. J., R. A. Tomas, and F. O. Bryan, 2014: Storm track response to ocean fronts in a global high-resolution climate model. *Climate dynamics*, **43**, 805–828.

Smirnov, D., M. Newman, M. A. Alexander, Y.-O. Kwon, and C. Frankignoul, 2015: Investigating the local atmospheric response to a realistic shift in the oyashio sea surface temperature front. *Journal of Climate*, **28 (3)**, 1126–1147.

Smith, K. L., R. Neely, D. Marsh, and L. M. Polvani, 2014: The specified chemistry whole atmosphere community climate model (sc-waccm). *Journal of Advances in Modeling Earth Systems*, **6 (3)**, 883–901.

Sobel, A. H., and C. S. Bretherton, 2000: Modeling tropical precipitation in a single column. *Journal of climate*, **13 (24)**, 4378–4392.

Sobel, A. H., J. Nilsson, and L. M. Polvani, 2001: The weak temperature gradient approximation and balanced tropical moisture waves. *Journal of the atmospheric sciences*, **58 (23)**, 3650–3665.

Soden, B. J., I. M. Held, R. Colman, K. M. Shell, J. T. Kiehl, and C. A. Shields, 2008: Quantifying climate feedbacks using radiative kernels. *Journal of Climate*, **21 (14)**, 3504–3520.

Solomon, S., 1999: Stratospheric ozone depletion: A review of concepts and history. *Reviews of geophysics*, **37 (3)**, 275–316.

Solomon, S., D. J. Ivy, D. Kinnison, M. J. Mills, R. R. Neely III, and A. Schmidt, 2016: Emergence of healing in the antarctic ozone layer. *Science*, **353 (6296)**, 269–274.

Solomon, S., and Coauthors, 2022: On the stratospheric chemistry of midlatitude wildfire smoke. *Proceedings of the National Academy of Sciences*, **119 (10)**, e2117325 119.

Stevens, B., S. C. Sherwood, S. Bony, and M. J. Webb, 2016: Prospects for narrowing bounds on earth's equilibrium climate sensitivity. *Earth's Future*, **4 (11)**, 512–522.

Stone, K., S. Solomon, D. Kinnison, and M. J. Mills, 2021: On recent large antarctic ozone holes and ozone recovery metrics. *Geophysical Research Letters*, **48 (22)**, e2021GL095 232.

Stone, K. A., S. Solomon, D. E. Kinnison, C. F. Baggett, and E. A. Barnes, 2019: Prediction of northern hemisphere regional surface temperatures using stratospheric ozone information. *Journal of Geophysical Research: Atmospheres*, **124 (12)**, 5922–5933.

Strahan, S. E., A. R. Douglass, and M. R. Damon, 2019: Why do antarctic ozone recovery trends vary? *Journal of Geophysical Research: Atmospheres*, **124 (15)**, 8837–8850.

Tabazadeh, A., K. Drdla, M. Schoeberl, P. Hamill, and O. Toon, 2002: Arctic "ozone hole" in a cold volcanic stratosphere. *Proceedings of the National Academy of Sciences*, **99 (5)**, 2609–2612.

Taguchi, B., H. Nakamura, M. Nonaka, N. Komori, A. Kuwano-Yoshida, K. Takaya, and A. Goto, 2012: Seasonal evolutions of atmospheric response to decadal sst anomalies in the north pacific subarctic frontal zone: Observations and a coupled model simulation. *Journal of Climate*, **25 (1)**, 111–139.

Taha, G., R. Loughman, T. Zhu, L. Thomason, J. Kar, L. Rieger, and A. Bourassa, 2021: Omps lp version 2.0 multi-wavelength aerosol extinction coefficient retrieval algorithm. *Atmospheric Measurement Techniques*, **14 (2)**, 1015–1036.

Thompson, D. W., M. P. Baldwin, and S. Solomon, 2005: Stratosphere–troposphere coupling in the southern hemisphere. *Journal of the Atmospheric Sciences*, **62 (3)**, 708–715.

Thompson, D. W., and S. Solomon, 2002: Interpretation of recent southern hemisphere climate change. *Science*, **296 (5569)**, 895–899.

Thompson, D. W., S. Solomon, P. J. Kushner, M. H. England, K. M. Grise, and D. J. Karoly, 2011: Signatures of the antarctic ozone hole in southern hemisphere surface climate change. *Nature geoscience*, **4 (11)**, 741–749.

Thompson, L. A., and Y.-O. Kwon, 2010: An enhancement of low-frequency variability in the kuroshio–oyashio extension in ccsm3 owing to ocean model biases. *Journal of climate*, **23 (23)**, 6221–6233.

Toohey, M., K. Krüger, M. Bittner, C. Timmreck, and H. Schmidt, 2014: The impact of volcanic aerosol on the northern hemisphere stratospheric polar vortex: mechanisms and sensitivity to forcing structure. *Atmospheric Chemistry and Physics*, **14 (23)**, 13 063–13 079.

Trenberth, K. E., G. W. Branstator, and P. A. Arkin, 1988: Origins of the 1988 north american drought. *Science*, **242 (4886)**, 1640–1645.

Ueyama, R., and J. M. Wallace, 2010: To what extent does high-latitude wave forcing drive tropical upwelling in the brewer–dobson circulation? *Journal of the atmospheric sciences*, **67 (4)**, 1232–1246.

Vallis, G. K., 2017: *Atmospheric and oceanic fluid dynamics*. Cambridge University Press.

Wang, B., R. Wu, and X. Fu, 2000: Pacific–east asian teleconnection: how does enso affect east asian climate? *Journal of Climate*, **13 (9)**, 1517–1536.

Wang, Q., S.-P. Zhang, S.-P. Xie, J. R. Norris, J.-X. Sun, and Y.-X. Jiang, 2019: Observed variations of the atmospheric boundary layer and stratocumulus over a warm eddy in the kuroshio extension. *Monthly Weather Review*, **147 (5)**, 1581–1591.

Wargan, K., B. Weir, G. L. Manney, S. E. Cohn, and N. J. Livesey, 2020: The anomalous 2019 antarctic ozone hole in the geos constituent data assimilation system with mls observations. *Journal of Geophysical Research: Atmospheres*, **125 (18)**, e2020JD033 335.

Waugh, D. W., W. J. Randel, S. Pawson, P. A. Newman, and E. R. Nash, 1999: Persistence of the lower stratospheric polar vortices. *Journal of Geophysical Research: Atmospheres*, **104 (D22)**, 27 191–27 201.

Weber, M., S. Dikty, J. P. Burrows, H. Garny, M. Dameris, A. Kubin, J. Abalichin, and U. Langematz, 2011: The brewer-dobson circulation and total ozone from seasonal to decadal time scales. *Atmospheric Chemistry and Physics*, **11 (21)**, 11 221–11 235.

Wilka, C., K. Shah, K. Stone, S. Solomon, D. Kinnison, M. Mills, A. Schmidt, and R. R. Neely III, 2018: On the role of heterogeneous chemistry in ozone depletion and recovery. *Geophysical Research Letters*, **45 (15)**, 7835–7842.

Wills, S. M., and D. W. Thompson, 2018: On the observed relationships between wintertime variability in kuroshio–oyashio extension sea surface temperatures and the atmospheric circulation over the north pacific. *Journal of Climate*, **31 (12)**, 4669–4681.

Wills, S. M., D. W. Thompson, and L. M. Ciasto, 2016: On the observed relationships between variability in gulf stream sea surface temperatures and the atmospheric circulation over the north atlantic. *Journal of Climate*, **29 (10)**, 3719–3730.

Woollings, T., B. Hoskins, M. Blackburn, D. Hassell, and K. Hodges, 2010: Storm track sensitivity to sea surface temperature resolution in a regional atmosphere model. *Climate dynamics*, **35**, 341–353.

Xu, H., H. Tokinaga, and S.-P. Xie, 2010: Atmospheric effects of the kuroshio large meander during 2004–05. *Journal of Climate*, **23 (17)**, 4704–4715.

Yau, M. K., and R. R. Rogers, 1996: *A short course in cloud physics*. Elsevier.

Yook, S., D. W. Thompson, and S. Solomon, 2022a: Climate impacts and potential drivers of the unprecedented antarctic ozone holes of 2020 and 2021. *Geophysical Research Letters*, **49 (10)**, e2022GL098 064.

Yook, S., D. W. Thompson, S. Solomon, and S.-Y. Kim, 2020: The key role of coupled chemistry–climate interactions in tropical stratospheric temperature variability. *Journal of Climate*, **33 (17)**, 7619–7629.

Yook, S., D. W. J. Thompson, L. Sun, and C. R. Patrizio, 2022b: The atmospheric response to western north pacific sea-surface temperature anomalies. *Journal of Climate*, **35 (11)**, 3335–3352, doi: 10.1175/JCLI-D-21-0371.1.

Yu, P., and Coauthors, 2021: Persistent stratospheric warming due to 2019–2020 australian wildfire smoke. *Geophysical Research Letters*, **48 (7)**, e2021GL092 609.

Yulaeva, E., J. R. Holton, and J. M. Wallace, 1994: On the cause of the annual cycle in tropical lower-stratospheric temperatures. *Journal of Atmospheric Sciences*, **51 (2)**, 169–174.

Zambri, B., S. Solomon, D. W. Thompson, and Q. Fu, 2021: Emergence of southern hemisphere stratospheric circulation changes in response to ozone recovery. *Nature Geoscience*, **14 (9)**, 638–644.

Zawada, D. J., L. A. Rieger, A. E. Bourassa, and D. A. Degenstein, 2018: Tomographic retrievals of ozone with the omps limb profiler: algorithm description and preliminary results. *Atmospheric Measurement Techniques*, **11 (4)**, 2375–2393.

Zelinka, M. D., and D. L. Hartmann, 2010: Why is longwave cloud feedback positive? *Journal of Geophysical Research: Atmospheres*, **115 (D16)**.

Zhou, C., M. D. Zelinka, and S. A. Klein, 2016: Impact of decadal cloud variations on the earth's energy budget. *Nature Geoscience*, **9 (12)**, 871–874.

Zhou, C., M. D. Zelinka, and S. A. Klein, 2017: Analyzing the dependence of global cloud feedback on the spatial pattern of sea surface temperature change with a g reen's function approach. *Journal of Advances in Modeling Earth Systems*, **9 (5)**, 2174–2189.

Zhou, G., M. Latif, R. J. Greatbatch, and W. Park, 2015: Atmospheric response to the north pacific enabled by daily sea surface temperature variability. *Geophysical Research Letters*, **42 (18)**, 7732–7739.

Zhu, Y., and Coauthors, 2018: Stratospheric aerosols, polar stratospheric clouds, and polar ozone depletion after the mount calbuco eruption in 2015. *Journal of Geophysical Research: Atmospheres*, **123 (21)**, 12–308.